

DIPARTIMENTO DI INGEGNERIA INDUSTRIALE

Dottorato di Ricerca in MECCANICA E SCIENZE AVANZATE DELL'INGEGNERIA

Ciclo XXVI

Settore Concorsuale 09/C2 - FISICA TECNICA E INGEGNERIA NUCLEARE

Settore Scientifico-Disciplinare ING-IND/18 - FISICA DEI REATTORI NUCLEARI

**Fast and accurate numerical solutions in some
problems of particle and radiation transport:
synthetic acceleration for the method of short
characteristics, Doppler-broadened scattering
kernel, remote sensing of the cryosphere**

Presentata da:
Alberto Previti

Relatore:
prof. Domiziano Mostacci

Coordinatore:
prof. Vincenzo Parenti Castelli

Sommario

Questo lavoro si propone di presentare diversi aspetti della simulazione numerica del trasporto di particelle e di radiazione per applicazioni industriali e di protezione ambientale, per consentire l'analisi di processi fisici complessi in modo veloce, affidabile ed efficiente.

Nella prima parte è trattata la velocizzazione della simulazione numerica del trasporto di neutroni per l'analisi del nocciolo di un reattore nucleare. Le proprietà di convergenza della *source iteration* del Metodo delle Caratteristiche applicate a geometrie strutturate eterogenee sono state migliorate per mezzo della *Boundary Projection Acceleration*, consentendo lo studio di geometrie 2D e 3D con la teoria del trasporto senza omogeneizzazione spaziale. Le prestazioni computazionali sono state verificate tramite il *benchmark* C5G7 2D e 3D, mostrando una sensibile riduzione del numero di iterazioni e del tempo di calcolo.

La seconda parte è dedicata allo studio dello *scattering* elastico dei neutroni con isotopi pesanti in funzione della temperatura vicino alla zona termica. È presentato il calcolo numerico della convoluzione Doppler del kernel di *scattering* elastico col modello gas per una generale sezione d'urto dipendente dall'energia e per una generica legge di *scattering* nel sistema del centro di massa. L'intervallo di integrazione è stata ottimizzato utilizzando un *cutoff* numerico, consentendo una valutazione numerica più veloce dell'integrale. I momenti di Legendre del *kernel* di trasferimento sono successivamente ottenuti per quadratura diretta e validati tramite un'analisi numerica della convergenza.

La terza parte è focalizzata alle applicazioni di telerilevamento del trasferimento radiativo per indagini sulla criosfera terrestre. L'equazione del trasporto per fotoni è applicata per simulare la riflettività dei ghiacciai a diverse età dello strato di neve o ghiaccio, al suo spessore, alla presenza o meno di altri strati sottostanti, al grado di polvere inclusa nella neve, creando un sistema in grado di decifrare segnali spettrali raccolti dai rivelatori orbitanti.

Abstract

The aim of this work is to present various aspects of numerical simulation of particle and radiation transport for industrial and environmental protection applications, to enable the analysis of complex physical processes in a fast, reliable, and efficient way.

In the first part we deal with speed-up of numerical simulation of neutron transport for nuclear reactor core analysis. The convergence properties of the source iteration scheme of the Method of Characteristics applied to heterogeneous structured geometries has been enhanced by means of Boundary Projection Acceleration, enabling the study of 2D and 3D geometries with transport theory without spatial homogenization. The computational performances have been verified with the C5G7 2D and 3D benchmarks, showing a sensible reduction of iterations and CPU time.

The second part is devoted to the study of temperature-dependent elastic scattering of neutrons for heavy isotopes near to the thermal zone. A numerical computation of the Doppler convolution of the elastic scattering kernel based on the gas model is presented, for a general energy dependent cross section and scattering law in the center of mass system. The range of integration has been optimized employing a numerical cutoff, allowing a faster numerical evaluation of the convolution integral. Legendre moments of the transfer kernel are subsequently obtained by direct quadrature and a numerical analysis of the convergence is presented.

In the third part we focus our attention to remote sensing applications of radiative transfer employed to investigate the Earth's cryosphere. The photon transport equation is applied to simulate reflectivity of glaciers varying the age of the layer of snow or ice, its thickness, the presence or not other underlying layers, the degree of dust included in the snow, creating a framework able to decipher spectral signals collected by orbiting detectors.

La filosofia è scritta in questo grandissimo libro che continuamente ci sta aperto innanzi a gli occhi (io dico l'universo), ma non si può intendere se prima non s'impara a intender la lingua, e conoscer i caratteri, ne' quali è scritto. Egli è scritto in lingua matematica, e i caratteri son triangoli, cerchi, ed altre figure geometriche, senza i quali mezzi è impossibile a intenderne umanamente parola; senza questi è un aggirarsi vanamente per un oscuro laberinto.

Galileo Galilei, *Il Saggiatore* (1623), capitolo VI

*«O frati,» dissi, «che per cento milia
perigli siete giunti a l'occidente,
a questa tanto picciola vigilia*

*d'i nostri sensi ch'è del rimanente
non vogliate negar l'esperienza,
di retro al sol, del mondo senza gente.*

*Considerate la vostra semenza:
fatti non foste a viver come bruti,
ma per seguir virtute e canoscenza».*

Dante Alighieri, *La Divina Commedia, Inferno 26*, vv. 112-120

Contents

| | |
|--|-----------|
| Introduction | 1 |
| References | 8 |
| 1 Synthetic acceleration for neutron transport in structured geometries | 9 |
| 1.1 Neutrons transport | 13 |
| 1.1.1 Basic quantities | 13 |
| 1.1.2 Integro-differential neutron balance | 18 |
| 1.1.3 Interface and boundary conditions | 20 |
| 1.1.4 Eigenvalue problem | 21 |
| 1.1.5 Integral formulation | 22 |
| 1.2 Discretization of transport equation | 24 |
| 1.2.1 Energy variable | 24 |
| 1.2.2 Angular variable | 26 |
| 1.2.3 Spatial variable | 29 |
| 1.3 Solution of the transport problem | 29 |
| 1.3.1 Method of short characteristics: IDT | 29 |
| 1.3.2 Representation of Balance and Transmission | 32 |
| 1.3.3 Inner and Outer iterations | 36 |
| 1.4 Boundary Projection Acceleration | 37 |
| 1.4.1 Synthetic acceleration | 38 |
| 1.4.2 BPA for the Method of Short Characteristics in HCC | 40 |
| 1.4.3 Boundary source correction | 45 |
| 1.4.4 Numerical implementation | 46 |
| Storage strategy and vectorization | 46 |
| Flowcharts of the implementation | 48 |
| 1.5 Numerical results | 51 |
| 1.5.1 C5G7: 2D configuration | 54 |
| 1.5.2 C5G7: 3D Rodded B configuration | 64 |
| References | 67 |
| 2 Thermal effects of neutron scattering off heavy isotopes | 69 |
| 2.1 Mathematical formulation of Doppler convolution | 72 |
| 2.1.1 Definitions and dynamics of elastic scattering | 72 |
| 2.1.2 Range of integration | 76 |
| 2.1.3 Computation of the transfer kernel | 77 |
| 2.1.4 Calculation of the angular moments | 81 |
| 2.2 Numerical implementation | 81 |

| | | |
|----------|---|------------|
| 2.2.1 | Kernel computation | 81 |
| 2.2.2 | Angular moments calculation | 83 |
| 2.2.3 | Flowchart of the implementation | 84 |
| 2.3 | Numerical results | 85 |
| 2.3.1 | Kernel computation | 88 |
| | Dependence on medium temperature | 88 |
| 2.3.2 | Angular moments calculation | 94 |
| | Convergence analysis | 95 |
| | Angular moments near the thermal region | 95 |
| | Behavior around the resonances | 98 |
| | Effects at higher energies | 102 |
| 2.3.3 | Influence of anisotropy of the scattering | 102 |
| | References | 105 |
| 3 | Radiative transfer modeling for remote sensing of the cryosphere | 107 |
| 3.1 | Fundamentals of radiative transfer | 109 |
| 3.1.1 | Particle and wave models for photon transport | 109 |
| 3.1.2 | Transport modeling for remote sensing | 110 |
| 3.1.3 | Mathematical setting for layered media | 113 |
| 3.1.4 | Quantities of interest for remote sensing | 114 |
| 3.2 | Radiative transfer modeling for glaciers surfaces monitoring | 116 |
| 3.2.1 | Snow | 118 |
| 3.2.2 | Glacier ice | 120 |
| 3.2.3 | Rock debris | 121 |
| 3.2.4 | Mixtures | 122 |
| 3.3 | Numerical solution method | 123 |
| 3.3.1 | MADOC | 125 |
| 3.4 | Glacier simulations results | 127 |
| | References | 134 |
| | Conclusions | 137 |

List of Tables

| | | |
|-----|--|-----|
| 1.1 | C5G7 2D: eigenvalues and percent difference with respect to reference (1.18655), varying acceleration (outers and inners), MOC spatial moment order (Constant, Linear, Bilinear). Quadrature schemes: Level-Symmetric and Chebyshev-Legendre with $N = 4, 6, 8, 12, 16, S_2$, Level-Symmetric S_8^* | 55 |
| 1.1 | C5G7 2D: eigenvalues and percent difference with respect to reference (1.18655), varying acceleration (outers and inners), MOC spatial moment order (Constant, Linear, Bilinear). Quadrature schemes: Level-Symmetric and Chebyshev-Legendre with $N = 4, 6, 8, 12, 16, S_2$, Level-Symmetric S_8^* | 56 |
| 1.1 | C5G7 2D: eigenvalues and percent difference with respect to reference (1.18655), varying acceleration (outers and inners), MOC spatial moment order (Constant, Linear, Bilinear). Quadrature schemes: Level-Symmetric and Chebyshev-Legendre with $N = 4, 6, 8, 12, 16, S_2$, Level-Symmetric S_8^* | 57 |
| 1.2 | C5G7 3D: eigenvalues and percent difference with respect to reference (1.07777), varying acceleration (outers and inners), MOC spatial moment order (Constant, Linear). Quadrature scheme: Level-Symmetric S_8^* | 65 |
| 3.1 | Symbols used to describe optical properties of mixtures. | 122 |
| 3.2 | Input optical parameters employed for MADOC BRF simulations of intimate and areal mixtures of ice and soil. | 133 |

List of Figures

| | | |
|------|---|----|
| 1.1 | Discretization of a BWR assembly. | 10 |
| 1.2 | Schematic illustration of an heterogeneous cell: water (blue), cladding (black), fuel (orange). | 12 |
| 1.3 | Deviation angle for an elastic scattering. | 17 |
| 1.4 | Schematic illustration of a 2D HCC with 2 regions. V_1 and V_2 are the 2 regions. $s_1, s_2, s_3,$ and s_4 are the 4 exterior surfaces. $o_1, o_2, o_3,$ and o_4 are the 4 octants. | 33 |
| 1.5 | Flowchart of the BPA preprocessing. | 49 |
| 1.6 | Flowchart of the iterative BPA algorithm. | 50 |
| 1.7 | C5G7 benchmark: geometry, material composition, and solver discretization. | 52 |
| 1.8 | C5G7 2D benchmark. Quadrature Level Symmetric. Inner iterations and total time varying MOC spatial order (constant, linear, bilinear), SN quadrature order, and acceleration scheme. | 59 |
| 1.9 | C5G7 2D benchmark. Quadrature Chebyshev Legendre. Inner iterations and total time varying MOC spatial order (constant, linear, bilinear), SN quadrature order, and acceleration scheme. | 60 |
| 1.10 | C5G7 2D benchmark. Quadrature S2 and S8*. Inner iterations and total time varying MOC spatial order (constant, linear, bilinear) and acceleration scheme. | 61 |
| 1.11 | C5G7 2D benchmark. Quadrature Level Symmetric. Inner iterations and total time varying MOC spatial order (constant, linear, bilinear), and SN quadrature order. Comparison CMFD (Inners) vs BPA (Inners). | 62 |
| 1.12 | C5G7 2D benchmark. Quadrature Level Symmetric. Inner iterations and total time varying MOC spatial order (constant, linear, bilinear), and SN quadrature order. Comparison CMFD (Outers) + CMFD (Inners) vs CMFD (Outers) + BPA (Inners). | 63 |
| 1.13 | C5G7 3D benchmark. Quadrature S8*. Inner iterations and total time varying MOC spatial order (constant, linear) and acceleration scheme. | 66 |
| 2.1 | Reference system with c as polar axis. | 74 |
| 2.2 | Bounds for μ_{COM} versus E_r | 76 |
| 2.3 | Flowchart of the computation of Doppler-broadened angular moments. | 84 |

| | | |
|------|---|-----|
| 2.4 | Elastic scattering cross section for ^{238}U at 1000 K near various resonances. | 86 |
| 2.5 | Elastic scattering cross section for ^{238}U near the 1474 eV resonance at 1000 K and its degree of anisotropy. | 87 |
| 2.6 | Analytical kernel at 1000 K for different E values versus μ_{LAB} for $\sigma = 1$ and $E = 6.5$ eV. | 89 |
| 2.7 | $P_T(E \rightarrow E', \mu_{\text{LAB}})$ for $E = 6.5$ eV near 6.67 eV for $\sigma = 1$. 3D rendering of the dependency upon μ_{LAB} and E' | 90 |
| 2.8 | $P_T(E \rightarrow E', \mu_{\text{LAB}})$ for $E = 6.5$ eV near 6.67 eV for $\sigma = 1$. Cuts for most significant μ_{LAB} . Higher temperatures result in a broadening of the peaks. | 91 |
| 2.9 | $P_T(E \rightarrow E', \mu_{\text{LAB}})$ for $E = 6.5$ eV near the 6.67 eV resonance of ^{238}U . 3D rendering of the dependency upon μ_{LAB} and E' | 92 |
| 2.10 | $P_T(E \rightarrow E', \mu_{\text{LAB}})$ for $E = 6.5$ eV near the 6.67 eV resonance of ^{238}U . Cuts for most significant μ_{LAB} . A strong up-scattering in backward directions is manifested for higher temperatures. | 93 |
| 2.11 | $P_{0,T}(E \rightarrow E')$ for ^{238}U for different values of T . The asymptotic model is depicted as a solid black line. | 94 |
| 2.12 | Convergence analysis of computation of $P_{0,T}(E \rightarrow E')$ for ^{238}U increasing the angular representation with $E = 6.5$ eV at 1000 K. | 96 |
| 2.13 | $P_{0,T}(E \rightarrow E')$ for constant and ^{238}U cross sections at 1000 K for $E = 6.5$ eV. A pronounced up-scattering is found when the Doppler convolution is fully taken into account. | 97 |
| 2.14 | $P_{n,T}(E \rightarrow E')$ for constant and ^{238}U cross sections at 1000 K for $E = 6.5$ eV. A pronounced up-scattering is found when the Doppler convolution is fully taken into account. | 99 |
| 2.15 | $P_{0,T}(E \rightarrow E')$ for ^{238}U for different values of E | 100 |
| 2.16 | $P_{1,T}(E \rightarrow E')/P_{0,T}(E \rightarrow E')$ for ^{238}U for different values of E | 100 |
| 2.17 | $P_{2,T}(E \rightarrow E')/P_{0,T}(E \rightarrow E')$ for ^{238}U for different values of E | 101 |
| 2.18 | $P_{3,T}(E \rightarrow E')/P_{0,T}(E \rightarrow E')$ for ^{238}U for different values of E | 101 |
| 2.19 | Angular moments for ^{238}U at 1000 K for $E = 9865$ eV. The complete Doppler convolution does not affect the Legendre moments. | 103 |
| 2.20 | $P_{0,T}(E \rightarrow E')$ with and without anisotropy of scattering for ^{238}U near the 1474 eV resonance. | 104 |
| 3.1 | Spectral behavior of the complex index of refraction for pure ice. | 119 |
| 3.2 | Spectral albedo for a layer of optically thick pure snow as a function of wavelength and grain size. The solar zenith angle is 30 degrees. | 127 |
| 3.3 | Spectral albedo for a layer of optically thick pure snow as a function of wavelength and solar zenith angle. The particle grain size is fixed and assumed to be 50 μm | 129 |
| 3.4 | Spectral albedo for a layer of optically thick mixture of pure snow and carbon soot as a function of wavelength and snow grain size. Soot particle concentration is assumed to be 3 ppmw. | 130 |
| 3.5 | Spectral albedo for a layer of pure snow over a layer of optically thick ice as a function of wavelength and snow depth. The snow particle grain size is assumed to be 50 μm | 131 |

3.6 BRF simulations for intimate mixtures (in volume percentage) of ice and sediment/soil. The white dot represents the impinging solar beam. The overall magnitude (i.e. albedo) decreases as the percentage of soil increases. The BRF patterns are also a function of the mixture percentage. This set of simulations shows that BRF patterns can be potentially used to discriminate between various surface materials and conditions in glacier environments. 132

Introduction

The scientific revolution of the 17th century is universally accepted as the starting point of modern natural sciences. Galileo Galilei developed the so-called *scientific method* during his studies on the motion of falling bodies. Since that time this method has become the formal procedure for all scientific endeavor, and the globally accepted way to investigate phenomena and acquire or correct our knowledge of the world. The scientific method comprises two main aspects: formulation of an hypothesis and experimental verification of that hypothesis. The continuous iterative feedback between these two phases, together with the Popperian imaginative and “artistic” approach of the scientists, brings to the refinement of the proposed hypothesis until a convergence and a new theory is established. The deductive reasoning proposed by Aristotle is then rejected for an objective approach to scientific discovery.

In physical sciences, a formal hypothesis or theory takes the form of one or more mathematical expressions. The real power of science is then its ability to describe the world through these exact mathematical relations and at the same time to make predictions about the behavior of a particular system. Still, the complexity of the relations needed makes increasingly difficult, and often unfeasible, to analyze our world only through experiments.

More recently, an additional aspect has gained more and more importance in the daily activity of scientists: numerical simulation. The mathematical representation of the nature can be transformed into computer codes. In fact, with the help of computers scientists can formalize the details and the interdependent relations that describe how a particular system behaves. Nature can then be re-created in scientific *dream machines* mimicking these dynamics by means of computer models. In this way, computer simulation serves as an additional step in the scientific method (Summers, 1998). The interest of engineers in computer simulation is the ability to have an additional tool to assist the design and analysis of a particular man-made system. Computer simulation studies are in fact an intermediate step between the initial ideas and the prototypes.

The research activity presented in this work regards the numerical aspect of

particle and radiation transport for industrial and environmental protection applications. The techniques employed are part of the bigger framework of nuclear reactor physics, and are connected with the necessity to simulate and analyze complex physical processes in a fast, reliable, and efficient way. The mathematical formulation employed to deal with these problems is quite old. The diffusion and dynamical behavior of an ensemble of neutral particles was considered at the beginning by Maxwell in 1859, and was later examined by Boltzmann in a more rigorous fashion in 1895. Boltzmann's formulation of the problem of particle diffusion under various scattering laws has remained unchanged since its discovery (Williams, 1966). The transport of neutron is described accurately through Boltzmann's original equation, and more modern quantum mechanical correction and more rigorous derivation of the base equation do not change the original framework. The mathematics needed to describe these phenomena was therefore ready and with more than seventy years of maturity when Chadwick discovered the neutron in 1932. Moreover, due to very low density of neutrons inside matter, the original non-linear collision terms of the equations proposed by Boltzmann could be discarded, drastically simplifying the mathematical problems to be solved and opening the era of the commercial exploitation of nuclear energy for peaceful purposes.

Also photon transport problems can be approached by linear transport theory, and the propagation of light can be analyzed with the same methods employed for neutrons. The problem of specifying the radiation field in an atmosphere that scatters lights with well-defined physical laws originated in Lord Rayleigh's studies in 1871 (Chandrasekhar, 1960). Later, the problem of illumination and polarization of light was formalized using the transport theory. Consequently various solution methods of the Boltzmann equation take their origin at the beginning of the XX century by astrophysicists and were applied to photon transport in galactic dusts. Around the middle of the century, and especially at the end of World War II, new methods were conceived to solve the neutron field inside the multiplying media of interest for nuclear technology. Lately, new photon applications, like remote sensing for Earth and climate change monitoring, renewed the interest in photon applications of the transport theory. This continuous exchange of ideas and methods between these two fields has stimulated and increased the scientists and engineers efforts to better represent and simulate the particle and radiation transport through media using numerical models.

The transport equation describes the population of neutron or the intensity of a radiation field, and it is based on the principle of particle conservation. Let's consider the case of neutrons, knowing that analogous consideration can be done for photons. Describing the state of a particle system requires knowing the po-

sition and the speed of each particle in every moment. Although the interaction between neutron and nucleus is described through quantum mechanics laws, the wave nature of neutron can be discarded for our applications, and a theory based on classical mechanics can be developed. The collision of a particle inside a medium takes place in a completely random way, at the same time the direction and the velocity after a scattering event depend upon probabilistic laws. This means that the quantum laws of interactions can be enclosed inside a given parameters named cross sections, that provide the probability of a requested type of event given input characteristics of the incident neutron. Considering this point and remembering the quantum indeterminateness characterizing these phenomena, it is justified why the transport of neutron and photons inside matter is better described through an approach of *statistical mechanics*.

The density of neutron in a particular point of the medium to be considered is a result of the scattering parameters of the said medium. Since scattering itself is based on a given probability of collision, also the neutron density would be affected by fluctuations. For a sufficiently big ensemble of particles, the entity of fluctuations per cm^3 is of the order of $1/\sqrt{n}$. In a thermal nuclear reactor, for example, $n = 1 \times 10^6 \text{ cm}^{-3}$ and then $1/\sqrt{n} = 0.1\%$, that is negligible. This means that for our considerations the density of neutron will be always sufficiently high, and the statistical fluctuations will not affect the validity of our calculations. At the same time the density of nuclei N in the system to be analyzed is much greater than the neutron density n . For a thermal reactor $n = 10^6 \div 10^9 \text{ cm}^{-3}$ and $N = 10^{19} \div 10^{22} \text{ cm}^{-3}$. This means that a neutron generated inside a medium with atomic density N will almost surely interact with another nucleus and not with another neutron. As a result this justifies the linear nature of transport of neutron (Boffi, 1974).

In the attempts to better understand the key processes that govern the evolution and the Earth's biosphere, the ability to investigate and study the environment of our planet using remote sensing techniques plays a crucial role. This is connected with the renewed concerns over global warming and greenhouse effect, and on the consequent research about the responses of the Earth as a complete system. In particular, high-latitude and high-altitude environments are known to be sensitive to climate change. The complex problem of the reflectance caused by the atmosphere and by mixtures of soil, snow and debris is therefore of paramount importance in the research connected with surface processes and natural resources of the cryosphere. Addressing this issue requires modeling and simulation of the photon field inside those media using the *transport equation*, whose results should be compared with the data provided by artificial satellites with scientific instruments orbiting around our planet. These instruments measure the intensity of the

photon field at various wavelengths, and are sensitive to the spectral emission of glaciers mixtures, allowing investigations about the composition and thickness of the polar ice sheets.

At the same time, nuclear technology, and in particular nuclear energy, represents a concrete and effective alternative to traditional fossil source of energy in the effort to contrast climate changes, given the bigger and bigger energetic needs of mankind that, in light of the continuous development and improvement of the quality of life, require the production and distribution of an increased amount of electric energy. In fact, nuclear power reactor are devices capable of generate electricity without a direct emission of greenhouse gases, and therefore are expected to play a relevant role together with renewable sources in the energy transition from fossil sources. This transition is essential to preserve Earth's biosphere and to guarantee a sustainable development.

The fundamental component of a nuclear system is the reactor *core*, that is the place where nuclear reactions and the consequent release of thermal energy take place. In our applications we are interested only in fission, i.e. in exothermic split of heavy nuclei provoked by neutron bombardment. The core of a typical nuclear reactor is composed by the fissile material (like ^{235}U or ^{239}Pu). When one of these nuclei is hit by a neutron, there is a significant chance that this nucleus absorb the neutron, becoming highly unstable and splitting into two fragments after a very short transition (1×10^{-22} s to 1×10^{-14} s), releasing at the same time 2 or 3 energetic neutrons (about 2 MeV) and a great amount of energy (about 200 MeV). This energy can be transferred to a cooling fluid, and thus used to produce steam and then electricity using turbines like ordinary coal-fired plants. At the same time, while the neutron initiating the reaction disappears, the new neutrons generated sustain the so-called *chain reaction*. Since not all the neutrons induce a fission, the nuclear multiplying medium is said to be in *critical* state when the neutron population and consequently the energy released is stationary in time.

The first self-sustained nuclear reaction was realized in Chicago by a group on scientists lead by Enrico Fermi in 1942, and the potentiality of these reactors as a powerful source of neutron and gamma rays to be employed for medical purposes, material testing and power generation was soon realized (Fermi and Szilard, 1944). The first nuclear reactor whose only scope was generating electric power appeared in 1954 in the USSR, and a year later in the USA, while the first commercial power plant was started in the UK in 1956.

From the illustration of the principle of operation of a power plant, it is evident how the precise knowledge of the neutron population inside the reactor core is compelling in the design and operation of these systems. Because of the extreme

complexity and high cost of a real nuclear reactor, it is unfeasible to design such system only through experimentation and prototypes, and therefore the contribution of numerical simulation is decisive in this field. Concerns about safety and security of nuclear power plants have stimulated in the last decades an increased effort in developing more and more accurate numerical tools to better calculate and predict the neutron population inside a reactor core. At the same, such tools can be applied by the industry to both optimize current operating plants fuel assemblies and by research centers to investigate and design new innovative Generation IV systems, that are expected to provide a more concrete and economically bearable answer to electric generation, while greatly improving the security and the safety of the current commercially exploited designs.

Since currently the design phase of nuclear core and photons detector is performed by means of numerical models, it is of paramount importance that the results provided by computers are accurate and very close to reality. In this process, a continuous short iterative feedback loop is needed to continually refine the model of the object or system to be constructed until an optimal design is reached. Thus, accuracy and velocity play together a crucial role in the effectiveness of numerical simulations used by engineers.

The solution of every complex physical problem, such as the computation of the radiation field into a generic medium or the determination of the neutron population inside a reactor core, requires a double step: transformation of the real physical problem into one or more mathematical equations in which the physical phenomena are modeled through a series of approximations, and conversion to a numeric problem to be solved with the algorithmic methods of numerical analysis. In the last years, in particular with the application of the transport theory to nuclear and radiative problems, the dependence on large-scale computing and then the reliance on numerical methods increased, which in turn encouraged development of more powerful and sophisticated numerical tools. While these tools enable more comprehensive investigations of transport processes, they generally possess an inherent shortcoming, i.e. some degree of numerical discretization error. This error is a result of the finiteness, though large by past standards, of computer storage (Ganapol, 2008). This is the reason why it is necessary to *validate* the numerical models against experiments and to *verify* the effectiveness and accuracy of the numerical schemes employed to resolve the equations representing the system of interest.

There are two different simulation philosophies to solve the neutron and photon transport equations: *stochastic* and *deterministic* methods. The Monte Carlo method is the direct simulation of a population of particles, and it is realized through the pseudo-random number generator used to reproduce the inherent

stochastic nature of particle-matter interaction. This method is based on following the stories of a very large number of particles, to get a representative average thanks to the central limit theorem. While numerous improvements has been achieved in recent years due to parallel machines, and increased computer speed and memory storage (Martin, 2012), Monte Carlo remains prohibitive for routine design studies in remote sensing and nuclear reactor applications, where repeated very fast simulations are always needed. This is due to the intrinsic nature of Monte Carlo: while it is very accurate, it requires a very large number of histories and therefore an excessive calculation time to produce results with acceptable statistics.

On the contrary, deterministic methods are fundamentally based on a numerical scheme to solve directly the general linear transport equation. The unknown of this equation is the *angular flux*, that is a distribution function representing the particle population in the phase space. Analytical solutions of the transport equation exist only for idealized cases, i.e. one-dimensional, homogeneous, and monoenergetic systems. Still, there are efficient numerical schemes to solve this equation for more realistic cases like real industrial nuclear systems, that present an extreme complexity in the geometry and heterogeneity of materials. Current industrial needs comprise tools to calculate a large number of reactor cycles, to be performed in relatively short times and comprising many three-dimensional steady-state calculations (Sanchez, 2012). This is the reason why this second approach is preferred when a multitude of fast calculates is needed in engineering design.

This work presents various aspects of the improvement of the simulation of transport processes for neutrons and photons.

In Chapter 1 we deal with the numerical solution of the neutron transport equation for nuclear reactor applications. In particular we present the utilization of the Boundary Projection Acceleration (BPA) to the method of characteristics applied to be heterogeneous structured geometries. This approach has been incorporated into the transport solver IDT (**I**ntegro-**D**ifferential **T**ransport) (Masiello et al., 2009), part of APOLLO3 code system developed at SERMA¹/LTSD² laboratory of the CEA³ center of Saclay, France. The BPA is a synthetic acceleration scheme applied to the speed-up of the source iteration for the discrete-ordinates method deterministic solution of the neutron transport equation. We will see the details of our implementation of this scheme inside IDT, specifying also how we deal with the residue on boundary conditions as an additional correction for the

¹Service d'Études des Réacteurs et de Mathématiques Appliquées

²Laboratoire de Transport Stochastique et Déterministe

³Commissariat à l'énergie atomique et aux énergies alternatives

acceleration problem. The effectiveness and accuracy of this approach are tested using the C5G7 UO₂-MOX benchmark case.

In Chapter 2 we deal with the problem of accurately representing the energy dependent scattering cross section near the thermal range. A numerical computation of the Doppler convolution of the elastic scattering kernel based on the gas model is presented, without making assumptions on the variation of the cross section with energy and for a general scattering law in the center of mass system. This enhancement of the generation of scattering kernel for multigroup cross section generation is needed because it is shown that the exact scattering kernel increases light water reactors Doppler coefficients by 10%, affecting the full power eigenvalues by about 200 pcm for light water reactors and about 450 pcm for high temperature reactors (Lee et al., 2008). We will see how the range of integral to be computed has been optimized employing a numerical cutoff, allowing a faster numerical evaluation of the convolution integral, and how Legendre moments of the transfer kernel are subsequently obtained by direct quadrature, presenting a numerical analysis of the convergence.

In Chapter 3 we focus our attention to remote sensing applications of radiative transfer employed to investigate the Earth's cryosphere. The numerical method employed to solve the radiative transfer equation is based on a multilayer extension of the Analytical Discrete Ordinates Method (Siewert, 2000), that provides an efficient and fast way to compute the photon field inside parallel-plane stratified media typical of remote sensing applications. We will see how the radiative transfer equation can be applied to decipher the spectral signals collected by orbiting detectors employed in the study of glaciers and frozen lakes. We present the results of simulations of the reflectivity of glaciers varying the age of the layer of snow or ice, its thickness, the presence or not other underlying layers, the degree of dust included in the snow.

References

- V. Boffi (1974). *Fisica del reattore nucleare. La teoria del trasporto dei neutroni*. Pàtron.
- S. Chandrasekhar (1960). *Radiative Transfer*. Dover.
- E. Fermi and L. Szilard (1944). "Neutronic reactor". US 2708656.
- B. D. Ganapol (2008). *Analytical Benchmarks for Nuclear Engineering Applications, Case Studies in Neutron Transport Theory*. NEA/DB.
- D. Lee, K. Smith, and J. Rhodes (2008). "The impact of ^{238}U resonance elastic scattering approximations on the thermal reactor Doppler reactivity". In: *International Conference on Reactor Physics, Nuclear Power: A Sustainable Resource (PHYSOR 2008)*. Interlaken, Switzerland.
- W. R. Martin (2012). "Challenges and Prospects for Whole-Core Monte Carlo Analysis". In: *Nuclear Engineering and Technology* 44.2, pp. 151–160. DOI: 10.5516/NET.01.2012.502.
- E. Masiello, R. Sanchez, and I. Zmijarevic (2009). "New Numerical Solution with the Method of Short Characteristics for 2-D Heterogeneous Cartesian Cells in the APOLLO2 Code: Numerical Analysis and Tests". In: *Nuclear Science And Engineering* 161, pp. 257–278.
- R. Sanchez (2012). "Prospects in Deterministic Three-Dimensional Whole-Core Transport Calculations". In: *Nuclear Engineering and Technology* 44.2, pp. 113–150. DOI: 10.5516/NET.01.2012.501.
- C. E. Siewert (2000). "A concise and accurate solution to Chandrasekhar's basic problem in radiative transfer". In: *Journal of Quantitative Spectroscopy and Radiative Transfer* 64, pp. 109–130. DOI: 10.1016/S0022-4073(98)00144-7.
- R. L. Summers (1998). "Computer Simulation Studies and the Scientific Method". In: *Journal of Applied Animal Welfare Science* 1.2, pp. 119–131. DOI: 10.1207/s15327604jaws0102_3.
- M. M. R. Williams (1966). *The slowing down and thermalization of neutrons*. North-Holland.

Chapter 1

Synthetic acceleration for neutron transport in structured geometries

A nuclear reactor is a device conceived to produce and sustain a controlled fission chain reaction. In the reactor core, neutrons undergo fission, generating new neutrons, gamma rays, and a large amount of thermal energy. The latter is used in power plant to produce electricity. Accurate knowledge of neutron population inside the reactor core is of paramount importance to efficiently control the chain reaction. The neutron population can be represented by the angular flux $\psi(r, E, \Omega, t)$, that depends upon the position r , the flight direction Ω , the kinetic energy E , and time t . The angular flux is determined by solving the neutron transport equation, that is the balance of neutrons in the phase space.

The study of a nuclear reactor core encounters many delicate aspects,

- *the precision of the results.* The critically state of a nuclear reactor, which corresponds to the condition in which the neutron population and thus the power generated are constants, is a very sensitive equilibrium that requires a precise determination of the principal quantities (e.g. temperature, power distribution, etc.). Typically the acceptable errors should not exceed few percentage ($\approx 3 \div 5\%$).
- *the representation of the geometry.* A nuclear reactor core is composed by a regular ensemble of heterogeneous fuel assemblies. The correct representation of the fuel pins and assemblies is necessary to achieve accurate results. In particular, the approximation of curved surface is particularly delicate, and source of errors in the estimation of the angular flux.
- *the nuclear data.* The physics of nuclear reactions that take place inside the core are presented through interaction cross sections. The international databases of nuclear data, such as ENDF/B or JEFF, are provided for a very

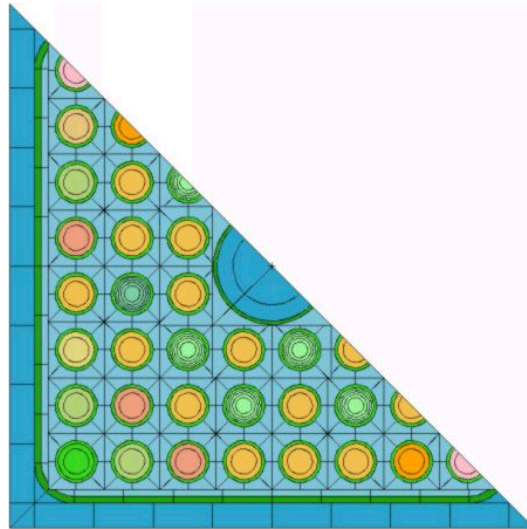


Figure 1.1 Discretization of a BWR assembly.

fine energy mesh, thus requiring a process of interpolation or condensation that can introduce further errors.

The geometrical and material heterogeneity of a nuclear reactor core results in a strong variation of the angular flux. At the same time, the energy interval to be taken into account is very large: from few hundredths of eV (thermal neutrons) to several MeV (fast neutron resulting from fission). For these reasons a discretization of the transport equation for the whole reactor is unfeasible, and the determination of the neutron population is achieved through a two-step procedure. At first, the neutron transport equation is solved as precisely as possible over a reduced geometry, e.g. a fuel assembly (see Figure 1.1). This is also called *lattice calculation*, since an infinite repetition of the same geometric pattern is taken into account in solving the transport equation. This computation is performed with a very fine discretization of the energy variable, in order to compile a few macrogroup parametrized library of homogenized constants. Then, the second step consists of a full core calculation. It is generally based on the diffusion theory, that is a simplification of the full transport theory. In addition, the core is represented in a simplified geometry making use of the few group interaction cross sections calculated in the first phase. Finally, a reconstruction technique is applied to accurately determine the angular flux in each position.

The material properties of a nuclear reactor, represented by the macroscopic cross sections (as we discuss below), change during its operation life. In fact, nuclear reactions produce transmutation of nuclei composing the core, thus modifying the isotopic concentrations inside the fuel. In particular, the amount of fissile

and fissionable material decrease, and an increased amount of fission products are generated. Nevertheless, experimental evidence has shown that significant changes in material properties occur on a time scale much greater than the interval between two successive neutron collisions. Thus criticality calculations can be done assuming a constant material composition using the two-step procedure. Temporal variation of materials important for reactor fuel cycle analysis is then studied coupling a multitude of core calculations with isotopic depletion calculations, that are dependent upon the angular flux. This is a *quasi-static* process that removes the non-linearity coming from the dependence on the time of cross sections. In addition, we underline that we assume the *local thermodynamic equilibrium*, since the spatial range of variation of the temperature inside the core is sensibly larger than the neutron mean free path.

The diffusion theory normally employed in the second step just mentioned introduces strong approximations. In fact, it is derived from a truncation of the Taylor's flux expansion series at first terms, neglecting upper derivatives. As a consequence, pronounced variations of the flux due to the extreme heterogeneity commonly found in a nuclear reactor core cannot be completely represented. For example, this is the case of fuel assemblies containing strong neutron absorbers for the water cooled and moderated thermal reactors, or of interface core-reflector for fast reactors. The industrial need of forecast accurately power distribution at nominal as well as accidental conditions demands improved numerical methods for reactor core calculations. In this framework, transport theory offer a mathematical tool capable to describe the angular flux in a more precise way. Given the increase computer power, new numerical methods capable of solving the neutron transport equation for large optical regions have been conceived in the last years to perform core computation without the diffusion approximation.

Spatial and angular discretization are need to numerically solve the neutron transport equation. Regarding the former, various possibilities are possible, e.g. finite differences, nodal methods, finite elements, method of characteristics (MOC) (Sanchez and McCormick, 1982). The latter has become a standard for 2D assembly or assembly motifs and is currently applied also for 2D whole-core transport calculations (Sanchez, 2012b). Its success is due to the high accuracy of its solutions, that are guaranteed thanks to the fact that the neutron balance equation is solved together with an additional transmission equation, providing a more precise determination of the interface condition among at the boundaries of the spatial mesh. In fact, numerical methods such as diamond differences and low-order finite elements may not give enough accuracy for optically large regions.

The code IDT (Integro-Differential Transport) of the platform APOLLO (Sanchez, Zmijarevic, et al., 2010) developed by the CEA center of Saclay implements the

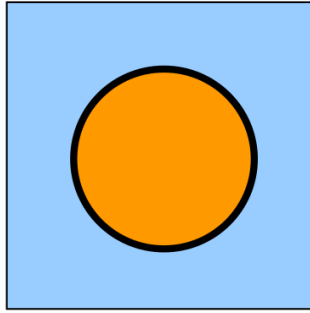


Figure 1.2 Schematic illustration of an heterogeneous cell: water (blue), cladding (black), fuel (orange).

method of characteristics for structured 2D and 3D Cartesian geometries (*Method of Short Characteristics, (MSC)*). It has been conceived as a tool to apply the transport theory to assembly and core analysis. The method of short characteristics has been proposed in the early 80's for the solution of transport equation for $x - y$ regular geometries. It is based on the integral formulation of the transport equation, that is used to represent exactly the propagation throughout Cartesian cells. In each cell, the angular flux and the sources are expanded on polynomial base functions.

The method of short characteristics in IDT has been originally conceived to determine the angular flux into a reactor core considering homogenized regions (Zmijarevic, 1998). Despite its fast solution and high accuracy, the homogeneous rectangular mesh is inefficient for approximating curved material interfaces such as pin cells, and a pre-homogenization technique is needed to deal with cells containing fuel pins. Recently the MSC has been extended to heterogeneous Cartesian cells (HCC) (Masiello, 2004; Masiello, Sanchez, et al., 2009). The heterogeneous cell is composed by an external rectangular surface containing an arbitrary number of concentric and homogeneous rings, thus representing the typical fuel-cladding-moderator geometry found in fuel pins (see Figure 1.2). The introduction of heterogeneous cells into IDT permits the analysis of PWR assemblies and bundles in the exact geometry, and can be seen as an effort to enable the accurate and detailed study of a whole core in transport theory.

Numerical codes conceived to solve transport theory are based on a given angular representation. IDT implements the discrete ordinates method (S_N), where an ensemble of discrete directions and associated weights are used to reconstruct the integral over the angular variable. The resulting large system of algebraic equations is solved by source iteration. This is the classical method used with the discrete ordinates codes. While it is proven to enable accurate solutions, its convergence can be very slow, especially in weakly-absorbing media. This is due

to its intrinsic solution strategy, where each iteration n corresponds to the determination of the angular flux for neutron having collided n times. Therefore a large number of iterations is needed when the ratio between the scattering and the total cross section is close to 1. Also, slow convergence can result in *false convergence*, i.e. the interruption of the iterative scheme due to the apparent reached convergence due the slow variation of the angular flux determined in consequent iterations. Acceleration techniques are employed to lighten the computational effort in terms of CPU time and to avoid the effect of false convergence. In this way, simulations becomes less expensive and it is possible to investigate larger systems in a more detailed way.

In this chapter we focus our attention to the transport synthetic acceleration (TSA). It is a class of acceleration schemes where a low order transport operator is used to speed-up the convergence of the full transport operator. Typically, a coarser angular representation is considered in the TSA. In particular, the Boundary Projection Acceleration implements the low order transport operator at the boundaries of the geometrical mesh. In the following we present the mathematical and numerical implementation of the Boundary Projection Acceleration for the solution of the neutron transport equation for heterogeneous cells with the neutronic code IDT. After a review of the basic quantities and equations of the transport theory for neutrons, we concentrate on the solution strategy of IDT for HCC, specifying how the BPA has been incorporated for generic 2D and 3D calculations.

The C5G7 benchmark provided by the IAEA is used to test the accuracy and the effectiveness of the acceleration, for 2D and 3D geometries. We will see how the BPA effectively decrease the number of transport iteration, thus reducing the overall computation burden. Finally, we present the comparison of the BPA with a non-linear acceleration based on coarse-mesh finite differences (CMFD).¹

1.1 Neutrons transport

1.1.1 Basic quantities

In transport theory, a neutron is represented as a point particle, whose state is fully represented by its position \mathbf{r} and velocity $\mathbf{v} = v\mathbf{\Omega}$, where v is the neutron scalar speed and $\mathbf{\Omega}$ is a unit vector in its flight direction. Since neutrons are electrically neutral, their direction of motion is not influenced by external fields, and thus the paths between two successive collisions are considered straight. Neutron has

¹This work has been realized in cooperation with CEA/DEN/DANS/DM2S/SERMA/LTSD, center of Saclay, France.

spin and magnetic moment that can lead to polarization, but this effect is small in most practical situations and can be neglected (Bell and Glasstone, 1970).

With these assumptions, we can now recall the definitions of the quantities involved in the description of the neutron population inside a nuclear reactor.

The seven independent variables needed to precisely determine the state of a particle are:

- r : position, 3 components;
- Ω : flight direction, 2 angles in the spherical coordinate system;
- E : kinetic energy, or alternatively absolute value of the velocity v ;
- t : time.

The volume element in the six dimension neutron phase space is thus:

$$drd\Omega dE. \quad (1.1)$$

To describe a population of neutrons we introduce the *neutron density distribution*:

$$n(\mathbf{r}, \Omega, E, t), \quad (1.2)$$

where

$$n(\mathbf{r}, \Omega, E, t) drd\Omega dE \quad (1.3)$$

represents the number of neutrons in the phase space $drd\Omega dE$ at time t .

The product of v and the neutron angular density is called *neutron angular flux*:

$$\psi(\mathbf{r}, \Omega, E, t) = vn(\mathbf{r}, \Omega, E, t). \quad (1.4)$$

It corresponds to the total track length per unit time of all neutrons in the phase space per unit of phase space volume. As we will see below, it is the unknown quantity of the neutron balance expressed through the linear transport equation.

The integral of the angular flux over all directions is the *scalar flux*:

$$\phi(\mathbf{r}, E, t) = \int_{4\pi} d\Omega' \psi(\mathbf{r}, \Omega', E, t). \quad (1.5)$$

It is the quantity determined when a nuclear system is studied by means of diffusion theory.

We define the *angular current* as:

$$\mathbf{J}(\mathbf{r}, \Omega, E, t) = v\Omega n(\mathbf{r}, \Omega, E, t) = \Omega\psi(\mathbf{r}, \Omega, E, t), \quad (1.6)$$

such that $\hat{n} \cdot \mathbf{J}(\mathbf{r}, \boldsymbol{\Omega}, E, t) d\boldsymbol{\Omega} dE$ is the net rate of neutrons passing through a unit area having normal \hat{n} .

The production of neutrons per unit time and per unit phase space volume that is independent on the neutron density of the system is called *external source*, or simply *source*:

$$q_{\text{ext}}(\mathbf{r}, \boldsymbol{\Omega}, E, t). \quad (1.7)$$

These neutrons arise from events not connected to neutron collisions, e.g. (α, n) reactions, spontaneous fissions, cosmic rays, etc.

The probability related to a collision event is expressed through the *macroscopic cross section*:

$$\Sigma_{x,j}(\mathbf{r}, E, t), \quad (1.8)$$

that is the fractional probability of neutron interaction x with a nuclide j per unit path length traveled. This partial cross section depends on the particle emerging from a collision. In particular,

- $x = s$ represents a *scattering* event, that can be further separated in *elastic* and *inelastic* scattering;
- $x = c$ represents a *radiative capture*, i.e. the emission of gamma rays following a disappearance of a neutron;
- $x = f$ represents a *fission*, that is the emission of new neutrons from the split of a heavy isotope;
- $x = a$ is the *absorption*, i.e. the sum of capture and fission;
- $x = t$, where t is often omitted, is the sum of all preceding collision events.

As we have in general a multitude of nuclei, the overall cross section of the mixture is calculated summing the partial contribution of each isotope:

$$\Sigma_x(\mathbf{r}, E, t) = \sum_{j=1}^J \Sigma_{x,j}(\mathbf{r}, E, t). \quad (1.9)$$

The reciprocal of the total Σ is the *neutron mean free path*, or *mfp*. The variation of $\Sigma_{x,j}$ with time may arise from fuel depletion or *burnup*, but it is so slow that may be easily separable from the neutron transport problem. In the following, it will be assumed constant in time. In addition, the macroscopic cross section is related to the *microscopic cross section* $\sigma_{x,j}(E)$ according to the relation:

$$\Sigma_{x,j}(\mathbf{r}, E) = N_j(\mathbf{r})\sigma_{x,j}(E), \quad (1.10)$$

where $N_j(\mathbf{r})$ is the nuclear atomic density of the nuclide j computed as

$$N = \frac{\rho A_0}{M}, \quad (1.11)$$

with ρ the density of the material, A_0 the Avogadro number, and M the atomic mass of the nuclide. The value of the cross section is strongly dependent on the energy of the impinging neutron, and for this reason we need to accurately determine the neutron population also with respect to the energy variable.

Since the macroscopic cross section is the probability that a neutron will undergo a particular reaction per unit distance, the product $v\Sigma_x$ is the corresponding probability per unit time. Having the angular density of neutrons $n(\mathbf{r}, \boldsymbol{\Omega}, E, t)$, the *interaction rate* or *reaction rate* is:

$$v\Sigma_x(\mathbf{r}, E)n(\mathbf{r}, \boldsymbol{\Omega}, E, t) = \Sigma_x(\mathbf{r}, E)\psi(\mathbf{r}, \boldsymbol{\Omega}, E, t), \quad (1.12)$$

that gives the number of interaction x at position \mathbf{r} per unit phase space volume per unit time. The total number of interactions (or collisions) is obtained by using the total macroscopic cross section $\Sigma(\mathbf{r}, E)$. Since each fission releases an amount of energy, we can determinate the distribution of thermal power with the reactor knowing the fission reaction rate.

In neutron transport theory, neutrons emitted by fission are usually considered independent on velocity and direction of the neutron from which they originate. On the contrary, to properly describe a scattering event it is required to determine the energy and flight direction of neutrons emerging after the collision. This relation is express through the *law of deflection* or *differential scattering kernel*:

$$P(\boldsymbol{\Omega}' \rightarrow \boldsymbol{\Omega}, E' \rightarrow E)d\boldsymbol{\Omega}dE, \quad (1.13)$$

that represents the probability of scattering from direction $\boldsymbol{\Omega}'$ and energy E to the direction interval $d\boldsymbol{\Omega}$ about $\boldsymbol{\Omega}$ with energy in dE about E . The neutrons emerging from a scattering event, either elastic or inelastic, emerges from each neutron colliding with a nucleus. The transfer probabilities may consequently normalized to 1:

$$\int_0^\infty dE \int_{4\pi} d\boldsymbol{\Omega}' P(\boldsymbol{\Omega}' \rightarrow \boldsymbol{\Omega}, E' \rightarrow E) = 1 \quad (1.14)$$

The dependence on temperature of the differential scattering kernel will be considered extensively in Chapter 2.

The *differential cross section* for a generic nuclear interaction x may be expressed as the product of the scattering cross section and the scattering kernel:

$$\Sigma_s(\mathbf{r}, \boldsymbol{\Omega}' \rightarrow \boldsymbol{\Omega}, E' \rightarrow E) = \Sigma_s(\mathbf{r}, E')P(\boldsymbol{\Omega}' \rightarrow \boldsymbol{\Omega}, E' \rightarrow E). \quad (1.15)$$

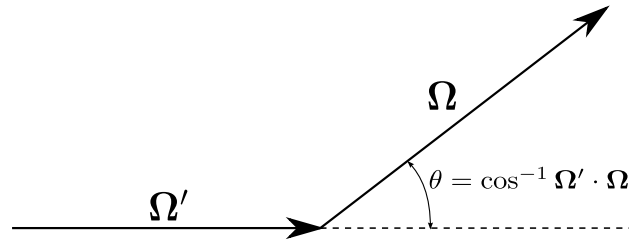


Figure 1.3 Deviation angle for an elastic scattering.

Even though the scattering law is independent of position, the scattering cross section includes the atomic density, and subsequently the differential cross section can provide a spatial variation.

In the following, we assume an *isotropic medium*, neglecting anisotropy that can arise from particular crystal configurations. Under this approximation, the interaction cross sections are independent on the angular direction Ω of the hitting neutrons. Also, the differential transfer cross section is supposed *rotationally invariant*: it does not depend on the directions of Ω' and Ω before and after the collisions, but only on the deviation angle Θ in the laboratory system, or its cosine $\mu_0 = \Omega' \cdot \Omega$ (see Figure 1.3):

$$\Sigma_s(\mathbf{r}, \Omega' \rightarrow \Omega, E' \rightarrow E) = \Sigma_s(\mathbf{r}, \Omega' \cdot \Omega, E' \rightarrow E) \quad (1.16)$$

The energy distribution of fission neutrons is represented with the *fission spectrum*:

$$\chi(E), \quad (1.17)$$

where $\chi(E)dE$ gives the probability of a fission neutron appearing within dE about E . We note that the neutron fission spectrum is assumed to be independent on the energy of the incident neutron. The function $\chi(E)$ is normalized to 1:

$$\int_0^{\infty} dE \chi(E) = 1. \quad (1.18)$$

Neutrons emerging from the fission are emitted promptly during the reaction, or after a delay. Since we intend to analyze the steady-state neutron balance, all delayed neutrons are assumed to be included with prompt neutrons. Furthermore, it is a good approximation to consider all the fission neutrons to be emitted isotropically in the laboratory system: this will lead to a 4π normalization factor for the fission contribution in the neutron balance.

Last but not least, the average number of neutrons produced per fission is denoted with:

$$\nu(E). \quad (1.19)$$

Its energy dependence can be directly included into the fission cross section, i.e.:

$$\nu(E)\Sigma_f(\mathbf{r}, E) = \nu\Sigma_f(\mathbf{r}, E). \quad (1.20)$$

1.1.2 Integro-differential neutron balance

Having defined the quantities normally used in neutron transport theory, we shall now proceed in the derivation of the neutron balance in the phase space, writing the *Boltzmann neutron transport equation* in integro-differential form.

As stated in the introduction, in reaction physics the neutron-neutron interactions can be safely neglected due to the very low “neutron gas” density compared to the atomic density of the surrounding medium. Also, the average spontaneous disintegration time of a neutron is many order of magnitude larger than the typical life of a neutron inside a reactor ($\approx 10^{-5} \div 10^{-7}$ s), and thus for our purposes neutrons can be considered as stable particles.

The variation of the neutron population into the unit phase space volume between t and $t + dt$ is denoted by:

$$[n(\mathbf{r}, \mathbf{\Omega}, E, t + dt) - n(\mathbf{r}, \mathbf{\Omega}, E, t)] drd\mathbf{\Omega}dE = \frac{\partial}{\partial t}n(\mathbf{r}, \mathbf{\Omega}, E, t)drd\mathbf{\Omega}dE = \frac{1}{v}\frac{\partial}{\partial t}\psi(\mathbf{r}, \mathbf{\Omega}, E, t)drd\mathbf{\Omega}dE. \quad (1.21)$$

It is controlled by four physical phenomena:

- particle streaming;
- losses by collision;
- arrivals due to scattering;
- sources (fission and external).

The neutron balance is then obtained by equaling the variation of the population (1.21) and the sum all these contributions.

Particle streaming is due to neutrons escaping the phase space unit volume, and can be described using the concept of angular current. Denoting with dS an element of the surface of $d\mathbf{r}$ having normal \hat{n} , the net number of neutrons with direction $\mathbf{\Omega}$ about $d\mathbf{\Omega}$ and energy E within dE crossing dS during dt is:

$$\mathbf{J}(\mathbf{r}, \mathbf{\Omega}, E, t) \cdot \hat{n} dSd\mathbf{\Omega}dEdt = \mathbf{\Omega}\psi(\mathbf{r}, \mathbf{\Omega}, E, t) \cdot \hat{n} dSd\mathbf{\Omega}dEdt \quad (1.22)$$

Integrating over the contour surface ∂V enclosing a volume V , we find the number of neutrons with direction $\mathbf{\Omega}$ about $d\mathbf{\Omega}$ and energy E within dE exiting $d\mathbf{r}$ during

d. Making use of the Gauss's divergence theorem we have:

$$\oint_{\partial V} dS \hat{n} \cdot \mathbf{J}(\mathbf{r}, \boldsymbol{\Omega}, E, t) d\boldsymbol{\Omega} dE dt = \int_V d\mathbf{r} \nabla \cdot \boldsymbol{\Omega} \psi(\mathbf{r}, \boldsymbol{\Omega}, E, t) d\boldsymbol{\Omega} dE dt. \quad (1.23)$$

Remembering that $(\nabla \cdot \boldsymbol{\Omega}) = 0$ and using the vectorial identity $\nabla \cdot (f\mathbf{g}) = \mathbf{g} \cdot \nabla f + f \nabla \cdot \mathbf{g}$, we can write:

$$\nabla \cdot \boldsymbol{\Omega} \psi(\mathbf{r}, \boldsymbol{\Omega}, E, t) = \boldsymbol{\Omega} \cdot \nabla \psi(\mathbf{r}, \boldsymbol{\Omega}, E, t). \quad (1.24)$$

Losses by collisions are described using the concept of reaction rate. The neutrons in the phase space element $d\mathbf{r}d\boldsymbol{\Omega}dE$ can disappear due to a collision, either absorption or scattering into another energy or direction. The probability per unit length of this phenomenon is expressed using the total macroscopic cross section. Therefore, the number of neutrons that disappear in the unit phase space volume during dt is:

$$\Sigma(\mathbf{r}, \boldsymbol{\Omega}, E, t) \psi(\mathbf{r}, \boldsymbol{\Omega}, E, t) d\mathbf{r}d\boldsymbol{\Omega}dE dt. \quad (1.25)$$

If a collision is not an absorption, the impinging neutron is re-emitted with a different velocity (represented though is direction vector and its corresponding kinetic energy). This event is represented using the differential scattering cross section. Thus, the number of neutrons transferred from direction $\boldsymbol{\Omega}'$ and energy E' to direction $\boldsymbol{\Omega}$ and energy E in the unit phase space volume during d is:

$$\Sigma_x(\mathbf{r}, \boldsymbol{\Omega}' \cdot \boldsymbol{\Omega}, E' \rightarrow E) \psi(\mathbf{r}, \boldsymbol{\Omega}', E', t) d\mathbf{r}d\boldsymbol{\Omega}dE dt. \quad (1.26)$$

The *arrivals due to scattering* are therefore computed integrating over all the starting directions $\boldsymbol{\Omega}'$ and energies E' :

$$\int_0^\infty dE' \int_{4\pi} d\boldsymbol{\Omega}' \Sigma_x(\mathbf{r}, \boldsymbol{\Omega}' \cdot \boldsymbol{\Omega}, E' \rightarrow E) \psi(\mathbf{r}, \boldsymbol{\Omega}', E', t) d\mathbf{r}d\boldsymbol{\Omega}dE dt. \quad (1.27)$$

Finally, the *source term* is composed by the sum of two contributions: *fissions* and *external sources*. The former is expressed using the fission spectrum and the average number of neutrons produced per fission. Considering as usual the phase space unit volume in the time interval dt , the arrival of neutrons from fission is computed integrating over all the incoming directions and energies of the impinging neutron:

$$\frac{\chi(E)}{4\pi} \int_0^\infty dE' \int_{4\pi} d\boldsymbol{\Omega}' \nu(E') \Sigma_f(\mathbf{r}, E', t) \psi(\mathbf{r}, \boldsymbol{\Omega}', E', t) d\mathbf{r}d\boldsymbol{\Omega}dE dt. \quad (1.28)$$

The total source term in the phase space unit volume during dt is then given by:

$$\left[q_{\text{ext}}(\mathbf{r}, \boldsymbol{\Omega}, E, t) + \frac{\chi(E)}{4\pi} \int_0^\infty dE' \int_{4\pi} d\boldsymbol{\Omega}' v(E') \Sigma_f(\mathbf{r}, E', t) \psi(\mathbf{r}, \boldsymbol{\Omega}', E', t) \right] d\mathbf{r} d\boldsymbol{\Omega} dE dt. \quad (1.29)$$

Upon inserting all the contributions (1.22), (1.25), (1.27), and (1.29) of the balance (1.21), the result is (Bell and Glasstone, 1970):

$$\left[\frac{1}{v} \frac{\partial}{\partial t} + \boldsymbol{\Omega} \cdot \nabla + \Sigma(\mathbf{r}, E, t) \right] \psi(\mathbf{r}, \boldsymbol{\Omega}, E, t) = \int_0^\infty dE' \int_{4\pi} d\boldsymbol{\Omega}' \Sigma_s(\mathbf{r}, \boldsymbol{\Omega}' \cdot \boldsymbol{\Omega}, E' \rightarrow E, t) \psi(\mathbf{r}, \boldsymbol{\Omega}', E', t) + \frac{\chi(E)}{4\pi} \int_0^\infty dE' \int_{4\pi} d\boldsymbol{\Omega}' v(E') \Sigma_f(\mathbf{r}, E') \psi(\mathbf{r}, \boldsymbol{\Omega}', E', t) + q_{\text{ext}}(\mathbf{r}, \boldsymbol{\Omega}, E, t). \quad (1.30)$$

It is an integro-differential equation of the first order, integral with respect to $\boldsymbol{\Omega}$ and E , and differential with respect to \mathbf{r} and t . The right hand side of (1.30) represents the arrivals in the phase space unit volume due to scattering, fission, and external source. In the following we may indicate it simply with $Q(\mathbf{r}, \boldsymbol{\Omega}, E, t)$.

1.1.3 Interface and boundary conditions

Inside a nuclear reactor many materials are present, and the geometrical configuration of the core can be very complex. While the cross sections can be assumed continuous functions inside each material, at the interfaces between different spatial regions they are discontinuous. At such interfaces it is necessary to deal with the neutron transport equation considering these discontinuities. However, the neutron angular flux itself described by (1.30) does not change merely crossing a physical interfaces. As a consequence the neutron transport equation should be applied at both sides, applying the condition of continuity of the angular flux.

Different considerations apply for the external boundaries of the system to be analyzed. In general, the region of interest is supposed to have a convex external surface, i.e. each straight segment connecting two points of the domain lies entirely within the region. Under this condition, a neutron leaving this spatial domain cannot intersect its surface again. Therefore, for the closure of the mathematical problem of (1.30) we need know the distribution of the angular flux in the boundary ∂V that enters into the spatial domain taken into account, namely:

$$\psi(\mathbf{r}_s, \boldsymbol{\Omega}, E, t) \quad \text{for} \quad \mathbf{r}_s \in \partial V \quad \hat{n} \cdot \boldsymbol{\Omega} < 0. \quad (1.31)$$

At first, we recall the *albedo boundary condition*, that relates the outgoing angular flux with the incoming one:

$$\psi(\mathbf{r}_s, \mathbf{\Omega}, E, t) = \beta \psi(\mathbf{r}_s, \mathbf{\Omega}', E, t). \quad (1.32)$$

Vacuum condition is achieved with $\beta = 0$, and total reflection with $\beta = 1$. Intermediate values of β represent partial reflection.

Then, we mention the boundary conditions that exploit symmetry of the geometry:

- *specular reflection*:

$$\psi(\mathbf{r}_s, \mathbf{\Omega}, E, t) = \psi(\mathbf{r}_s, \mathbf{\Omega} - 2\hat{n}(\mathbf{\Omega} \cdot \hat{n}), E, t) \quad \text{for} \quad \hat{n} \cdot \mathbf{\Omega} < 0; \quad (1.33)$$

- *translation*:

$$\psi(\mathbf{r}_s + \Delta \mathbf{r}, \mathbf{\Omega}, E, t) = \psi(\mathbf{r}_s, \mathbf{\Omega}, E, t); \quad (1.34)$$

- *rotation*:

$$\psi(\mathbf{r}_s, \mathbf{\Omega} + \Delta \mathbf{\Omega}, E, t) = \psi(\mathbf{r}_s, \mathbf{\Omega}, E, t). \quad (1.35)$$

They are very useful to reduce the computational domain, in order to study the reactor or the fuel assembly considering a reduced domain (e.g. 1/4 of a reactor).

1.1.4 Eigenvalue problem

From physical consideration, a nuclear system can be regarded as being either subcritical, critical, or supercritical, based on the behavior of the neutron population as a function of time. Given an initial non-zero neutron density, the system is said to be *subcritical* if the neutron population decreases over time, *critical* if it remains constant, and *supercritical* if it diverges. A critical system is therefore reacted when a reactor is capable of maintaining a steady neutron population, and consequently a steady energy production, in absence of source.

Since we are interested in steady state analysis of a nuclear reactor, in the following we eliminate the temporal variation in (1.30). However, the material composition of a reactor changes continuously over time, and thus a perfect critical state cannot be reached. For example, the steady state inside a power reactor is maintained by adjusting the control bar level, i.e. controlling the amount of absorptions.

From the mathematical point of view, the balance of (1.30) needs to be adjusted where the time derivative and the external sources are eliminated. This can be done by rescaling the various contributions. A typically choice is to divide the

neutron generation from fission by the *effective multiplication factor* k , that measures the ratio between two successive neutron populations:

$$[\mathbf{\Omega} \cdot \nabla + \Sigma(\mathbf{r}, E)] \psi(\mathbf{r}, \mathbf{\Omega}, E) = \int_0^\infty dE' \int_{4\pi} d\mathbf{\Omega}' \Sigma_s(\mathbf{r}, \mathbf{\Omega}' \cdot \mathbf{\Omega}, E' \rightarrow E) \psi(\mathbf{r}, \mathbf{\Omega}', E') + \frac{\chi(E)}{4\pi} \int_0^\infty dE' \int_{4\pi} d\mathbf{\Omega}' \frac{\nu(E')}{k} \Sigma_f(\mathbf{r}, E') \psi(\mathbf{r}, \mathbf{\Omega}', E') \quad (1.36)$$

The reactor is therefore said to be subcritical, critical, or supercritical if $k < 1$, $k = 1$, and $k > 1$, respectively.

Equation (1.36) depicts an *eigenvalue problem*. The trivial solution $\psi(\mathbf{r}, \mathbf{\Omega}, E) = 0$ obviously are not of our interest. We may note that given $\psi(\mathbf{r}, \mathbf{\Omega}, E)$ a non-trivial solution $C\psi(\mathbf{r}, \mathbf{\Omega}, E)$ is always a solution of the eigenvalue problem. This means that the normalization of the angular flux is arbitrary. For engineering applications, the constant C can be found from the value of the thermal power of the reactor, by multiplying the angular flux per the amount of energy released in each fission, and integrating on the entire core.

1.1.5 Integral formulation

The transport of neutrons in the phase space is to be regarded as a both local and extended phenomenon. In fact, the formulation of the neutron transport equation presented so far involves derivatives in space and time and integrals in energy and angle. In a collision, the position and time associated with a neutron change in a continuous manner, while the energy and the angle present discontinuities. So the mathematical form of the transport equation must contains integral over energy and angle: an equivalent differential-only form does not exist.

However, by representing the inversion of the transport operator along the flight direction of neutrons $\mathbf{\Omega}$, it is possible to reformulate the transport problem into an integral-only form. This procedure is know as the *method of characteristics*. A characteristic is a straight line with direction $\mathbf{\Omega}$ corresponding to a particle trajectory. We intend to study the transport of neutron along these lines.

Let's consider a characteristic with direction $\mathbf{\Omega}$. The reference position along this line is called \mathbf{r}_s , that is the intersection with the entering surface of ∂V . The position of each point lying over $\mathbf{\Omega}$ can be expressed with:

$$\mathbf{r} = \mathbf{r}_s + l\mathbf{\Omega}, \quad (1.37)$$

where l is the length of the segment traveled over the characteristic. This segment can be measured in mean free paths, leading to the definition of *optical path*:

$$\tau(l, E) = \int_0^l dl' \Sigma(\mathbf{r} + l'\mathbf{\Omega}, E). \quad (1.38)$$

At the same time, the generic time t can be referred to the neutron speed v as

$$t = t_0 + \frac{l}{v}, \quad (1.39)$$

where t_0 is the instant on which the neutron considered lies on the reference point \mathbf{r}_s .

The first two terms at the left hand side of (1.30) can be expressed making use of the concept of total derivative, expressing the $\nabla \cdot \mathbf{\Omega}$ in Cartesian coordinates:

$$\frac{d}{dl} = \frac{1}{v} \frac{\partial}{\partial t} + \Omega_x \frac{\partial}{\partial x} + \Omega_y \frac{\partial}{\partial y} + \Omega_z \frac{\partial}{\partial z} = \frac{dt}{dl} \frac{\partial}{\partial t} + \frac{dx}{dl} \frac{\partial}{\partial x} + \frac{dy}{dl} \frac{\partial}{\partial y} + \frac{dz}{dl} \frac{\partial}{\partial z}. \quad (1.40)$$

With this definition it is possible to rewrite the neutron transport equation as:

$$\frac{d}{dl} \psi \left(\mathbf{r}_s + l\mathbf{\Omega}, \mathbf{\Omega}, E, t_0 + \frac{l}{v} \right) + \Sigma \left(\mathbf{r}_s + l\mathbf{\Omega}, E, t_0 + \frac{l}{v} \right) \psi \left(\mathbf{r}_s + l\mathbf{\Omega}, \mathbf{\Omega}, E, t_0 + \frac{l}{v} \right) = Q \left(\mathbf{r}_s + l\mathbf{\Omega}, \mathbf{\Omega}, E, t_0 + \frac{l}{v} \right). \quad (1.41)$$

The latter is a first order linear differential equation, that can be solved with the usual methods of calculus with the angular flux at (\mathbf{r}_s, t_0) as boundary condition, leading to:

$$\psi(\mathbf{r}, \mathbf{\Omega}, E, t) = \psi(\mathbf{r}_s, \mathbf{\Omega}, E, t_0) e^{-\tau(l, E)} + \int_0^l ds e^{-\tau(s, E)} Q(\mathbf{r}_s + s\mathbf{\Omega}, \mathbf{\Omega}, E, t_0 + s/v) \quad (1.42)$$

It is worth to note that angular flux in a generic position \mathbf{r} is dependent on the source, the optical path, and the entering contribution. This will be the basis of the numerical implementation of method of characteristics, both for the balance and the transmission equation, as we will see in the next sections.

In the integro-differential formulation of the transport problem, the contribution to the angular flux of the particles emitted is local (that is to say at the same point \mathbf{r}) and the coupling with the other points is obtained through the operator $\mathbf{\Omega} \cdot \nabla$. On the contrary, in the integral form the spatial coupling is achieved via the source term Q . This suggests a possible numerical solution strategy. If the explicit form of $Q(\mathbf{r}_s + s\mathbf{\Omega}, \mathbf{\Omega}, E, t_0 + s/v)$ is introduced in (1.42), the result may be written as:

$$\psi = \mathbf{K}\psi + Q', \quad (1.43)$$

where \mathbf{K} is the integral operator, and Q' a known function. The solution of (1.43) can be sought by iteration:

$$\begin{aligned}\psi_0 &= Q', \\ \psi_1 &= \mathbf{K}\psi_0, \\ &\vdots \\ \psi_{n+1} &= \mathbf{K}\psi_n.\end{aligned}$$

Physically ψ_0 is the angular flux of uncollided neutrons emerging after the introduction of independent source Q' . At the same time, ψ_1 is the angular flux of first-collision neutrons. Similarly, ψ_i is the angular flux of neutrons that have made i collisions. The solution of (1.43) can be found if this series converges. This procedure, called *source iteration*, will be the approach used to solve the neutron transport equation within IDT.

1.2 Discretization of transport equation

Numerical solution of the transport equation requires the discretization of the variables describing the position of the neutron in the phase space. In this section we present the approach usually employed for the variables E , Ω , and r . More specifically, we will deal with the multigroup approximation, the method of discrete ordinates, and the spatial representation of the angular flux.

1.2.1 Energy variable

The energy discretization is achieved via the *multigroup* approximation, i.e. by partitioning the total interval of interest into G energy groups defined so that:

$$\Delta E_g = [E_g, E_{g-1}] \quad \text{for} \quad g = 1, \dots, G, \quad (1.44)$$

where $g = 1$ corresponds to the highest energy group, and $g = G$ to the lowest.

In this way the cross sections and the angular flux are no more continuous functions in energy, but are constants in the energy domain inside each group. The group averaged angular and scalar fluxes are obtained by integration, namely:

$$\psi^g(\mathbf{r}, \Omega) = \int_{E_g}^{E_{g-1}} dE \psi(\mathbf{r}, \Omega, E), \quad (1.45)$$

$$\phi^g(\mathbf{r}) = \int_{E_g}^{E_{g-1}} dE \phi(\mathbf{r}, E) \quad (1.46)$$

The formal definition for the group-averaged cross section is found by preserving the reaction rate within each group (Hébert, 2009), say:

$$\Sigma^g(\mathbf{r}) = \frac{\int_{\Delta E_g} dE \Sigma(\mathbf{r}, E) \phi(\mathbf{r}, E)}{\phi^g(\mathbf{r})}. \quad (1.47)$$

However, we notice that to calculate the group parameters we need the angular flux, that is the solution of the problem. This source of non-linearity can be avoided in the preparation of the library of group cross section by assuming a spatial independent function $\phi(E)$ that works as an integration weight. Typically, it comes from an infinite-medium approximation representing of the spectrum of the core or of a spatial subdomain of interest (Sanchez, 2012b).

The multigroup approximation transforms the neutron transport equation into a system of G equations, where each energy group describes a one-speed balance. The coupling between these groups is obtained through the scattering integral and the fission term, according to the physical collision process. Three macro regions are defined: *fast* (10 MeV ÷ 300 keV), *epithermal* (300 keV ÷ 0.625 eV), and *thermal* (0.625 eV ÷ 0.001 eV). While in the fast and epithermal regions scattering mainly decreases the energy of the neutron (down-scattering), in the thermal region a neutron can acquire energy from a collision (up-scattering). In the formers the solution is obtained by a cascade, i.e. by proceeding from the highest group to the slower ones. Instead, In the latters an iterative solution is needed. Finally, the multigroup solution is found by iteration on the fission source.

In each energy group we may write the transport balance as:

$$L^g \psi^g(\mathbf{r}, \boldsymbol{\Omega}) = H^{g:g} \psi^g(\mathbf{r}, \boldsymbol{\Omega}) + \sum_{g' \neq g} H^{g':g} \psi^{g'}(\mathbf{r}, \boldsymbol{\Omega}) + (F\psi)^g(\mathbf{r}) + q_{\text{ext}}^g(\mathbf{r}, \boldsymbol{\Omega}) \quad (1.48)$$

where:

- L^g is the one-group transport operator

$$L^g = \boldsymbol{\Omega} \cdot \nabla + \Sigma^g \quad (1.49)$$

- $H^{g:g} \psi^g(\mathbf{r}, \boldsymbol{\Omega})$ is the scattering events inside the energy group considered

$$H^{g:g} \psi^g(\mathbf{r}, \boldsymbol{\Omega}) = \int_{4\pi} d\boldsymbol{\Omega}' \Sigma_s^{g \rightarrow g}(\mathbf{r}, \boldsymbol{\Omega}' \cdot \boldsymbol{\Omega}) \psi^g(\mathbf{r}, \boldsymbol{\Omega}') \quad (1.50)$$

- $H^{g':g} \psi^{g'}(\mathbf{r}, \boldsymbol{\Omega})$ represents the scattering contribution arriving from other groups

$$H^{g':g} \psi^{g'}(\mathbf{r}, \boldsymbol{\Omega}) = \int_{4\pi} d\boldsymbol{\Omega}' \Sigma_s^{g' \rightarrow g}(\mathbf{r}, \boldsymbol{\Omega}' \cdot \boldsymbol{\Omega}) \psi^{g'}(\mathbf{r}, \boldsymbol{\Omega}') \quad (1.51)$$

- $(F\psi)^g(\mathbf{r})$ is the contribution of fission in group g

$$(F\psi)^g(\mathbf{r}) = \chi^g(\mathbf{r}) \sum_{g'=1}^G \int_{4\pi} d\Omega v \Sigma_f^{g'}(\mathbf{r}) \psi^{g'}(\mathbf{r}, \Omega) \quad (1.52)$$

- $q_{\text{ext}}^g(\mathbf{r}, \Omega)$ the external source.

1.2.2 Angular variable

The numerical approximation of the transport equation requires an angular discretization. There are two numerical techniques employed: spherical harmonics (P_N) and discrete ordinates (S_N).

The former is a projection method, in which the angular flux is expanded in series assuming as basis functions the spherical harmonics spanning on a subspace invariant by orthogonal transformations,

$$\psi(\Omega) = \sum_h A_h(\Omega) \psi_h, \quad (1.53)$$

$$\psi_h = \int_{4\pi} d\Omega A_h(\Omega) \psi(\Omega), \quad (1.54)$$

where $A_h(\Omega)$ represent the real spherical harmonics of order h (the indices ℓ and m have been collapsed into a single index h), and ψ_h is the flux moment of order h . The solution is achieved by truncating the sum at the order N , and solving the system of resulting equations. The coupling among the moments occurs through the streaming term, and the scattering integral is diagonalized. Although the anisotropy of the scattering is accurately represented, this method results in bigger and more cumbersome numerical implementations.

In reactor physics the more popular way to represent the angular dependence of the angular flux is through the *discrete ordinates* or S_N method. It originates from the seminal work of Chandrasekhar (1960) and it has been proposed for neutron transport applications by Carlson and Bell (1958). Basically, it is a collocation method for the angular variable, where a quadrature formula

$$S_N = \{w_d, \Omega_d\}_{d=1, D(N)} \quad (1.55)$$

is introduced to represent the scattering integral. The number of angles is a function of N , an even integer. In this way we obtain a system of equations for every node in the angular representation. The coupling of these equations occurs in the scattering integral, and the streaming term is diagonalized. Under some circumstances, a S_N method can be constructed in a way to satisfy also a related set of

P_N equations (Sanchez, 2012a). IDT is based on this technique, and therefore in the following we assume always this angular discretization.

The S_N method is plagued by a number of problems, such as numerical dispersion and, more importantly the *ray effect*. The latter results in nonphysical behavior of the numerical solution, and it particularly strong in the presence of localized sources and regions dominated by strong absorption properties (Lathrop, 1968). However, discrete ordinates methods are very appealing, since they lead in a natural way to stable iterative solutions based on source iterations (Sanchez, 2012b). Generally, ray effect anomalies are mitigated by increasing the angular representation and by selecting an appropriate quadrature formula, able to correctly represent the angular flux in the domain of interest and given the actual anisotropy of scattering to be taken into account.

We shall now proceed in a brief description of the S_N method. Since we are considering isotropic media, the differential scattering cross section depends only on the cosine of deviation angle $\mu_0 = \mathbf{\Omega}' \cdot \mathbf{\Omega}$, that it bounded between -1 and 1 . For a specific energy group², it can be represented with a Legendre polynomial expansion

$$\Sigma_s(\mathbf{r}, \mu_0) = \frac{1}{4\pi} \sum_{\ell=0}^L (2\ell + 1) \Sigma_{s,\ell}(\mathbf{r}) P_\ell(\mu_0), \quad (1.56)$$

where

$$\Sigma_{s,\ell}(\mathbf{r}) = 2\pi \int_{-1}^{+1} d\mu_0 \Sigma_s(\mathbf{r}, \mu_0) P_\ell(\mu_0), \quad (1.57)$$

and L is the anisotropy order of the scattering (e.g. $L = 0$ for a isotropic scattering, $L = 1$ for a linearly anisotropic scattering, etc.). At the same time, the representation of angular flux in spherical harmonics is

$$\psi(\mathbf{r}, \mathbf{\Omega}) = \sum_{\ell=0}^L \frac{2\ell + 1}{4\pi} \sum_{m=-\ell}^{\ell} \phi_\ell^m(\mathbf{r}) A_\ell^m(\mathbf{\Omega}), \quad (1.58)$$

where $\psi_\ell^m(\mathbf{r})$ is the moment of the angular flux with respect to the spherical harmonic $A_\ell^m(\mathbf{\Omega})$, namely

$$\phi_\ell^m(\mathbf{r}) = \int_{4\pi} d\mathbf{\Omega} \psi(\mathbf{r}, \mathbf{\Omega}) A_\ell^m(\mathbf{\Omega}). \quad (1.59)$$

Making use of the addition theorem of the spherical harmonics

$$P_\ell(\mathbf{\Omega}' \cdot \mathbf{\Omega}) = \sum_{m=-\ell}^{\ell} A_\ell^m(\mathbf{\Omega}') A_\ell^m(\mathbf{\Omega}), \quad (1.60)$$

²the group index is here suppressed for the sake of simplicity and clarity

the integral of the source of scattering is transformed to

$$Q_{\text{scatt}}(\mathbf{r}, \boldsymbol{\Omega}) = \sum_{\ell=0}^L \Sigma_{s,\ell}(\mathbf{r}) \sum_{m=-\ell}^{\ell} A_{\ell}^m(\boldsymbol{\Omega}) \int_{4\pi} d\boldsymbol{\Omega}' \psi(\mathbf{r}, \boldsymbol{\Omega}') A_{\ell}^m(\boldsymbol{\Omega}') \quad (1.61)$$

and, considering (1.59), we may write:

$$Q_{\text{scatt}}(\mathbf{r}, \boldsymbol{\Omega}) = \sum_{\ell=0}^L \Sigma_{s,\ell}(\mathbf{r}) \sum_{m=-\ell}^{\ell} A_{\ell}^m(\boldsymbol{\Omega}) \phi_{\ell}^m(\mathbf{r}). \quad (1.62)$$

The S_N methodology is applied by substituting (1.59) with a numerical integration based on (1.55):

$$\phi_{\ell}^m(\mathbf{r}) \simeq \sum_{d=1}^{D(N)} w_d A_{\ell}^m(\boldsymbol{\Omega}_d) \psi_d(\mathbf{r}) \quad (1.63)$$

where $\psi_d(\mathbf{r}) = \psi(\mathbf{r}, \boldsymbol{\Omega}_d)$. Upon inserting this formulation into (1.36) and considering a single energy group, we obtain a system of equations valid for each direction $\boldsymbol{\Omega}_d$ of the quadrature formula (1.55):

$$[\boldsymbol{\Omega}_d \cdot \nabla + \Sigma(\mathbf{r})] \psi(\mathbf{r}, \boldsymbol{\Omega}_d) = \sum_{\ell=0}^L \Sigma_{s,\ell}(\mathbf{r}) \sum_{m=-\ell}^{\ell} A_{\ell}^m(\boldsymbol{\Omega}_d) \phi_{\ell}^m(\mathbf{r}) + Q_{\text{ext}}(\mathbf{r}, \boldsymbol{\Omega}_d), \quad (1.64)$$

where $Q_{\text{ext}}(\mathbf{r}, \boldsymbol{\Omega}_d)$ are the sources external to the energy group considered (i.e. scattering from other groups and fission). Numerical iteration using (1.64) and (1.63) are at the basis of the S_N methodology.

The quadrature formula of (1.55) have to be chosen carefully. Because the angular flux can be formally expanded into spherical harmonics, the directions and the weights should be determined to exactly integrate a maximum number of spherical harmonics. A typical choice is the *level symmetric* quadrature, where nodes are determined using planar and rotational symmetries between the axis, and weights are determined on the basis of a exact quadrature of a given set of spherical harmonics (Lewis and Miller, 1984). Another possibility are the product quadratures. Often, a Gauss-Legendre quadrature is used for the cosine of the polar angle and a Chebyshev uniform quadrature is used for the azimuthal angle. While this product quadrature assures that all the weights are positive, it tends to concentrate the nodes around the polar axis, wasting angular directions. Also, Galerkin quadratures have been conceived to maximize the number of spherical harmonics exactly integrated (Sanchez and Ragusa, 2011). In the following we assume a generic angular quadrature, and in the section dedicated at the numerical results we present the different behavior of the acceleration scheme varying the quadrature formula.

1.2.3 Spatial variable

There are many possible spatial discretization techniques. All the methods are based on partitioning the computational domain into many smaller homogeneous subdomains. The angular flux is then determined inside each discretized region.

We consider methods based on projection of the flux spatial dependence into basis functions. In particular, we assume a local spatial development of angular flux for each direction of the S_N method. The numerical method we are interested in, i.e. the method of short characteristics, requires a pair of equations for the local resolution of the transport operator: the *balance* equation for the calculation of the volume flux inside each cell, and the *transmission* equation to evaluate the angular flux at the borders of the cells. The angular flux inside each region and at the surfaces are therefore represented as:

$$\psi(\mathbf{r}) = \sum_{i=1}^{G_\alpha} f_\alpha^i(\mathbf{r}) \psi_\alpha^i \quad \forall \mathbf{r} \in V_\alpha, \quad (1.65a)$$

$$\psi(\mathbf{r}) = \sum_{i=1}^{G_{s,\alpha}} f_{s,\alpha}^i(\mathbf{r}) \psi_{s,\alpha}^i \quad \forall \mathbf{r} \in \partial V_\alpha, \quad (1.65b)$$

where G_α and $G_{s,\alpha}$ are the volume and surface maximum order to be represented, α indicate the subdomain of the mesh discretization. Assuming an orthonormal basis, the spatial moments are defined as:

$$\psi_\alpha^i = \int_{V_\alpha} d\mathbf{r} f_\alpha^i(\mathbf{r}) \psi(\mathbf{r}), \quad (1.66a)$$

$$\psi_{s,\alpha}^i = \int_{\partial V_\alpha} dS f_{s,\alpha}^i(\mathbf{r}) \psi(\mathbf{r}), \quad (1.66b)$$

The moments of (1.66) are the unknowns to be numerically found for each angular direction Ω_d .

1.3 Solution of the transport problem

Having set the mathematical framework of the neutron transport equation and its discretization, we can now concentrate on the solution of the one-speed problem with source (coming from fission and up/down-scattering from other energy groups). Afterwards, we will see how it is possible to couple a multitude of single group calculations into a multigroup solution of the transport problem.

1.3.1 Method of short characteristics: IDT

In the last decades many numerical methods have been conceived to solve the neutron transport equation. The solutions of the transport equations are based

on three equivalent form of the basic equation: integro-differential, integral, and surface-integral (Sanchez and McCormick, 1982). Most of the methods are based on the first two formulations. The integro-differential equation describes a local balance, and the resulting iteration matrices are sparse. On the other hand, the integral formulation results in a global balance of particle in each direction. Since its coefficients are strongly coupled, the matrices describing the numerical discretization are full. It is therefore possible to write specialize routines to evaluate exactly the coefficients for a given geometrical description. In general, integral methods require an bigger memory storage. While they are able to provide a more precise representation, their application to large domains poses problem due to intense processor and memory requirements.

The balance equation assures the conservation of the number of particles. The integration of the $\Omega \cdot \nabla$ operator of (1.64) (one-speed problem) results in a integral on the surface of each spatial domain that corresponds to the neutron currents at the interfaces. For this reason, the source at the interior of the domain and the incoming angular flux are not sufficient to completely solve the transport problem. In fact, it is necessary to evaluate also the flux exiting the region of interest. This boundary condition is the mechanism that couple neighbor cell of the mesh discretization. However, additional relations should be put in place to provide this coupling. The choice of the approximation used to represent the transmission of the flux through the cells defines the type of numerical method used. Finite differences, nodal methods, and the method of characteristics are all examples of techniques to describe the transmission of neutrons. The peculiarity of the method of characteristics is that transmission equation is obtained via exact analytic representation of the propagation through mesh cells using the integral transport equation. In this way the strong gradients of the flux that can appear in a nuclear reactor are well represented. In general the *balance* and *transmission* equations for each energy group and each angular direction of the S_N method may be written as:

$$\psi = I\psi^- + CQ, \quad (1.67)$$

$$\psi^+ = T\psi^- + EQ, \quad (1.68)$$

where $\psi^\pm(\Omega)$ contains the approximation of the flux at the exiting (+) and entering (-) surfaces for the given angular direction, $\psi(\Omega)$ contains the approximation of the flux at the interior of the mesh cell, and $Q(\Omega)$ contains the sources (scattering, fission) at the interior of the mesh cell. The transport properties of each cell is described using a matrix response formulation, where:

- $I(\Omega)$ is the *incoming* matrix, that relates incoming fluxes on cell surfaces and

the in-cell angular flux;

- $C(\Omega)$ is the *collision* matrix, that quantifies the contribution that sources placed inside the cell have on the in-cell angular flux;
- $T(\Omega)$ is the *transmission* matrix, that specify how much flux entering from one side of the cell arrive at the opposite boundary;
- $E(\Omega)$ is the *escape* matrix, that indicate the contribution of source within the cell on the angular flux at the boundaries of the cell.

They contain the physical and geometrical properties of each cell. Each angle of the quadrature formula employed requires the determination of this set of response matrices, since along each trajectory Ω the material and the geometry encountered by a neutron are different.

The method of short characteristics implemented in IDT is based on projection of the balance and transmission equation on basis of polynomial functions. It is conceive the transport equation on structured 1D, 2D, or 3D Cartesian meshes. The Cartesian mesh enables a realization of dedicated routines for the calculation of the response matrices in an efficient way. Also, the regularity of mesh enables a straightforward iteration scheme, that results in fast and efficient numerical implementations. This methods is currently employed for the study of large portions of the reactor core (e.g. assembly, 1/4 of a reactor) in transport theory instead that in diffusion theory. Originally, each cell was represented as an homogeneous mixtures, requiring a pre-homogenization phase (Zmijarevic, 1998). Recently (Masiello, 2004), IDT has been extended to take into account directly rectangular meshes including concentric rings (in 2D), or prismatic cells including concentric cylinders (in 3D). This extensions, called HCC (Heterogeneous Cartesian Cell), enables the exact representation of the typical structure of fuel pin. In this way, the additional homogenization phase is no longer required and a more precise solution of the transport problem can be achieved.

The method of short characteristics requires a surface expansion of the angular flux. While in principle it could be introduced for each internal homogeneous region of the HCC, it would degrade the numerical precision of the method while increasing the computational cost. Instead, all the internal homogeneous regions are treated as a whole, like in collision probabilities method with the difference that the propagation of the neutrons is considered for each angular direction (Masiello, Sanchez, et al., 2009). Therefore, the only surface representation and projection are done on the sides of the mesh cell, preserving the algorithm structure and enabling a straightforward coupling of heterogeneous and homogeneous cells. In fact, in reactor applications we need to represent both the fuel pins and

the moderator/reflector zone, and thus a spatial discretization of a nuclear core requires both type of cells.

Lastly, we recall the problem of spatial numerical dispersion that affects the MSC. Since each mesh boundary angular flux is represented through a polynomial expansion that is assumed to be valid on all the surface, an hypothetical beam of neutron trespassing a cell without attenuation would be represented at the exiting surface not as a delta function, but as a continuous non-zero function on all the surface, leading to a numerical diffusion in space. This phenomenon appears to be more serious when different materials are present at the interior of the cell. To address this issue IDT allows the subdivision of the boundary surfaces of each cell into different parts, enabling a more detailed representation of the entering and exiting fluxes.

1.3.2 Representation of Balance and Transmission

We now concentrate on the heterogeneous Cartesian cell typical of a fuel element as it is represented in IDT. The domain V of our basic geometric is defined as

$$V = \bigcup_{\alpha=1,R} V_{\alpha}, \quad (1.69)$$

where R is the number of subdomains and α is the subdomain index. Each region inside the cell is in contact with its neighbor region via the entering and exiting surfaces. The coupling between regions is therefore based on geometrical considerations.

Figure 1.4 depicts a 2D HCC with two regions (e.g. fuel and moderator). In the following we may refer to this simple geometries in the description of the response matrices.

The angular flux and the volume sources inside each flux are expanded using Legendre polynomials:

$$\psi_{\alpha}^i(\mathbf{r}) = \sum_{i=0}^G P_{\alpha}^i(\mathbf{r}) \psi_{\alpha}^i, \quad (1.70)$$

$$Q_{\alpha}^i(\mathbf{r}) = \sum_{i=0}^G P_{\alpha}^i(\mathbf{r}) Q_{\alpha}^i, \quad (1.71)$$

where i indicates the order of the polynomial, G the number of spatial moments, and α the regions of interest. Legendre polynomials are opportunely normalize considering the actual volume V_{α} of each region.

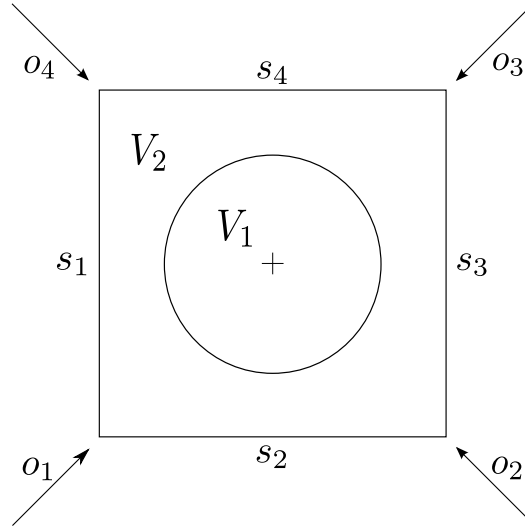


Figure 1.4 Schematic illustration of a 2D HCC with 2 regions. V_1 and V_2 are the 2 regions. $s_1, s_2, s_3,$ and s_4 are the 4 exterior surfaces. $o_1, o_2, o_3,$ and o_4 are the 4 octants.

At the same time, the development on the borders of the cell is:

$$\psi_k(\mathbf{r}_s^-) = \sum_{i_s=0}^{G_s} P_\alpha^{i_s}(\mathbf{r}_s^-) \psi_k^{i_s, -}, \quad (1.72)$$

$$\psi_k(\mathbf{r}_s^+) = \sum_{i_s=0}^{G_s} P_\alpha^{i_s}(\mathbf{r}_s^+) \psi_k^{i_s, +}, \quad (1.73)$$

where G_s is the number of degrees of freedom associated with the border of the cell, and k represents the side (x, y, z) . The basis functions are normalized considering the lengths of the borders in each direction.

Higher spatial expansions increase the precision of the representation, while raising the computational cost of the calculation. We need therefore strike a balance between these two opposite aspects. IDT implements expansions up to bilinear for the volume moments and up to linear for the surface moments, i.e.:

- volume basis: $P = (1, x, y, xy)$ (2D), $P = (1, x, y, z, xy, yz, xz)$ (3D),
- surface basis: $P_x = (1, y)$, $P_y = (1, x)$ (2D), $P_x = (1, y, z)$, $P_y = (1, x, z)$, $P_z = (1, x, y)$ (3D),

where the subscript (x, y, z) indicates the normal of the selected surface.

The balance and transmission equations for each energy group and each angular direction are obtained making use of the steady-state integral formulation

of the transport equation:

$$\psi(\mathbf{r}) = \psi(\mathbf{r}_s)e^{-\tau(l)} + \int_0^l ds e^{-\tau(s)}q(s), \quad (1.74)$$

evaluating $\psi(\mathbf{r})$ in a generic point of a region inside the cell for ψ and on the surface of the cell for ψ^+ , writing a pair of equations.

By substituting (1.70) and (1.72) inside (1.74) the integral along the characteristic line ds is transformed into a sum (polynomials can be integrated exactly). Subsequently spatial moments are obtained by projecting the integral equation on the basis functions:

$$\psi_\alpha^i = (P_\alpha^i, \psi), \quad (1.75)$$

$$\psi_k^{i_s,+} = \langle P_k^{i_s}, \psi \rangle_k^+. \quad (1.76)$$

The volume and surface integral resulting from projection (1.75) and (1.76) is computed analytically along the characteristic line and numerically in the perpendicular direction (Masiello, 2004; Masiello, Sanchez, et al., 2009).

The internal fluxes resulting from internal sources and entering fluxes are provided by (1.75), than after the integration can be recast as follows:

$$\psi_\alpha^i = \sum_{k=x,y,z} \sum_{i_s=0}^{G_s} I_k^{i,i_s} \psi_k^{i_s,-} + \sum_{\beta \neq \alpha}^R \sum_{j=0}^G C_{\alpha,\beta}^{i,j} q_\beta^j + C_{\alpha,\alpha}^{i,i} Q_\alpha^i, \quad (1.77)$$

where

- I_k^{i,i_s} represents the contribution of the moment i_s of the entrance flux from the surface k to the volume moment i ,
- $C_{\alpha,\beta}^{i,j}$ represents the contribution of the volume moment j of the internal region β to the moment i of the region α ,
- $C_{\alpha,\alpha}^{i,i}$ represents the contribution inside the region α from moment j to moment i .

The transmission of the flux among neighbor cells for a generic surface s is represented through (1.76). After projection and integration it can cast so that:

$$\psi_s^{i_s,+} = \sum_{k=x,y,z} \sum_{j_s=0}^{G_s} T_{s,k}^{i_s,j_s} \psi_k^{j_s,-} + \sum_{\beta=1}^R \sum_{j=0}^G E_{s,\beta}^{i_s,j} Q_\beta^j, \quad (1.78)$$

where

- $T_{s,k}^{i_s,j_s}$ represents the contribution of the moment j_s of the entrance surface k to the moment i_s of the exiting surface i_s ,

- $E_{s,\beta}^{i_s,j}$ represents the contribution of the moment j of the internal source in the region β to the moment i_s of the exiting surface i_s .

For the simple HCC of Figure 1.4, and indicating with the subscripts the appropriate surface or region, the balance equation is:

$$\begin{bmatrix} \psi_1 \\ \psi_2 \end{bmatrix} = \begin{bmatrix} I_{1 \rightarrow 1} & I_{2 \rightarrow 1} & I_{3 \rightarrow 1} & I_{4 \rightarrow 1} \\ I_{1 \rightarrow 2} & I_{2 \rightarrow 2} & I_{3 \rightarrow 2} & I_{4 \rightarrow 2} \end{bmatrix} \cdot \begin{bmatrix} \psi_1^- \\ \psi_2^- \\ \psi_3^- \\ \psi_4^- \end{bmatrix} + \begin{bmatrix} C_{1 \rightarrow 1} & C_{2 \rightarrow 1} \\ C_{1 \rightarrow 2} & C_{2 \rightarrow 2} \end{bmatrix} \cdot \begin{bmatrix} Q_1 \\ Q_2 \end{bmatrix} \quad (1.79)$$

and the transmission is:

$$\begin{bmatrix} \psi_1^+ \\ \psi_2^+ \\ \psi_3^+ \\ \psi_4^+ \end{bmatrix} = \begin{bmatrix} T_{1 \rightarrow 1} & T_{2 \rightarrow 1} & T_{3 \rightarrow 1} & T_{4 \rightarrow 1} \\ T_{1 \rightarrow 2} & T_{2 \rightarrow 2} & T_{3 \rightarrow 2} & T_{4 \rightarrow 2} \\ T_{1 \rightarrow 3} & T_{2 \rightarrow 3} & T_{3 \rightarrow 3} & T_{4 \rightarrow 3} \\ T_{1 \rightarrow 4} & T_{2 \rightarrow 4} & T_{3 \rightarrow 4} & T_{4 \rightarrow 4} \end{bmatrix} \cdot \begin{bmatrix} \psi_1^- \\ \psi_2^- \\ \psi_3^- \\ \psi_4^- \end{bmatrix} + \begin{bmatrix} E_{1 \rightarrow 1} & E_{1 \rightarrow 2} & E_{1 \rightarrow 3} & E_{1 \rightarrow 4} \\ E_{1 \rightarrow 2} & E_{2 \rightarrow 2} & E_{2 \rightarrow 3} & E_{2 \rightarrow 4} \end{bmatrix} \cdot \begin{bmatrix} Q_1 \\ Q_2 \end{bmatrix} \quad (1.80)$$

Each volume flux, volume source, and surface flux is a vector including the spatial moments up to the desired spatial expansion. The two equations (1.79) and (1.80) hold for each direction of the angular S_N discretization and for each energy group, upon calculation of the appropriate response matrices.

Having presented the characteristic formulation of the transport problem, we now have all the ingredients to introduce the process of *transport sweep* for the iterative solution. The iteration starts from the external boundaries of a given direction Ω_d . Imposing an initial ψ^- and q the flux inside the region of the first cell is computed with the aid of (1.79). With the updated flux, a new source term inside the regions is computed, and the transmission at the external boundary of the cell is determined using (1.80). The ψ^+ obtained are now imposed as ψ^- for the adjacent cell. This transport sweep proceeds on all the cells of the domain until the external boundary is reached. At this point, an updated ψ^- for a different direction is computed using (1.32), where the definition of β depends on the peculiar condition imposed at the external boundary of interest. Such procedure is repeated for each direction of the S_N quadrature formula. Subsequent iterations are employed until converge is reached. For an imposed up/down scattering and fission term $Q(\Omega)$, this iterative scheme provide the solution of the transport problem inside each group.

1.3.3 Inner and Outer iterations

The solution of neutron transport equation can be seen as an ensemble of one-speed problems inside each energy group.

The discrete ordinates iterative scheme inside each group is described by (1.64) and (1.63), that are here simplified as follows:

$$[\mathbf{\Omega}_d \cdot \nabla + \Sigma(\mathbf{r})] \psi_d^{i+1}(\mathbf{r}) = \sum_{h=0}^{N_h} \Sigma_{s,h}(\mathbf{r}) A_{h,d} \phi_h^i(\mathbf{r}) + Q_d^{\text{ext}}(\mathbf{r}), \quad (1.81a)$$

$$\phi_h^{i+1}(\mathbf{r}) = \sum_{d=1}^{N_d} w_d A_{h,d} \psi_d^{i+1}(\mathbf{r}), \quad (1.81b)$$

where the i is the iteration index, the double indices (ℓ, m) of the spherical harmonics are replaced with the global index h (N_h is the total anisotropy order considered), the subscript d indicates a discrete direction (so that $\psi_d(\mathbf{r}) = \psi(\mathbf{r}, \mathbf{\Omega}_d)$ and $A_{h,d} = A_{\ell,m}(\mathbf{\Omega}_d)$) (N_d is the number of directions considered), and $Q_d^{\text{ext}}(\mathbf{r})$ represents the source term (up/down-scattering and fission). The first equation is valid for each angular direction of the quadrature formula and the second one is used to recalculate the flux angular moment to update the in-scattering contribution. They can be rearranged in matrix form, namely:

$$L\psi^{i+1} = H\psi^i + q, \quad (1.82)$$

where $L = \mathbf{\Omega} \cdot \nabla$ is the transport operator, H is the in-scattering operator, and q is the “external” source (i.e. external of the given group). We note that (1.82) corresponds to (1.48), where the term q includes up/down-scattering, fission, and imposed source.

The peculiar nature of q induces a multiple level of iterations: *inners*, *thermals*, and *outers*:

- an inner iteration corresponds to the solution of the transport problem inside a given group g , imposing an initial source q and an initial set of entering boundary conditions; convergence of the flux inside each energy group is obtained proceeding by source iteration with the transport sweep described in §1.3.2;
- a thermal iteration corresponds to the calculation of the up/down-scattering among different groups;
- an outer iteration corresponds to the computation of the fission term using the updated angular fluxes.

The multigroup transport calculation therefore proceeds as follows. Starting from the higher energy group, the solution of each one-speed transport problem is found with the MSC. As long as only down-scattering occurs, the scattering source is computed and calculated for the subsequent group exactly, resembling the Gauss-Seidel iteration scheme. When also up-scattering is present, an additional iteration is performed: the out-of-group scattering term is recalculated and the solution of the transport problem inside each group is repeated until convergence is reached. When the last energy group is reached, the fission integral (and consequently the eigenvalue k) is recalculated, and procedure restarts.

Convergence criteria for the three level of iterations are:

- inner iterations (i index):

$$\max_{r,h,c} \frac{|\phi_{r,h,c}^{i+1} - \phi_{r,h,c}^i|}{\max_{h,c} |\phi_{r,h,c}^i|} < \epsilon_{\text{inn}}, \quad (1.83)$$

where h is the angular momentum, c is the spatial moment, r is the position;

- thermal iterations (t index):

$$\left| 1 - \frac{\int dV \phi^{t-1}}{\int dV \phi^t} \right| < \epsilon_{\text{th}} \quad (1.84)$$

- outer iterations (e index):

$$\left| 1 - \frac{k^{e-1}}{k^e} \right| < \epsilon_k, \quad (1.85)$$

$$\max_{r,c} \frac{|F_{r,c}^e - F_{r,c}^{e-1}|}{\max_c |F_{r,c}^e|} < \epsilon_F, \quad (1.86)$$

where F is the fission integral, and k the eigenvalue computed as ratio between two successive angular flux estimations.

1.4 Boundary Projection Acceleration

Source iteration process used in the inner iterations (1.82) is a fixed-point iterative strategy emerging from difference relations. In problems with optically thick regions and a ratio of scattering $c = \Sigma_s/\Sigma$ close to 1, the convergence of this iterative process may become unacceptably slow. In fact, the source iteration process may be physically interpreted as follows. Starting with a scalar flux $\phi^0(\mathbf{r}) = 0$, after i iterations $\phi^i(\mathbf{r})$ is the flux of neutrons emitted by the sources that have

collided less than i times. Let's consider a single energy group and a medium with material and geometrical properties so that absorption, escape, or transfer to other groups is negligible compared to in-group scattering. A neutron traveling into this medium would be on average elastically scattered a multitude of times. As a consequence, the source iteration process converges very slowly, and may become practically unusable. Moreover, the difference between successive iterations may be less than the maximum allowed error set as convergence criterion. Thus, false convergence may occur, resulting in nonphysical and erroneous outputs. Acceleration methods are therefore of paramount importance to alleviate the computational burden of the source iteration and to assure convergence.

Many techniques have been developed in the past to accelerate the convergence of source iterations (Adams and Larsen, 2002), for instance coarse mesh rebalance or Chebyshev extrapolation (Lewis and Miller, 1984). Among them *synthetic* methods have gained popularity thanks to their effectiveness. Synthetic methods are based on low-order approximation of the transport equation that is subsequently used to accelerate the convergence. The iterative process is therefore modified so that the acceleration equation is solved between two successive transport iterations, applying a correction that speeds-up the convergence. The most simple approach of this category is the Diffusion Synthetic Acceleration (DSA), where diffusion, that is the more crude approximation of complete transport, is employed as low-order operator. Acceleration schemes based on transport theory are called Transport Synthetic Acceleration (TSA).

In the following we present the implementation of the Boundary Projection Acceleration (BPA) inside IDT for heterogeneous cells. It is a transport synthetic acceleration that is based on a coarser angular representation, applied only at the borders of the spatial mesh. It has been originally developed by Adams and Martin (1988) as technique with the following properties: stability and rapid convergence, generality with respect to geometry, discretization scheme, and mesh shape. Already ported to IDT for homogeneous cells (Masiello and Rossi, 2013), this method has been extended for a more general HCC.

1.4.1 Synthetic acceleration

The system of equations to be solved may be represented symbolically as:

$$(L - H)\boldsymbol{\psi} = \boldsymbol{q}. \quad (1.87)$$

Since the inversion of the full $(L - H)$ operator as a whole is practically impossible, we may proceed iteratively calculating only the inverse of L , namely:

$$\boldsymbol{\psi}^{(i+1/2)} = L^{-1}H\boldsymbol{\psi}^{(i)} + L^{-1}\boldsymbol{q}, \quad (1.88)$$

where i and $(i + 1/2)$ designate two successive iterative solutions. By calculating the difference between (1.88) and (1.87) we may write the equation for the error:

$$L(\boldsymbol{\psi} - \boldsymbol{\psi}^{(i+1/2)}) = H(\boldsymbol{\psi} - \boldsymbol{\psi}^{(i)}), \quad (1.89)$$

where $\boldsymbol{\psi}$ is the converged solution. By adding and subtracting $\boldsymbol{\psi}^{(i+1/2)}$ at the right hand side, we can express the solution as:

$$\boldsymbol{\psi} = \boldsymbol{\psi}^{(i+1/2)} + (L - H)^{-1} H(\boldsymbol{\psi}^{(i+1/2)} - \boldsymbol{\psi}^{(i)}). \quad (1.90)$$

It is evident that we can obtain the solution of the problem from the the error between two successive iteration and the inversion of the full $(L - H)$ operator.

The synthetic acceleration is based on the reformulation of the transport problem in a simpler way, such that the resulting $(\widetilde{L} - H)$ operator is simpler to invert. In this way (1.90) is transformed to:

$$\boldsymbol{\psi}^{(i+1)} = \boldsymbol{\psi}^{(i+1/2)} + (\widetilde{L} - H)^{-1} H(\boldsymbol{\psi}^{(i+1/2)} - \boldsymbol{\psi}^{(i)}), \quad (1.91)$$

where the theoretical solution $\boldsymbol{\psi}$ is replaced by the accelerated solution $\boldsymbol{\psi}^{(i+1)}$. The latter can be rearranged as:

$$(\widetilde{L} - H)\boldsymbol{\varepsilon} = H\delta\boldsymbol{\psi} \quad (1.92)$$

where

$$\boldsymbol{\varepsilon} = \boldsymbol{\psi}^{(i+1)} - \boldsymbol{\psi}^{(i+1/2)}, \quad (1.93)$$

is the unknown of the acceleration problem (the correction to be computed), and

$$\delta\boldsymbol{\psi} = \boldsymbol{\psi}^{(i+1/2)} - \boldsymbol{\psi}^{(i)}, \quad (1.94)$$

is the transport residual of the normal iterations, that acts as source term. The solution of (1.92) can be found by source iteration as well, namely:

$$(\widetilde{L})\boldsymbol{\varepsilon}^{(j+1)} = H\boldsymbol{\varepsilon}^{(j)} + \delta\boldsymbol{\psi}, \quad (1.95)$$

where j is the iteration index for the acceleration problem.

The solution of the transport equation follows these steps:

1. starting from an initial value $\boldsymbol{\psi}^{(i)}$ a transport iteration is performed to obtained a new unaccelerated estimate of the angular flux $\boldsymbol{\psi}^{(i+1/2)}$;

2. using the two last know values of the angular flux the source term for the acceleration problem is computed using (1.94), and a numerical solution for ε is sought iteratively using (1.95);
3. the angular flux is corrected with the error computed with the acceleration, i.e.

$$\boldsymbol{\psi}^{(i+1)} = \boldsymbol{\psi}^{(i)} + \varepsilon \quad (1.96)$$

This procedure is repeated until the converge criterion is reached. With this formulation the synthetic acceleration acts as a *preconditioner* for the full transport problem.

To be efficient, a synthetic acceleration scheme should be simpler (in terms of mathematical complexity), lighter (in terms of memory requirements), and faster (in term of CPU power required) than the original transport problem, while accurate enough to speed-up effectively the iterative solution. Also, it should be stable enough not to ruin the convergence of the unaccelerated source iteration. As a matter of fact, DSA schemes may experience instability, while the BPA is proved to be more robust since it works only with the interface conditions among spatial cells (Adams and Martin, 1988).

1.4.2 BPA for the Method of Short Characteristics in HCC

The S_N method is based on the discretization of the neutron transport equation into N_d discrete directions. The iterative scheme of (1.81) can be reformulated using the balance and transmission equations of short characteristic scheme (1.77) and (1.78). Considering a given direction $\boldsymbol{\Omega}_d$ and writing explicitly the in-scattering contribution, we may write:

$$\boldsymbol{\psi}_d^{(i+1/2)} = \mathbf{I}_d \boldsymbol{\psi}_d^{-,(i+1/2)} + \mathbf{C}_d \left[\mathbf{H}_d \boldsymbol{\phi}^{(i)} + \mathbf{q}_d^{\text{ext}} \right] \quad (1.97a)$$

$$\boldsymbol{\psi}_d^{+,(i+1/2)} = \mathbf{T}_d \boldsymbol{\psi}_d^{-,(i+1/2)} + \mathbf{E}_d \left[\mathbf{H}_d \boldsymbol{\phi}^{(i)} + \mathbf{q}_d^{\text{ext}} \right] \quad (1.97b)$$

$$\boldsymbol{\phi}_h^{(i+1/2)} = \mathbf{D}_h \boldsymbol{\psi}^{(i+1/2)} \quad (1.97c)$$

where $\boldsymbol{\psi}_d$, $\boldsymbol{\psi}_d^\pm$, and $\mathbf{q}_d^{\text{ext}}$ contain the spatial moments of the angular flux inside the cell, of the angular flux at the edges of the cell, and of the external source (up/down-scattering and fission, coming from thermal and outer iterations). The matrix \mathbf{H}_d enables the computation of the scattering internal at the selected energy group starting from the angular moments of the flux, i.e.:

$$\mathbf{H}_d \boldsymbol{\phi} = \sum_{h=0}^{N_h} \Sigma_{s,h}(\mathbf{r}) \mathbf{A}_{h,d} \boldsymbol{\phi}_h, \quad (1.98)$$

where N_h is the number of spherical harmonics used to reconstruct the source. In turn, the angular moments ϕ_h are computed using the quadrature formula with N_d point that is at the hearth of the S_N methodology, namely:

$$\phi_h = D_h \psi = \sum_{d=1}^{N_d} w_d A_{h,d} \psi_d, \quad (1.99)$$

where D_h is the operator that reconstruct the angular moments starting from the angular discretization of the flux.

The acceleration equation is obtained by projecting the angular flux on the borders of the cell on a reduced set of angular directions. We shall now proceed on the definition of a *projection* and *prolongation* operator, to be able to go back and forth the transport and acceleration unknowns.

The angular discretization of the transport solver is based on an ensemble N_d of nodes and weights:

$$\{\Omega_d, w_d\}_{d=1, N_d}, \quad (1.100)$$

while the acceleration employs a reduced set of N_k directions:

$$\{\Omega_k, w_k\}_{k=1, N_k}. \quad (1.101)$$

Each direction Ω_k comes with an associated angular subdomain $\Delta\Omega_k$, each of them containing several nodes of the original S_N discretization. Therefore, we can define a characteristic function of each k direction:

$$\chi_{k,d} = \chi(\Omega_k, \Omega_d) = \begin{cases} 1 & \Omega_d \in \Delta\Omega_k \\ 0 & \Omega_d \notin \Delta\Omega_k \end{cases}. \quad (1.102)$$

The weights of the reduced angular quadrature formula are subsequently computed as:

$$w_k = \int_{\Delta\Omega_k} d\Omega = \sum_{d=1}^{N_d} w_d \chi_{k,d}. \quad (1.103)$$

Once the low-order angular discretization has been constructed, we can define the projection operator able to be used for the interface fluxes. The fluxes in the coarse angular discretization are calculated as weighted average of the fluxes in the fine angular mesh:

$$\psi_{s,k} = P_{s,k \leftarrow d} \psi_s = \frac{\sum_{d=1}^{N_d} w_d \chi_{k,d} \zeta_{s,d} \psi_{s,d}}{\sum_{d=1}^{N_d} w_d \chi_{k,d} \zeta_{s,d}} \quad (1.104)$$

where s subscript indicates the index of the border surface considered. The definition of the weights $\zeta_{s,d}$ is arbitrary, but induces the conservation of different

quantities. For instance, $\zeta_{s,d} = 1$ results in the conservation of the scalar flux, while $\zeta_{s,d} = |\mathbf{\Omega} \cdot \hat{n}_s|$ leads to the conservation of the partial currents traversing the borders of the cell. If the projection preserves the partial currents, then the acceleration equation preserves the balance of particles inside each cell. We therefore adopted this scheme.

The prolongation operator operator is constructed considering the angular fluxes $\boldsymbol{\psi}_k$ isotropically distributed in each subdomain $\Delta\Omega_k$, i.e.:

$$\boldsymbol{\psi}_d = P_{d \leftarrow k} \boldsymbol{\psi}_k = \sum_{k=1}^{N_k} \chi_{k,d} \boldsymbol{\psi}_k. \quad (1.105)$$

Using the operators defined so far, the errors of the transport source iteration are:

$$\boldsymbol{\varepsilon}_s^{\pm,(i)} = \boldsymbol{\psi}_s^{\pm} - \boldsymbol{\psi}_s^{\pm,(i)}, \quad (1.106a)$$

$$\boldsymbol{\varepsilon}_{s,k}^{\pm,(i)} = P_{s,k \leftarrow d} \boldsymbol{\varepsilon}_s^{\pm,(i)}, \quad (1.106b)$$

$$\boldsymbol{\varepsilon}^{(i)} = \boldsymbol{\psi} - \boldsymbol{\psi}^{(i)}, \quad (1.106c)$$

$$\delta\boldsymbol{\phi}_h^{(i)} = \boldsymbol{\phi}_h - \boldsymbol{\phi}_h^{(i)} = \mathbf{D}_h \boldsymbol{\varepsilon}^{(i)}. \quad (1.106d)$$

We shall proceed on the derivation of the accelerated set of equations. By subtracting to (1.97a) the converged solution, we get the equation for the error inside the cell

$$\boldsymbol{\varepsilon}_d^{(i+1/2)} = \mathbf{I}_d \boldsymbol{\varepsilon}_d^{-(i+1/2)} + \mathbf{C}_d \mathbf{H}_d \delta\boldsymbol{\phi}^{(i)}. \quad (1.107)$$

We proceed by integration over all the directions Ω_d using the \mathbf{D}_h operator

$$\mathbf{D}_h \boldsymbol{\varepsilon}_d^{(i+1/2)} = \mathbf{D}_h \mathbf{I}_d \boldsymbol{\varepsilon}_d^{-(i+1/2)} + \mathbf{D}_h \mathbf{C}_d \mathbf{H}_d \delta\boldsymbol{\phi}^{(i)}, \quad (1.108)$$

and by substitution using the prolongation operator for $\boldsymbol{\varepsilon}_d^{-(i+1/2)}$

$$\mathbf{D}_h \boldsymbol{\varepsilon}_d^{(i+1/2)} = \mathbf{D}_h \mathbf{I}_d P_{d \leftarrow k} \boldsymbol{\varepsilon}_k^{-(i+1/2)} + \mathbf{D}_h \mathbf{C}_d \mathbf{H}_d \delta\boldsymbol{\phi}^{(i)} \quad (1.109)$$

to finally obtain

$$\delta\boldsymbol{\phi}_h^{(i+1/2)} = \hat{\mathbf{I}}_{h,k} \boldsymbol{\varepsilon}_k^{-(i+1/2)} + \hat{\mathbf{C}}_h \left[\mathbf{H}_d \delta\boldsymbol{\phi}^{(i+1/2)} + \mathbf{H}_d (\boldsymbol{\phi}^{(i+1/2)} - \boldsymbol{\phi}^{(i)}) \right], \quad (1.110)$$

where

$$\hat{\mathbf{I}}_{h,k} = \mathbf{D}_h \mathbf{I}_d P_{d \leftarrow k} = \sum_{d=1}^{N_d} w_d A_{h,d} \mathbf{I}_d \chi_{k,d}, \quad (1.111)$$

and

$$\hat{\mathbf{C}}_h = \mathbf{D}_h \mathbf{C}_d = \sum_{d=1}^{N_d} w_d A_{h,d} \mathbf{C}_d. \quad (1.112)$$

By subtracting to (1.97b) the converged solution, we get the equation for the error at the surfaces of the cell

$$\boldsymbol{\varepsilon}_d^{+, (i+1/2)} = \mathbf{T}_d \boldsymbol{\varepsilon}_d^{-, (i+1/2)} + \mathbf{E}_d \mathbf{H}_d \delta \boldsymbol{\phi}^{(i)}. \quad (1.113)$$

Then, we project the values at the boundary of the cell into the coarser angular discretization

$$P_{k \leftarrow d} \boldsymbol{\varepsilon}_d^{+, (i+1/2)} = P_{k \leftarrow d} \mathbf{T}_d \boldsymbol{\varepsilon}_d^{-, (i+1/2)} + P_{k \leftarrow d} \mathbf{E}_d \mathbf{H}_d \delta \boldsymbol{\phi}^{(i)} \quad (1.114)$$

and by substitution using the prolongation operator for $\boldsymbol{\varepsilon}_d^{-, (i+1/2)}$

$$P_{k \leftarrow d} \boldsymbol{\varepsilon}_d^{+, (i+1/2)} = P_{k \leftarrow d} \mathbf{T}_d P_{d \leftarrow k} \boldsymbol{\varepsilon}_k^{-, (i+1/2)} + P_{k \leftarrow d} \mathbf{E}_d \mathbf{H}_d \delta \boldsymbol{\phi}^{(i)} \quad (1.115)$$

to finally obtain

$$\boldsymbol{\varepsilon}_k^{+, (i+1/2)} = \hat{\mathbf{T}}_k \boldsymbol{\varepsilon}_k^{-, (i+1/2)} + \hat{\mathbf{E}}_k \left[\mathbf{H}_d \delta \boldsymbol{\phi}^{(i+1/2)} + \mathbf{H}_d (\boldsymbol{\phi}^{(i+1/2)} - \boldsymbol{\phi}^{(i)}) \right], \quad (1.116)$$

where

$$\hat{\mathbf{T}}_k = P_{k \leftarrow d} \mathbf{T}_d P_{d \leftarrow k} = \frac{\sum_{d=1}^{N_d} w_d |\boldsymbol{\Omega} \cdot \hat{\mathbf{n}}| \chi_{k,d} \mathbf{T}_d \chi_{k,d}}{\sum_{d=1}^{N_d} w_d |\boldsymbol{\Omega} \cdot \hat{\mathbf{n}}| \chi_{k,d}}, \quad (1.117)$$

and

$$\hat{\mathbf{E}}_k = P_{k \leftarrow d} \mathbf{E}_d = \frac{\sum_{d=1}^{N_d} w_d |\boldsymbol{\Omega} \cdot \hat{\mathbf{n}}| \chi_{k,d} \mathbf{E}_d}{\sum_{d=1}^{N_d} w_d |\boldsymbol{\Omega} \cdot \hat{\mathbf{n}}| \chi_{k,d}}. \quad (1.118)$$

The accelerated equations are so far valid for each anisotropy order and each coarse angular discretization. In order to reduce the computational burden of the acceleration scheme we decided to accelerate only the isotropic spherical harmonics order $h = 0$ considering a reduced quadrature set S_2 , that includes 1 direction per octant (i.e. $N_k = 4$ in 2D and $N_k = 8$ in 3D).

In this way the \mathbf{H} operator reduces to a matrix $\boldsymbol{\Sigma}_{s,0}$ containing only the scattering cross sections of each internal region. In the case of Figure 1.4, it is equal to³:

$$\boldsymbol{\Sigma}_{s,0} = \begin{bmatrix} \Sigma_{s,0,1} & 0 \\ 0 & \Sigma_{s,0,2} \end{bmatrix}. \quad (1.119)$$

To simplify the notation, from now on we drop the subscript $h = 0$.

³subscripts are: collision type (i.e. scattering), moment order h , region r

We start introducing some definitions:

$$\Delta\boldsymbol{\phi} = \boldsymbol{\phi}^{(i+1/2)} - \boldsymbol{\phi}^{(i)}, \quad (1.120)$$

$$\hat{D} = (\mathbf{1} - \hat{C}\boldsymbol{\Sigma}_s)^{-1}, \quad (1.121)$$

$$\hat{D}^* = (\mathbf{1} - \boldsymbol{\Sigma}_s\hat{C})^{-1}, \quad (1.122)$$

where $\mathbf{1}$ is the identity matrix, and $\hat{D} = \hat{D}^*$ in the case of homogeneous cells with only one region.

The accelerated balance (1.110) becomes:

$$\delta\boldsymbol{\phi}^{(i+1/2)} = \hat{I}_k\boldsymbol{\varepsilon}_k^{-(i+1/2)} + \hat{C}\boldsymbol{\Sigma}_s\delta\boldsymbol{\phi}^{(i+1/2)} + \hat{C}\boldsymbol{\Sigma}_s\Delta\boldsymbol{\phi}, \quad (1.123)$$

and after the inversion of $\mathbf{1} - \hat{C}\boldsymbol{\Sigma}_s$

$$\delta\boldsymbol{\phi}^{(i+1/2)} = \hat{D} \left(\hat{C}\boldsymbol{\Sigma}_s\Delta\boldsymbol{\phi} + \delta\boldsymbol{\phi}^{-(i+1/2)} \right), \quad (1.124)$$

where

$$\delta\boldsymbol{\phi}^{-(i+1/2)} = \hat{I}_k\boldsymbol{\varepsilon}_k^{-(i+1/2)}. \quad (1.125)$$

At the same time, the accelerated transmission (1.116) becomes:

$$\boldsymbol{\varepsilon}_k^{+(i+1/2)} = \hat{T}_k\boldsymbol{\varepsilon}_k^{-(i+1/2)} + \hat{E}_k\boldsymbol{\Sigma}_s\delta\boldsymbol{\phi}^{(i+1/2)} + \hat{E}_k\boldsymbol{\Sigma}_s\Delta\boldsymbol{\phi}, \quad (1.126)$$

and, substituting (1.124),

$$\boldsymbol{\varepsilon}_k^{+(i+1/2)} = \hat{T}_k\boldsymbol{\varepsilon}_k^{-(i+1/2)} + \hat{E}_k\boldsymbol{\Sigma}_s\hat{D}\hat{C}\boldsymbol{\Sigma}_s\Delta\boldsymbol{\phi} + \hat{E}_k\boldsymbol{\Sigma}_s\Delta\boldsymbol{\phi} + \hat{E}_k\boldsymbol{\Sigma}_s\hat{D}\delta\boldsymbol{\phi}^{-(i+1/2)}. \quad (1.127)$$

The matrix \hat{D} obeys the following relation:

$$\hat{D} = \hat{D}(\hat{C}\boldsymbol{\Sigma}_s + \mathbf{1} - \hat{C}\boldsymbol{\Sigma}_s) = \hat{D}(\hat{C}\boldsymbol{\Sigma}_s + \hat{D}^{-1}) = \hat{D}\hat{C}\boldsymbol{\Sigma}_s + \mathbf{1}, \quad (1.128)$$

and similarly for \hat{D}^* holds:

$$\hat{D}^* = \hat{D}^*(\boldsymbol{\Sigma}_s\hat{C} + \mathbf{1} - \boldsymbol{\Sigma}_s\hat{C}) = \hat{D}^*(\boldsymbol{\Sigma}_s\hat{C} + \hat{D}^{*-1}) = \hat{D}^*\boldsymbol{\Sigma}_s\hat{C} + \mathbf{1}. \quad (1.129)$$

These two matrices are related by the following identity

$$\boldsymbol{\Sigma}_s\hat{D} = \hat{D}^*\boldsymbol{\Sigma}_s, \quad (1.130)$$

in fact

$$\boldsymbol{\Sigma}_s = \hat{D}^*\boldsymbol{\Sigma}_s\hat{D}^{-1} = \hat{D}^*\boldsymbol{\Sigma}_s(\mathbf{1} - \hat{C}\boldsymbol{\Sigma}_s) = (\mathbf{1} - \boldsymbol{\Sigma}_s\hat{C})(\mathbf{1} - \boldsymbol{\Sigma}_s\hat{C})\boldsymbol{\Sigma}_s = \boldsymbol{\Sigma}_s. \quad (1.131)$$

Making use of (1.130) and (1.129), (1.127) becomes:

$$\varepsilon_k^{+, (i+1/2)} = \hat{T}_k \varepsilon_k^{-, (i+1/2)} + \hat{E}_k \hat{D}^* (\Sigma_s \Delta \phi + \Sigma_s \delta \phi^{-, (i+1/2)}). \quad (1.132)$$

The acceleration problem is defined by the integrated balance (1.124) and the projected transmission (1.132). As a result, the solution of the transport problem follows these steps:

- transport iteration using (1.97) to get the spatial moments $\psi^{(i+1/2)}$ and $\psi^{+, (i+1/2)}$ for each angular direction Ω_d , as explained in §1.3.2;
- calculation of source of the acceleration problem as a difference between the previous accelerated iteration and the current unaccelerated iteration using (1.120);
- transport sweep with (1.132) to find $\varepsilon_k^{+, (i+1/2)}$;
- calculation of the correction to be applied to the flux isotropic angular moment using (1.124) using the updated $\varepsilon_k^{-, (i+1/2)}$;
- update of the fluxes inside the cell:

$$\phi^{(i+1)} = \phi^{(i+1/2)} + \delta \phi^{(i+1/2)}, \quad (1.133a)$$

$$\psi_d^{+, (i+1)} = \psi_d^{+, (i+1/2)} + P_{d \leftarrow k} \varepsilon_k^{+, (i+1/2)}. \quad (1.133b)$$

1.4.3 Boundary source correction

So far, the acceleration corrects only the values inside each spatial mesh, while the boundary conditions at the edges of the computational domain are kept unaccelerated. Basically the transport sweep after the application of the BPA starts with $\psi_{s,d}^{+, (i+1/2)}$. The BPA methodology can be therefore extended to take into account also the correction for the boundary conditions, resulting in a more robust numerical algorithm.

The general albedo boundary condition (1.32) is here rewritten in its iterative form:

$$\psi_{s,d}^{-, (i+1/2)} = \beta \psi_{s,d}^{+, (i)}, \quad (1.134)$$

and its associated relation at convergence:

$$\psi_{s,d}^- = \beta \psi_{s,d}^+. \quad (1.135)$$

The error between the two is:

$$\varepsilon_{s,d}^{-, (i+1/2)} = \beta \varepsilon_{s,d}^{+, (i)} = \beta \varepsilon_{s,d}^{+, (i+1/2)} + \beta \delta \psi_{s,d}^+, \quad (1.136)$$

where

$$\delta\psi_{s,d}^+ = \psi_{s,d}^{+,(i+1/2)} - \psi_{s,d}^{+,(i)}. \quad (1.137)$$

After the application of the projection operator, we can calculate the accelerated correction at the boundaries of the computational domain. At the end of each iteration of the acceleration process, the incoming boundary condition is updated as well using this formula:

$$\epsilon_{s,k}^{-(i+1/2)} = P_{s,k \leftarrow d} \epsilon_{s,d}^{-(i+1/2)} = \beta \epsilon_{s,k}^{+, (i+1/2)} + P_{s,k \leftarrow d} \beta \delta\psi_{s,d}^+. \quad (1.138)$$

The boundary angular fluxes to be used for the successive transport calculation are then computed with:

$$\begin{aligned} \psi_s^{-(i+1)} &= \psi_s^{-(i+1/2)} + \sum_{k=1}^{N_k} \chi_{k,d} \epsilon_{s,k}^{-(i+1/2)} = \\ & \psi_s^{-(i+1/2)} + \sum_{k=1}^{N_k} \left[\chi_{k,d} (\beta \epsilon_{s,k}^{+, (i+1/2)} + P_{s,k \leftarrow d} \beta \delta\psi_{s,d}^+) \right]. \end{aligned} \quad (1.139)$$

1.4.4 Numerical implementation

Storage strategy and vectorization

This acceleration strategy has been programmed in Fortran 90 inside the multi-group code IDT of the APOLLO platform (Sanchez, Zmijarevic, et al., 2010). Starting from the pure transport inner iteration, the code has been extended including the BPA algorithm described so far. The main goal of our implementation is to provide a fast, efficient, and accurate code, while minimizing the memory requirements.

To fulfill this goal, we carefully decided the storage strategy, in order to avoid wasting memory by storing only the elements different from zero, and to preserve as much as possible the contiguity in memory of the data to be accessed during the loops.

The latter is particularly important to avoid the occurrence of cache misses. In fact, multidimensional arrays got stored into memory as continuous string of bytes. Fortran utilize the column-major order approach, where the first index corresponds to elements continuous in memory, and the last is the one that varies less rapidly when one sequentially scans all the elements of the array. Modern processors present a cache memory, that is physically in the same silicon chip as the arithmetical logical unit. This local memory works as a buffer of the central memory (RAM). While there are multiple levels of this cache, the basic principle is the same. When the code requires an element of an array, the operating system

loads into the cache memory a portion of that array. Subsequently the required value is copied into the processor registers, and the mathematical operations is computed. Once done, the result is stored back to another portion of the cache, and then to the main memory. When an operation is performed on multiple elements of the same array, like in usual loops typical of scientific codes, the processor may take advantage of the presence of the required value in the local cache. If it is not there, it should be fetched from the central memory. Since the RAM is physically farther and intrinsically slower, the processor should wait until the required values get copied into its registers, wasting CPU cycles and user time. It is therefore evident that the storage of the coefficients should be carefully designed so that the subsequent loops required to perform the transport sweep profit of contiguity in memory of the required values. A substantial loss in performance is experienced if the loops and the associated arrays are not carefully designed.

Besides the storage strategy, we designed the code to aid the vectorization of the computation. Starting from the late '90s, the presence of vector registers (e.g. SSE, Streaming Single instruction multiple data Extension) has become more and more popular also for general purpose mainstream processors based on the x86 technology. Previously, such feature was present only on dedicated workstations or on supercomputers. With vector registers, the processor is able to perform the same mathematical operation in parallel for a multitude of values at the same time. The application of the BPA matrices requires the multiplication of the spatial moments on the region volume or on the border surface for the corresponding response matrix elements. Clearly, this operation is easily vectorized if the compiler is instructed to do so. Fortran, contrary to C, includes the possibility to express matrix and vector operations directly without writing a dedicated loop on the single components. Furthermore, Fortran compilers inherit more than 50 years of continuous enhancement and optimization in the field of scientific programming. By carefully expressing the matrix and vector operations, while preserving the continuity in memory, the compiler is able to optimize these operations exploiting the vector registers. This results in an increased speed of the computation.

Regarding the amount of memory required, the method of short characteristics requires to store the four response matrices I , C , T , E for each couple material-geometry⁴, for each direction and group. For a typical 17×17 assembly multi-group depletion calculation the storage required in 2D geometry can easily reach several hundreds of MiB (Masiello, Sanchez, et al., 2009). Since the BPA only degrades the angular representation, the additional memory needed should be

⁴multiple cells with the same geometry and material composition can be pointed to the same arrays stored in memory

carefully taken into account, storing only the coefficients different from zero. In doing this, we can profit from the regularity of the Cartesian cells supported by IDT.

Regarding the transmission matrix, we note given the geometrical shape of a cell, we can determine in advance the entering and exiting surface for each octant. The same consideration can be done for the escape and incoming matrices. Also, since in the acceleration C and I are employed after integration on all the angular directions, we decided to store only the integrated values, further reducing the memory required, and in turn avoiding the necessity to reintegrate over the angular space at each iteration.

If the rings of the heterogeneous Cartesian cell are concentric, the associated collision matrix C is made of diagonal blocks (Masiello, 2013). The peculiar nature of the diagonal blocks of \hat{C} is reflected also on \hat{D} and \hat{D}^* . Therefore, for the inversion required to compute the values of \hat{D} and \hat{D}^* a new dedicate routine has been written based on the Gauss-Jordan elimination with full pivoting (Press et al., 1992). In fact, the \hat{C} may be seen as a square matrix having vector elements, where each component correspond to the diagonal just mentioned. The Gauss-Jordan elimination can be subsequently vectorized to take into account this peculiar structure. The criterion employed for the pivoting is the infinite norm.

Flowcharts of the implementation

The implementation of the BPA algorithm inside IDT can be divided into two parts: *preprocessing* and *iterative solution*.

The flowchart of the former is reported in Figure 1.5. Appropriate routines have been written to extract the values of response matrices from the ones of the transport solver. The elements are then integrated (\hat{C} , \hat{I}) and projected (\hat{E} , \hat{T}) assuming a coarse quadrature formula S_2 . The storage required is dynamically allocated depending on the space required and appropriate pointers to the allocated structures are put in place to ease sharing of the data. Regarding the boundary conditions, we implemented the following possibilities:

- vacuum;
- rotation of $\pi/2$;
- translation;
- specular reflection;
- axial symmetry.

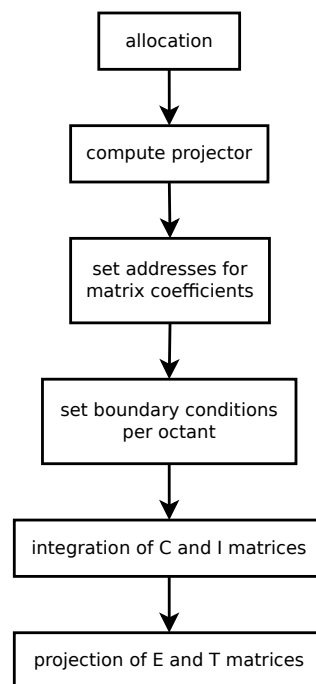


Figure 1.5 Flowchart of the BPA preprocessing.

A schematic representation of the iterative procedure of the BPA is reported in Figure 1.6. After a normal transport iteration, the source for the BPA problem is computed and then the iterative solution starts.

The sweeping chain on the cells of the domain is based on the alternating direction method in the 2D or 3D geometry. Also, the octant ordering is chosen so that the iteration starts from the directions coming from outside the physical domain. For example, if we want to represent a small reactor we may employ symmetry relations to diminish the computational domain. Thus, the boundary conditions at the internal side would be of specular reflection, and at the external side of vacuum. Since the transport iteration starts imposing incoming fluxes equal to zero, it is convenient to start the transport sweep from the direction for which the initial boundary condition is already known.

The incoming angular flux is reevaluated at each iteration. In this way the approach to the solution resemble the Gauss-Seidel method (Quarteroni et al., 2007). Gauss-Jacobi strategy, i.e. the calculation of $\delta\phi^-$ once per each acceleration iteration, has been tested as well. The BPA loop results less expensive in terms of computational time, but the efficiency is sensibly reduced with respect to the Gauss-Seidel methodology.

The accelerated boundary conditions at the surfaces of each cell are subsequently computed with the aid of the \hat{T} and \hat{E} operators. The BPA loops exits

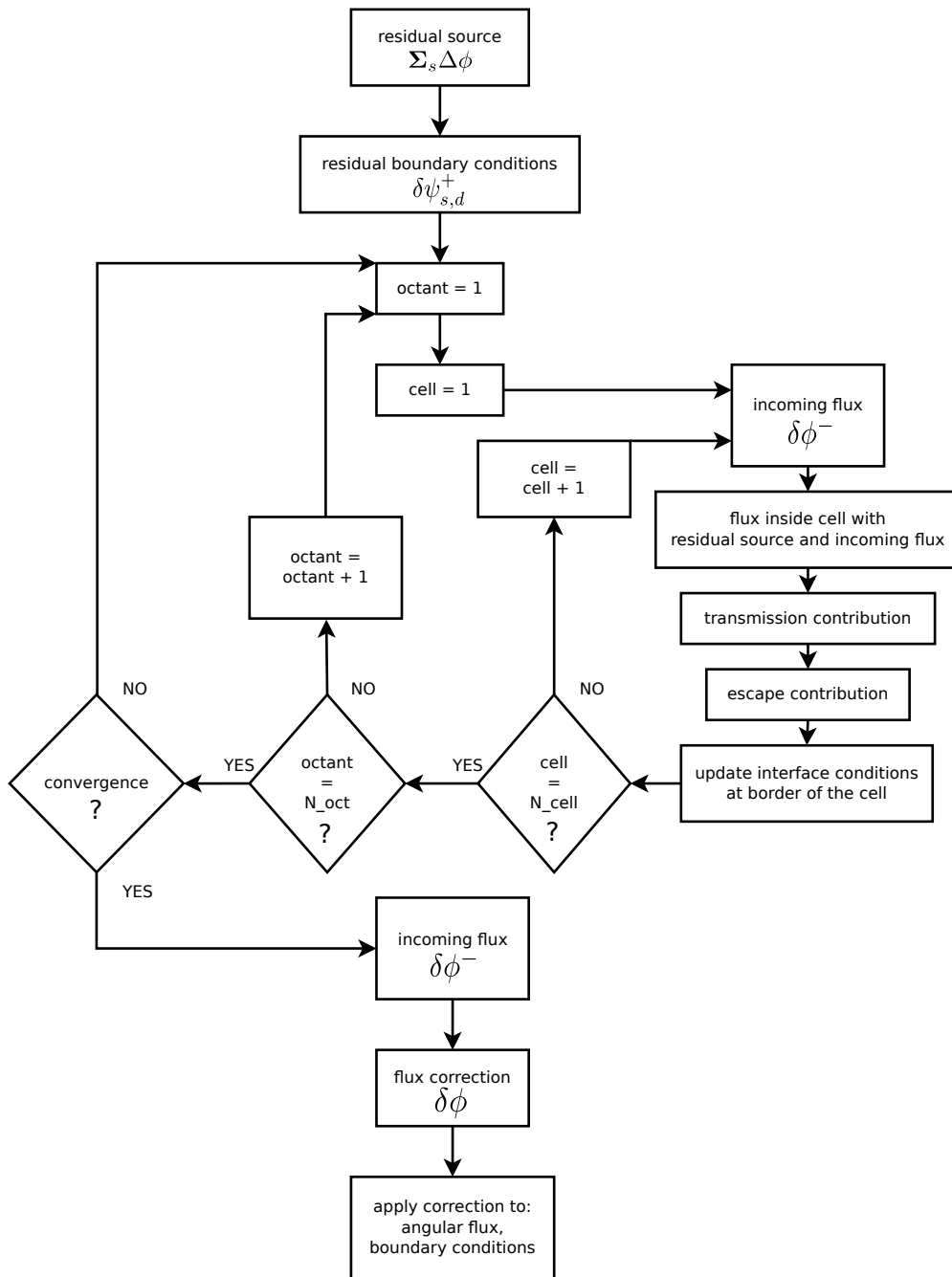


Figure 1.6 Flowchart of the iterative BPA algorithm.

when the convergence criterion is reached or after a maximum number of iterations. Besides, the flux corrections is computed and is applied to the original unaccelerated fluxes of the plain transport iteration.

In selecting the convergence criterion for the BPA, we have to strike a balance between the additional computational burden of the acceleration process and the

effective reduction of transport iterations, i.e. the acceleration should be effective in reducing the spectral radius of the unaccelerated source iteration without consuming too much CPU time. Except that for testing purposes, the maximum number of BPA iterations should be tuned not to pass too much of the computational effort of the transport solver to the acceleration problem.

Moreover, the acceleration of the boundary conditions strengthens the BPA effectiveness. This is particularly evident for small computational domains, where the effect of the boundary conditions inside the spatial mesh is more important. For bigger domains, this enhancement appears to be less relevant.

Finally, we note that by using a S_2 quadrature formula also for the transport iterations, the acceleration problem is equivalent to the full transport. In such cases, the solution of the transport equation is found with only 1 inner iteration, since the BPA problem provides a complete inversion of the $(L - H)$ operator.

1.5 Numerical results

By default IDT accelerates the outer iterations with the Chebyshev method and the thermal iteration with a group rebalance (Zmijarevic, 1998). Recently, it has been included the possibility to accelerate the outer and inner iterations with the CMFD (Coarse Mesh Finite Difference) methodology (Masiello, Sanchez, et al., 2009). In this case the coarse mesh, in which the acceleration operator is solved, is the standard rectangular mesh that is constructed by homogenizing the HCC. With CMFD, that is a non-linear scheme contrary to BPA, the solution is constructed by finite differences based on the diffusion equation, thus further reducing the degree of freedoms.

We shall now present the performance in terms of reduction of inner iterations and CPU time, including comparison with the other acceleration schemes for the standard C5G7 benchmark proposed by IAEA (Lewis, Smith, et al., 2003), for both 2D and 3D geometries. This case problem has been carefully designed to verify the ability of the deterministic 2D and 3D transport codes to solve typical reactor problems without spatial homogenization. It is therefore a good candidate to test the method of short characteristics with heterogeneous cells.

This benchmark considers a reactor core composed by 16 assemblies with two planes of symmetry. It is therefore possible to study the problem in reduced geometry: 1/4 in 2D, 1/8 in 3D. The four assemblies to be studied are surrounded by a water reflector. Figure 1.7 reports the geometry, the material composition, and the solver discretization used. The boundary conditions are of specular reflection and of vacuum at the internal and external boundaries, respectively. The layout in 2D geometry measures 64.26×64.26 cm, while each assembly is 21.42×21.42 cm

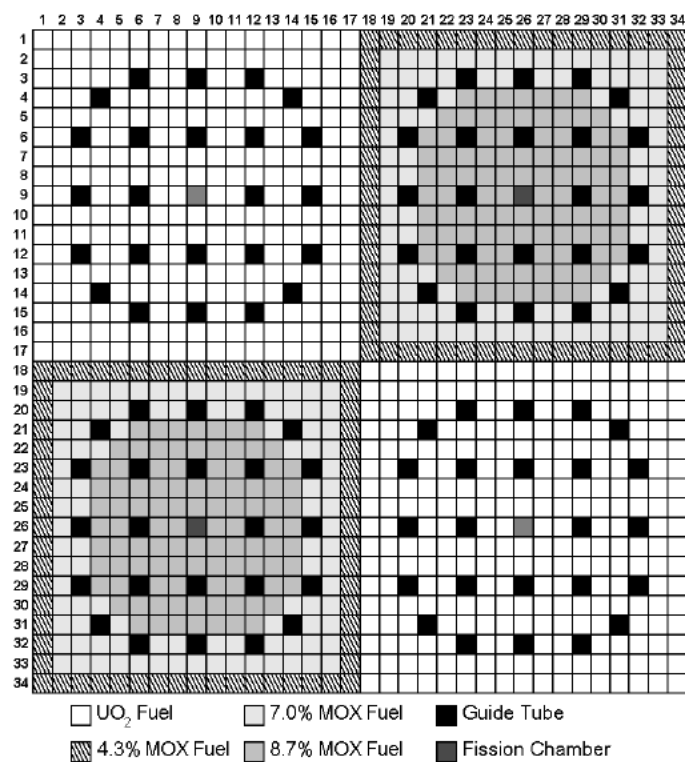
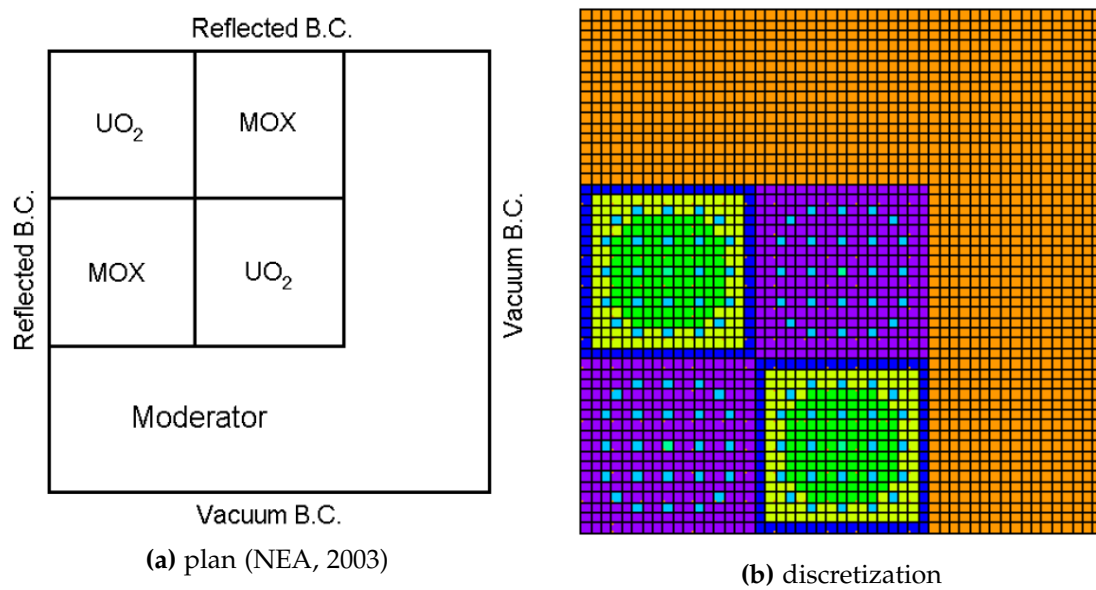


Figure 1.7 C5G7 benchmark: geometry, material composition, and solver discretization.

(NEA, 2003). For the 3D configuration, the fuel assemblies are extended in the vertical direction of 42.84 cm with an additional 21.42 cm water reflector above them (NEA, 2005). The boundary conditions in the 3D geometry are specular reflection at the lower boundary, and vacuum at the upper boundary. The overall dimensions of the core to be studied are therefore $64.26 \times 64.26 \times 64.26$ cm, while each assembly is $21.42 \times 21.42 \times 42.84$ cm.

Each fuel assembly is made up of a 17×17 lattice of square fuel pin cells. The side length of every pin cell is 1.26 cm and every fuel cylinder is of radius 0.54 cm. The composition of the fuel included varies enrichments of MOX and UO_2 , as indicated in Figure 1.7.

The material properties are described with a library of seven-group, transport-corrected, isotropic-scattering cross-sections. These cross sections have been previously pre-calculated using a 69-group solution in an infinite-lattice fine-mesh collision probability calculation with DRAGON (Cathalau et al., 1996; Lewis, Smith, et al., 2003). The reference values for the eigenvalue k has been computed using MCNP (Monte Carlo method).

Regarding the 3D geometry, three possible configurations are provided: Unrodded, Rodded A, and Rodded B (NEA, 2005). In the Unrodded configuration control rod clusters (one cluster for each assembly) are inserted into the upper axial water reflector. We note that, given the symmetry of this benchmark case, the control rods appear to be inserted from both the top and bottom of the proposed reactor, resulting in an unrealistic configuration. In the Rodded A configuration a control rod cluster is inserted 1/3 of the way into the inner UO_2 assembly. Similarly, the Rodded B configuration presents control rod clusters inserted 2/3 of the way into the inner UO_2 assembly and 1/3 of the way into both MOX assemblies.

In the solution of this benchmark problem each fuel pin cell has been represented as an HCC with one circular region inside. For 3D calculations, the boundary surfaces of the mesh cells have been subdivided into two segments, to increase the accuracy of the calculation.

All the computational times quotes refers on the following machine:

- Intel® Core™ i5 CPU 650 @3.20 GHz
- 4096 MiB RAM @1333 MHz
- Linux 3.2.0 64-bit
- Intel® Fortran 14.0.1
- -O1 optimization level

1.5.1 C5G7: 2D configuration

We start studying the 2D configuration of the C5G7 benchmark.

At first we have analyzed the effect of the acceleration methods on the accuracy of the eigenvalue estimation. Indicating with N_c and N_b the number of volume and surface moments, we have considered the following spatial expansions:

- constant, $N_c = 1, N_b = 1$;
- linear, $N_c = 3, N_b = 2$;
- bilinear, $N_c = 4, N_b = 2$.

The regions of the mesh discretization are 3757 and the external surfaces are 204. The number of flux moments needed to reconstruct the power distribution inside the domain are 26 299, 78 897, and 105 196 for constant, linear, and bilinear expansions, respectively.

The calculation has been repeated varying the quadrature scheme and the S_N order. In particular, we employed the product quadrature Chebyshev-Legendre and the default Level-Symmetric quadrature. Also, we have considered the simpler S_2 case for which the acceleration problem corresponds to the full transport. An additional peculiar Level-Symmetric quadrature of order 8 (S_8^*) with the angular directions more displaced near the x and y axis has been tested. This type of quadrature formula allows to better account for the transmission of neutrons along moderator channels that separate the cells.

The computation has been performed with the following acceleration schemes:

- (unacc) Outers: Chebyshev, Thermals: group rebalance, Inners: Unaccelerated;
- (bpa) Outers: Chebyshev, Thermals: group rebalance, Inners: BPA;
- (cmfd) Outers: Chebyshev, Thermals: group rebalance, Inners: CMFD;
- (cmfd+unacc) Outers: CMFD, Inners: Unaccelerated;
- (cmfd+bpa) Outers: CMFD, Inners: BPA;
- (cmfd+cmfd) Outers: CMFD, Inners: CMFD.

The results of the computations just mentioned are given in Table 1.1, that reports the eigenvalue and its relative difference with respect to the reference value 1.18655. First of all we note that, for a given angular discretization and spatial moment expansion, all the acceleration schemes yield to the same result. The stability of the BPA algorithm is therefore confirmed.

Table 1.1 C5G7 2D: eigenvalues and percent difference with respect to reference (1.18655), varying acceleration (outers and inners), MOC spatial moment order (Constant, Linear, Bilinear). Quadrature schemes: Level-Symmetric and Chebyshev-Legendre with $N = 4, 6, 8, 12, 16, S_2$, Level-Symmetric S_8^*

| Acceleration | MOC | S_N | quad | eig | %diff | quad | eig | %diff |
|--------------|-----|-------|------|---------|-------|------|---------|-------|
| unacc | C | 4 | L-S | 1.17980 | 0.569 | C-L | 1.18026 | 0.531 |
| unacc | L | 4 | L-S | 1.18560 | 0.080 | C-L | 1.18567 | 0.075 |
| unacc | B | 4 | L-S | 1.18557 | 0.082 | C-L | 1.18564 | 0.077 |
| bpa | C | 4 | L-S | 1.17980 | 0.569 | C-L | 1.18025 | 0.531 |
| bpa | L | 4 | L-S | 1.18560 | 0.080 | C-L | 1.18566 | 0.075 |
| bpa | B | 4 | L-S | 1.18557 | 0.082 | C-L | 1.18565 | 0.076 |
| cmfd | C | 4 | L-S | 1.17981 | 0.568 | C-L | 1.18026 | 0.531 |
| cmfd | L | 4 | L-S | 1.18560 | 0.080 | C-L | 1.18567 | 0.074 |
| cmfd | B | 4 | L-S | 1.18558 | 0.082 | C-L | 1.18565 | 0.076 |
| cmfd+unacc | C | 4 | L-S | 1.17981 | 0.568 | C-L | 1.18026 | 0.531 |
| cmfd+unacc | L | 4 | L-S | 1.18561 | 0.080 | C-L | 1.18567 | 0.074 |
| cmfd+unacc | B | 4 | L-S | 1.18558 | 0.082 | C-L | 1.18565 | 0.076 |
| cmfd+bpa | C | 4 | L-S | 1.17981 | 0.568 | C-L | 1.18026 | 0.530 |
| cmfd+bpa | L | 4 | L-S | 1.18561 | 0.080 | C-L | 1.18567 | 0.074 |
| cmfd+bpa | B | 4 | L-S | 1.18558 | 0.082 | C-L | 1.18565 | 0.076 |
| cmfd+cmfd | C | 4 | L-S | 1.17981 | 0.568 | C-L | 1.18026 | 0.530 |
| cmfd+cmfd | L | 4 | L-S | 1.18561 | 0.080 | C-L | 1.18567 | 0.074 |
| cmfd+cmfd | B | 4 | L-S | 1.18558 | 0.082 | C-L | 1.18565 | 0.076 |
| unacc | C | 6 | L-S | 1.18061 | 0.501 | C-L | 1.18151 | 0.425 |
| unacc | L | 6 | L-S | 1.18565 | 0.076 | C-L | 1.18600 | 0.046 |
| unacc | B | 6 | L-S | 1.18562 | 0.078 | C-L | 1.18597 | 0.049 |
| bpa | C | 6 | L-S | 1.18061 | 0.501 | C-L | 1.18151 | 0.425 |
| bpa | L | 6 | L-S | 1.18565 | 0.076 | C-L | 1.18600 | 0.046 |
| bpa | B | 6 | L-S | 1.18562 | 0.078 | C-L | 1.18597 | 0.049 |
| cmfd | C | 6 | L-S | 1.18061 | 0.501 | C-L | 1.18151 | 0.425 |
| cmfd | L | 6 | L-S | 1.18566 | 0.075 | C-L | 1.18600 | 0.046 |
| cmfd | B | 6 | L-S | 1.18563 | 0.078 | C-L | 1.18597 | 0.049 |
| cmfd+unacc | C | 6 | L-S | 1.18061 | 0.501 | C-L | 1.18151 | 0.425 |
| cmfd+unacc | L | 6 | L-S | 1.18566 | 0.075 | C-L | 1.18600 | 0.046 |
| cmfd+unacc | B | 6 | L-S | 1.18563 | 0.078 | C-L | 1.18598 | 0.048 |
| cmfd+bpa | C | 6 | L-S | 1.18061 | 0.501 | C-L | 1.18151 | 0.425 |
| cmfd+bpa | L | 6 | L-S | 1.18566 | 0.075 | C-L | 1.18600 | 0.046 |
| cmfd+bpa | B | 6 | L-S | 1.18563 | 0.078 | C-L | 1.18598 | 0.048 |
| cmfd+cmfd | C | 6 | L-S | 1.18061 | 0.500 | C-L | 1.18151 | 0.425 |
| cmfd+cmfd | L | 6 | L-S | 1.18566 | 0.075 | C-L | 1.18600 | 0.046 |
| cmfd+cmfd | B | 6 | L-S | 1.18563 | 0.078 | C-L | 1.18598 | 0.048 |
| unacc | C | 8 | L-S | 1.18092 | 0.474 | C-L | 1.18140 | 0.434 |
| unacc | L | 8 | L-S | 1.18575 | 0.068 | C-L | 1.18611 | 0.037 |
| unacc | B | 8 | L-S | 1.18572 | 0.070 | C-L | 1.18608 | 0.040 |
| bpa | C | 8 | L-S | 1.18092 | 0.474 | C-L | 1.18141 | 0.434 |
| bpa | L | 8 | L-S | 1.18575 | 0.067 | C-L | 1.18611 | 0.037 |
| bpa | B | 8 | L-S | 1.18572 | 0.070 | C-L | 1.18608 | 0.040 |
| cmfd | C | 8 | L-S | 1.18092 | 0.474 | C-L | 1.18141 | 0.434 |

Table 1.1 C5G7 2D: eigenvalues and percent difference with respect to reference (1.18655), varying acceleration (outers and inners), MOC spatial moment order (Constant, Linear, Bilinear). Quadrature schemes: Level-Symmetric and Chebyshev-Legendre with $N = 4, 6, 8, 12, 16$, S_2 , Level-Symmetric S_8^*

| Acceleration | MOC | S_N | quad | eig | %diff | quad | eig | %diff |
|--------------|-----|-------|------|---------|-------|------|---------|-------|
| cmfd | L | 8 | L-S | 1.18575 | 0.067 | C-L | 1.18611 | 0.037 |
| cmfd | B | 8 | L-S | 1.18572 | 0.070 | C-L | 1.18608 | 0.039 |
| cmfd+unacc | C | 8 | L-S | 1.18092 | 0.474 | C-L | 1.18141 | 0.434 |
| cmfd+unacc | L | 8 | L-S | 1.18575 | 0.067 | C-L | 1.18611 | 0.037 |
| cmfd+unacc | B | 8 | L-S | 1.18572 | 0.070 | C-L | 1.18609 | 0.039 |
| cmfd+bpa | C | 8 | L-S | 1.18092 | 0.474 | C-L | 1.18141 | 0.433 |
| cmfd+bpa | L | 8 | L-S | 1.18575 | 0.067 | C-L | 1.18611 | 0.037 |
| cmfd+bpa | B | 8 | L-S | 1.18572 | 0.070 | C-L | 1.18608 | 0.039 |
| cmfd+cmfd | C | 8 | L-S | 1.18092 | 0.474 | C-L | 1.18141 | 0.433 |
| cmfd+cmfd | L | 8 | L-S | 1.18575 | 0.067 | C-L | 1.18611 | 0.037 |
| cmfd+cmfd | B | 8 | L-S | 1.18572 | 0.070 | C-L | 1.18608 | 0.039 |
| <hr/> | | | | | | | | |
| unacc | C | 12 | L-S | 1.18126 | 0.446 | C-L | 1.18159 | 0.418 |
| unacc | L | 12 | L-S | 1.18597 | 0.049 | C-L | 1.18638 | 0.014 |
| unacc | B | 12 | L-S | 1.18593 | 0.052 | C-L | 1.18634 | 0.018 |
| bpa | C | 12 | L-S | 1.18126 | 0.445 | C-L | 1.18159 | 0.418 |
| bpa | L | 12 | L-S | 1.18597 | 0.049 | C-L | 1.18638 | 0.014 |
| bpa | B | 12 | L-S | 1.18594 | 0.052 | C-L | 1.18635 | 0.017 |
| cmfd | C | 12 | L-S | 1.18126 | 0.446 | C-L | 1.18159 | 0.418 |
| cmfd | L | 12 | L-S | 1.18597 | 0.049 | C-L | 1.18638 | 0.014 |
| cmfd | B | 12 | L-S | 1.18594 | 0.052 | C-L | 1.18635 | 0.017 |
| cmfd+unacc | C | 12 | L-S | 1.18126 | 0.446 | C-L | 1.18159 | 0.418 |
| cmfd+unacc | L | 12 | L-S | 1.18597 | 0.049 | C-L | 1.18638 | 0.014 |
| cmfd+unacc | B | 12 | L-S | 1.18594 | 0.051 | C-L | 1.18636 | 0.016 |
| cmfd+bpa | C | 12 | L-S | 1.18127 | 0.445 | C-L | 1.18159 | 0.418 |
| cmfd+bpa | L | 12 | L-S | 1.18597 | 0.049 | C-L | 1.18638 | 0.014 |
| cmfd+bpa | B | 12 | L-S | 1.18594 | 0.051 | C-L | 1.18636 | 0.016 |
| cmfd+cmfd | C | 12 | L-S | 1.18126 | 0.445 | C-L | 1.18159 | 0.418 |
| cmfd+cmfd | L | 12 | L-S | 1.18597 | 0.049 | C-L | 1.18638 | 0.014 |
| cmfd+cmfd | B | 12 | L-S | 1.18594 | 0.051 | C-L | 1.18636 | 0.016 |
| <hr/> | | | | | | | | |
| unacc | C | 16 | L-S | 1.18144 | 0.430 | C-L | 1.18163 | 0.415 |
| unacc | L | 16 | L-S | 1.18613 | 0.035 | C-L | 1.18648 | 0.006 |
| unacc | B | 16 | L-S | 1.18610 | 0.038 | C-L | 1.18645 | 0.008 |
| bpa | C | 16 | L-S | 1.18145 | 0.430 | C-L | 1.18163 | 0.414 |
| bpa | L | 16 | L-S | 1.18613 | 0.035 | C-L | 1.18648 | 0.006 |
| bpa | B | 16 | L-S | 1.18610 | 0.038 | C-L | 1.18645 | 0.009 |
| cmfd | C | 16 | L-S | 1.18145 | 0.430 | C-L | 1.18164 | 0.414 |
| cmfd | L | 16 | L-S | 1.18613 | 0.035 | C-L | 1.18648 | 0.006 |
| cmfd | B | 16 | L-S | 1.18610 | 0.038 | C-L | 1.18645 | 0.008 |
| cmfd+unacc | C | 16 | L-S | 1.18145 | 0.430 | C-L | 1.18164 | 0.414 |
| cmfd+unacc | L | 16 | L-S | 1.18613 | 0.035 | C-L | 1.18649 | 0.005 |
| cmfd+unacc | B | 16 | L-S | 1.18610 | 0.038 | C-L | 1.18646 | 0.008 |
| cmfd+bpa | C | 16 | L-S | 1.18145 | 0.430 | C-L | 1.18163 | 0.414 |
| cmfd+bpa | L | 16 | L-S | 1.18613 | 0.035 | C-L | 1.18649 | 0.005 |

Table 1.1 C5G7 2D: eigenvalues and percent difference with respect to reference (1.18655), varying acceleration (outers and inners), MOC spatial moment order (Constant, Linear, Bilinear). Quadrature schemes: Level-Symmetric and Chebyshev-Legendre with $N = 4, 6, 8, 12, 16$, S_2 , Level-Symmetric S_8^*

| Acceleration | MOC | S_N | quad | eig | %diff | quad | eig | %diff |
|--------------|-----|-------|------|---------|-------|------|---------|-------|
| cmfd+bpa | B | 16 | L-S | 1.18610 | 0.038 | C-L | 1.18646 | 0.008 |
| cmfd+cmfd | C | 16 | L-S | 1.18145 | 0.430 | C-L | 1.18164 | 0.414 |
| cmfd+cmfd | L | 16 | L-S | 1.18613 | 0.035 | C-L | 1.18649 | 0.005 |
| cmfd+cmfd | B | 16 | L-S | 1.18610 | 0.038 | C-L | 1.18646 | 0.008 |
| unacc | C | 2 | - | 1.17951 | 0.594 | | | |
| unacc | L | 2 | - | 1.18601 | 0.045 | | | |
| unacc | B | 2 | - | 1.18590 | 0.055 | | | |
| bpa | C | 2 | - | 1.17950 | 0.594 | | | |
| bpa | L | 2 | - | 1.18601 | 0.045 | | | |
| bpa | B | 2 | - | 1.18590 | 0.055 | | | |
| cmfd | C | 2 | - | 1.17951 | 0.594 | | | |
| cmfd | L | 2 | - | 1.18602 | 0.045 | | | |
| cmfd | B | 2 | - | 1.18589 | 0.056 | | | |
| cmfd+unacc | C | 2 | - | 1.17951 | 0.594 | | | |
| cmfd+unacc | L | 2 | - | 1.18602 | 0.045 | | | |
| cmfd+unacc | B | 2 | - | 1.18589 | 0.056 | | | |
| cmfd+bpa | C | 2 | - | 1.17951 | 0.594 | | | |
| cmfd+bpa | L | 2 | - | 1.18602 | 0.045 | | | |
| cmfd+bpa | B | 2 | - | 1.18589 | 0.055 | | | |
| cmfd+cmfd | C | 2 | - | 1.17951 | 0.594 | | | |
| cmfd+cmfd | L | 2 | - | 1.18602 | 0.045 | | | |
| cmfd+cmfd | B | 2 | - | 1.18589 | 0.056 | | | |
| unacc | C | 8 | L-S* | 1.18223 | 0.365 | | | |
| unacc | L | 8 | L-S* | 1.18644 | 0.009 | | | |
| unacc | B | 8 | L-S* | 1.18640 | 0.013 | | | |
| bpa | C | 8 | L-S* | 1.18223 | 0.364 | | | |
| bpa | L | 8 | L-S* | 1.18644 | 0.009 | | | |
| bpa | B | 8 | L-S* | 1.18641 | 0.012 | | | |
| cmfd | C | 8 | L-S* | 1.18223 | 0.364 | | | |
| cmfd | L | 8 | L-S* | 1.18644 | 0.009 | | | |
| cmfd | B | 8 | L-S* | 1.18641 | 0.012 | | | |
| cmfd+unacc | C | 8 | L-S* | 1.18223 | 0.364 | | | |
| cmfd+unacc | L | 8 | L-S* | 1.18644 | 0.009 | | | |
| cmfd+unacc | B | 8 | L-S* | 1.18641 | 0.012 | | | |
| cmfd+bpa | C | 8 | L-S* | 1.18223 | 0.364 | | | |
| cmfd+bpa | L | 8 | L-S* | 1.18644 | 0.009 | | | |
| cmfd+bpa | B | 8 | L-S* | 1.18641 | 0.012 | | | |
| cmfd+cmfd | C | 8 | L-S* | 1.18223 | 0.364 | | | |
| cmfd+cmfd | L | 8 | L-S* | 1.18644 | 0.009 | | | |
| cmfd+cmfd | B | 8 | L-S* | 1.18641 | 0.012 | | | |

Regarding the precision, an increased accuracy is manifested increasing the angular representation. For this specific benchmark case, the Chebyshev-Legendre scheme appears more accurate than the default Level-Symmetric. Moreover, we note that the Linear and Bilinear spatial expansions provide on average one additional digit of precision to the calculation. Instead, the benefit of the Bilinear scheme as opposed to the Linear seems less evident.

The effectiveness of the BPA algorithm in terms of spectral accuracy (i.e. reduction of inner transport iterations) and total CPU time is presented in Figure 1.8 for Level-Symmetric, in Figure 1.9 for Chebyshev-Legendre, and in Figure 1.10 for S_2 and S_8^* .

First of all, we note that the number of inner iterations to reach convergence is comparable among different quadrature schemes and orders. Besides, the computation time is almost linear with respect to the quadrature order. In fact, the number of Ω_d used to represent the angular flux is directly connected to the number of surface angular moments to be computed. As a consequence, the total number of floating point operations is greatly affected by the angular representation.

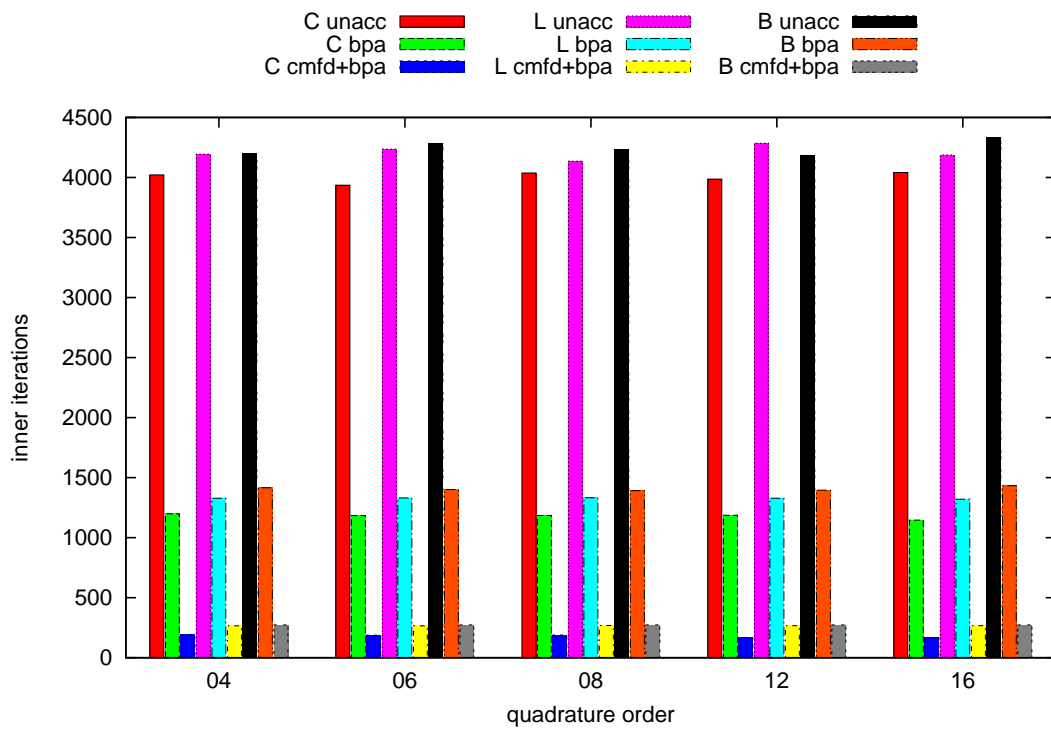
The BPA reduces on average by a factor of 4 the number of internal iterations needed to achieve convergence. When the CMFD scheme is employed for the outer iterations, a further 4-fold reduction in total inner iterations is manifested, resulting to a overall reduction of a factor of 16 of the total iterations.

However, the savings in terms of CPU time is less pronounced. The computational effort required by the BPA looks important, since it reduces only the angular representation, while preserving the other discretization unchanged. In fact, increasing the transport S_N order results in a more effective acceleration.

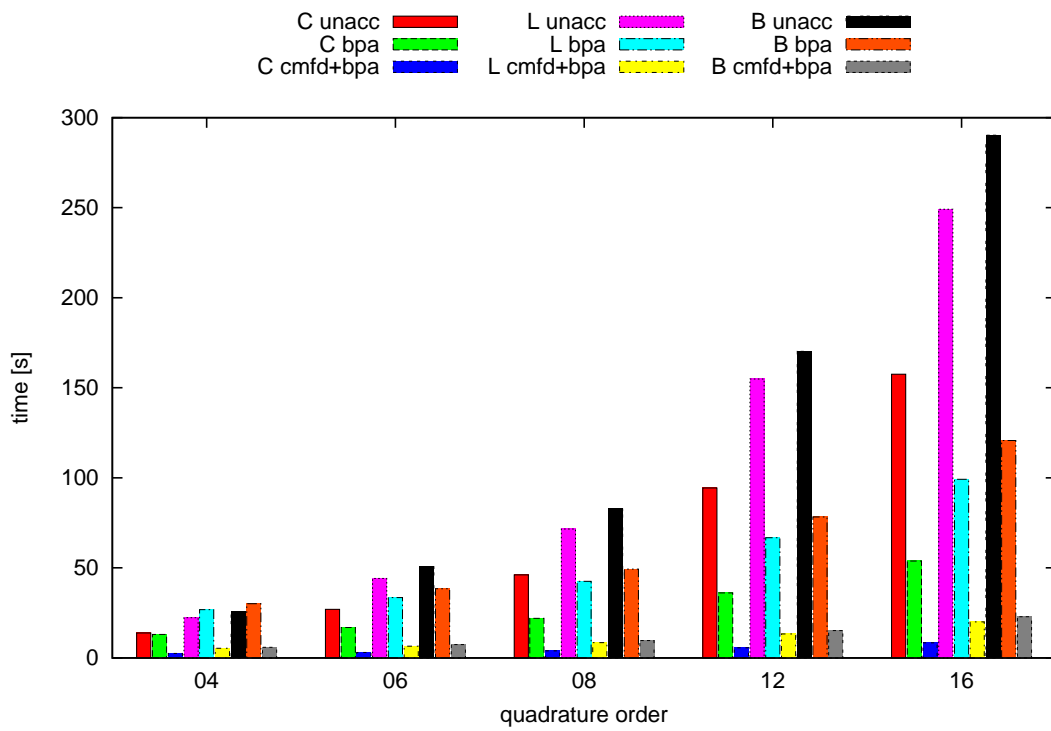
Figure 1.11 and Figure 1.12 are dedicated to the comparison between the BPA and the CMFD, with or without the outer iterations accelerated by CMFD, respectively.

At spectral level, the BPA is more effective, because of the more precise representation of the transport phenomenon that it includes. In terms of total computational time, instead, the BPA is too costly for low quadrature orders, but gains competitiveness for higher angular discretization of the transport solver and higher spatial representations.

While we would like to stress on the fact that the BPA implementation could be further improved, it appears that the CMFD should be preferred for low-order and less precise calculations, while the BPA should be reserved for high-order more accurate computations.

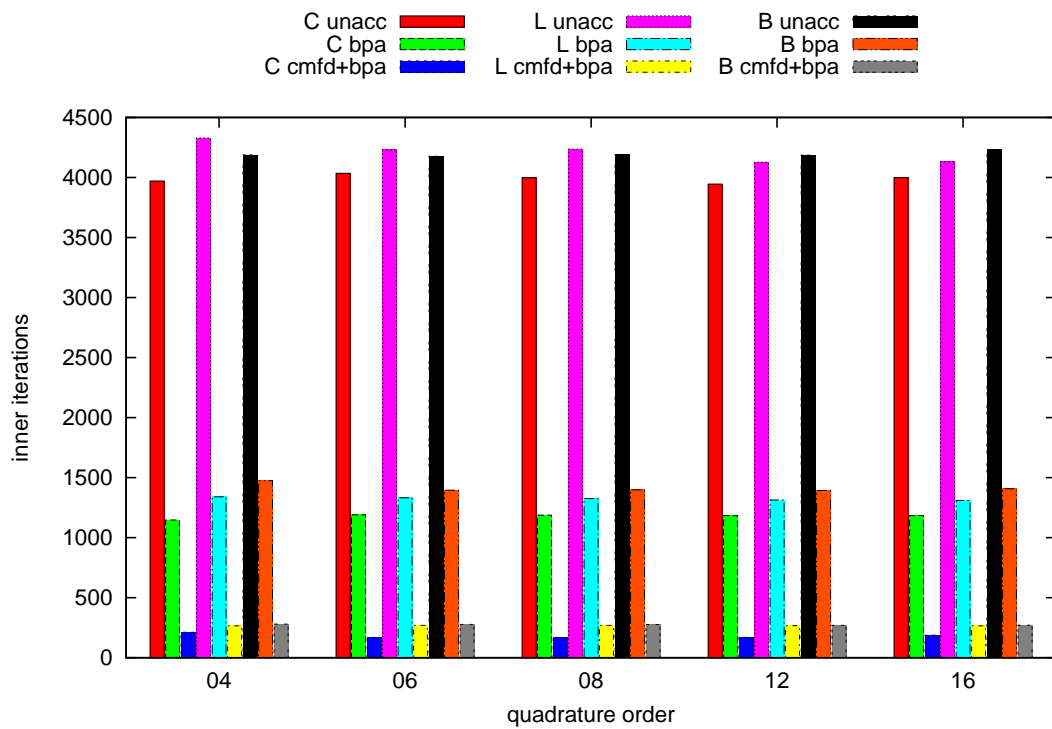


(a) inners

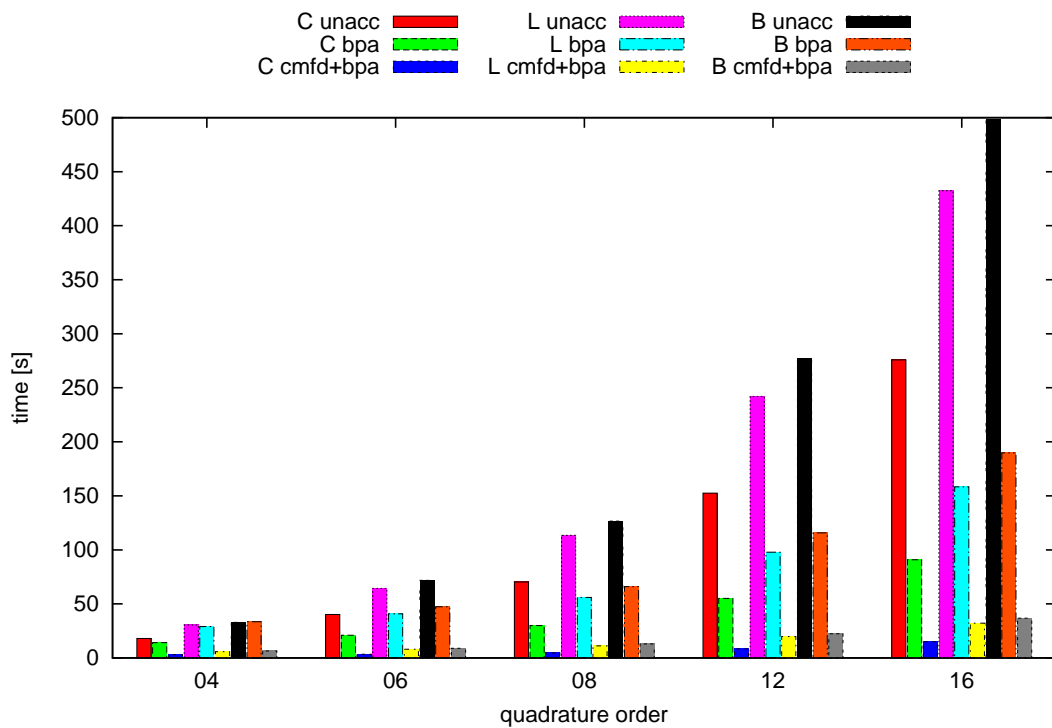


(b) time

Figure 1.8 C5G7 2D benchmark. Quadrature Level Symmetric. Inner iterations and total time varying MOC spatial order (constant, linear, bilinear), SN quadrature order, and acceleration scheme.

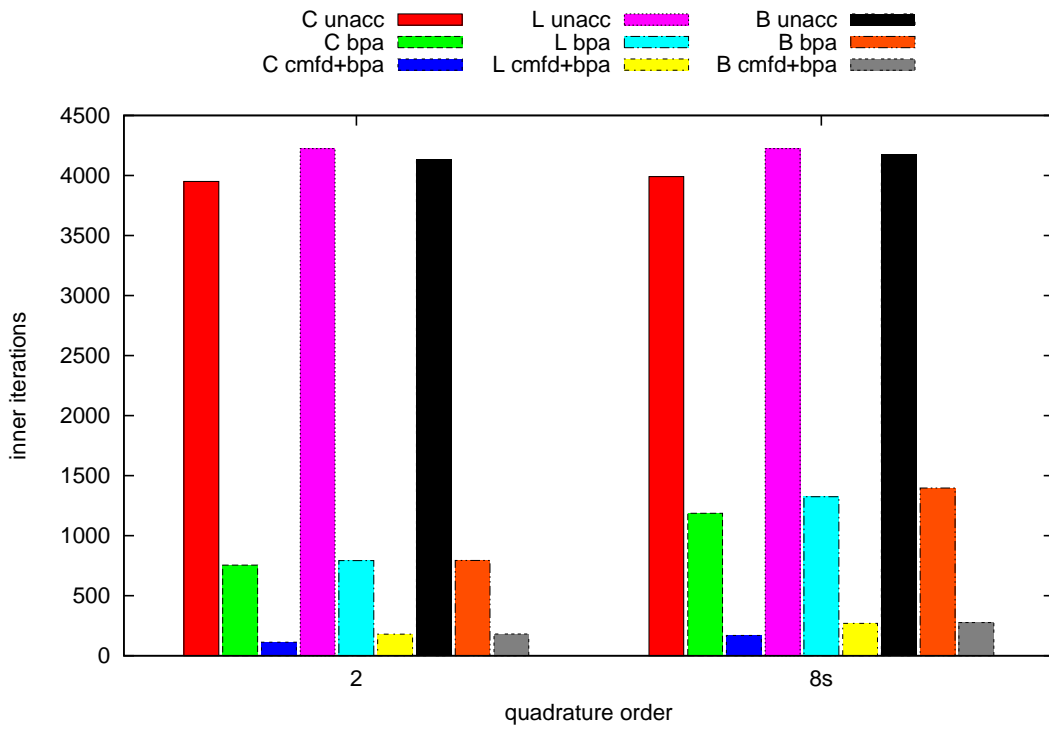


(a) inners

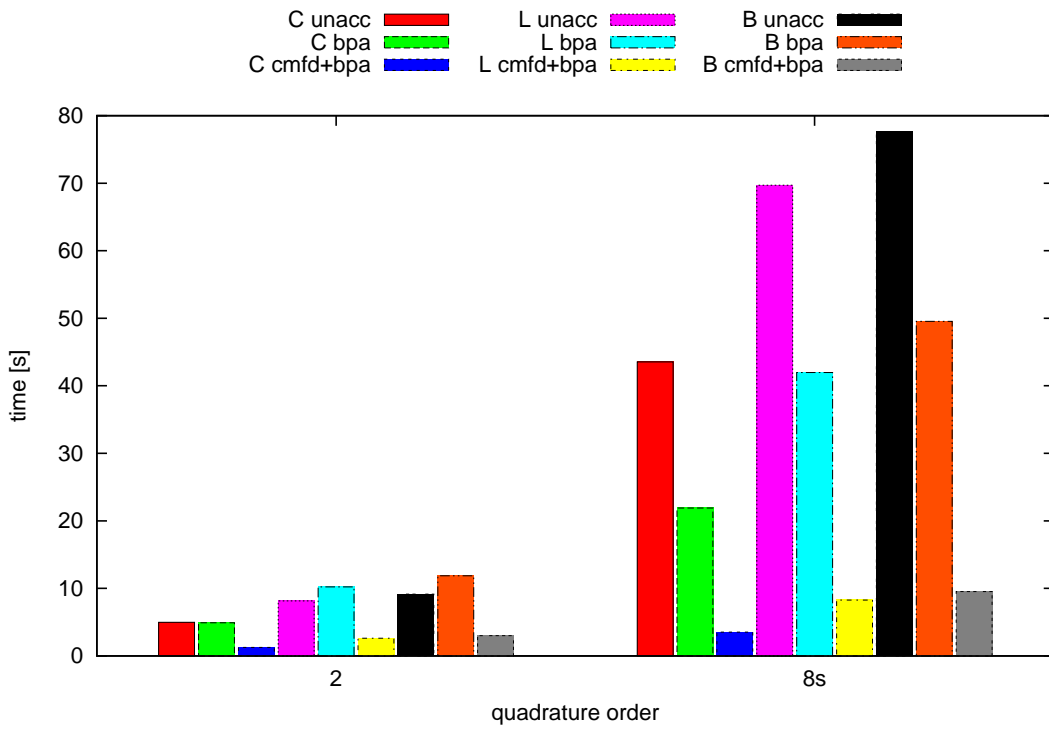


(b) time

Figure 1.9 C5G7 2D benchmark. Quadrature Chebyshev Legendre. Inner iterations and total time varying MOC spatial order (constant, linear, bilinear), SN quadrature order, and acceleration scheme.

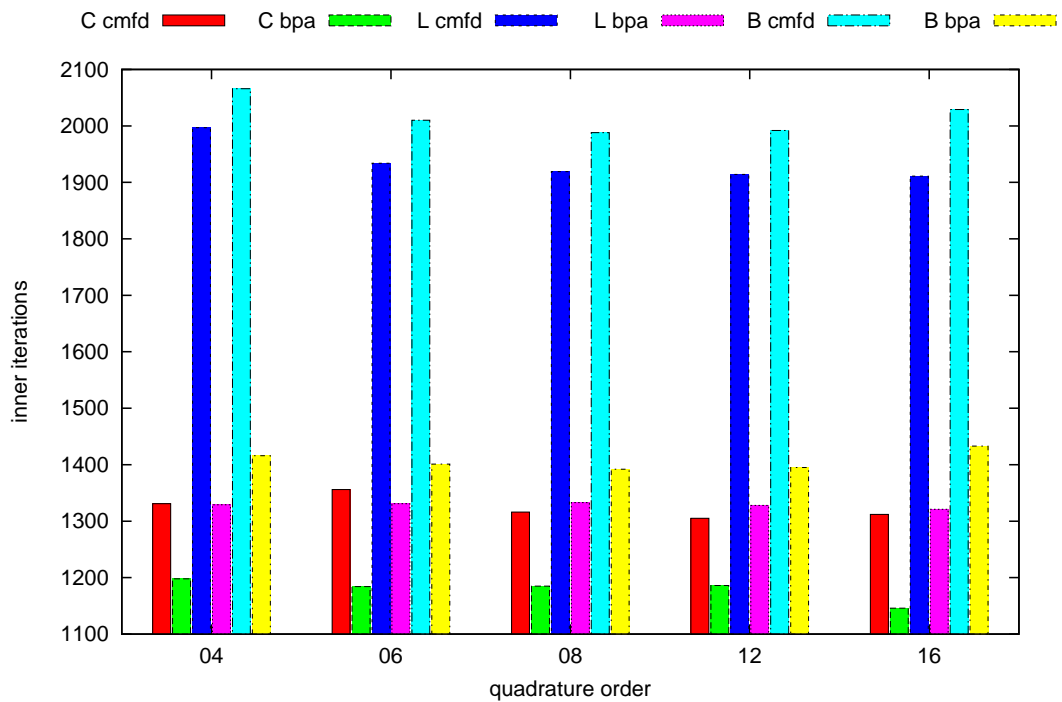


(a) inners

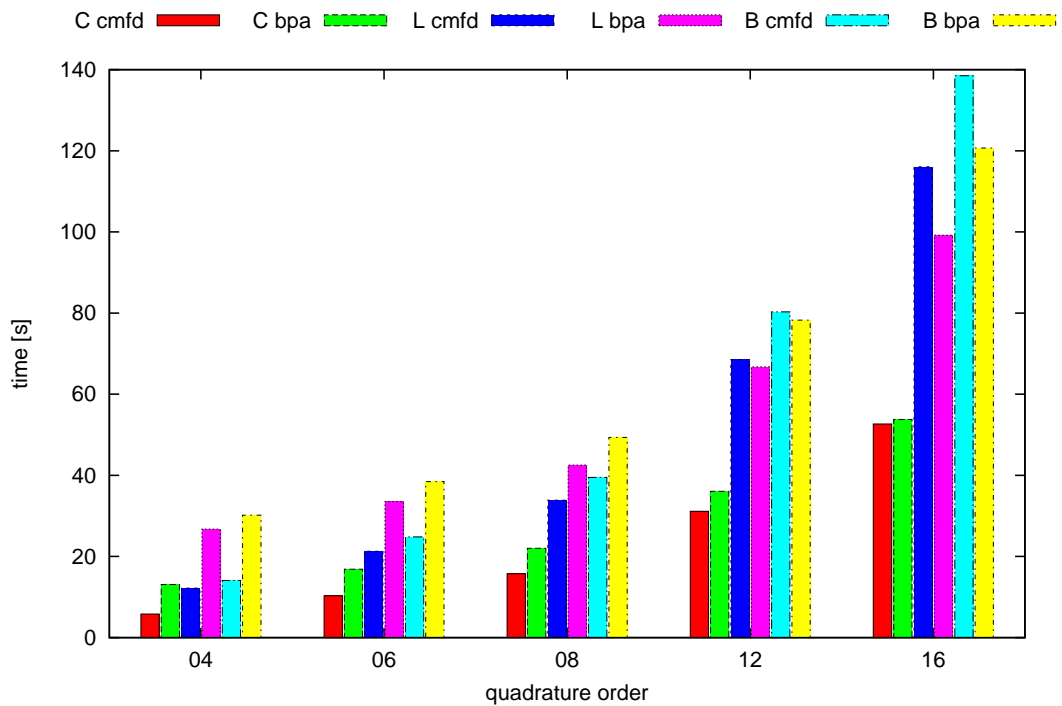


(b) time

Figure 1.10 C5G7 2D benchmark. Quadrature S2 and S8*. Inner iterations and total time varying MOC spatial order (constant, linear, bilinear) and acceleration scheme.

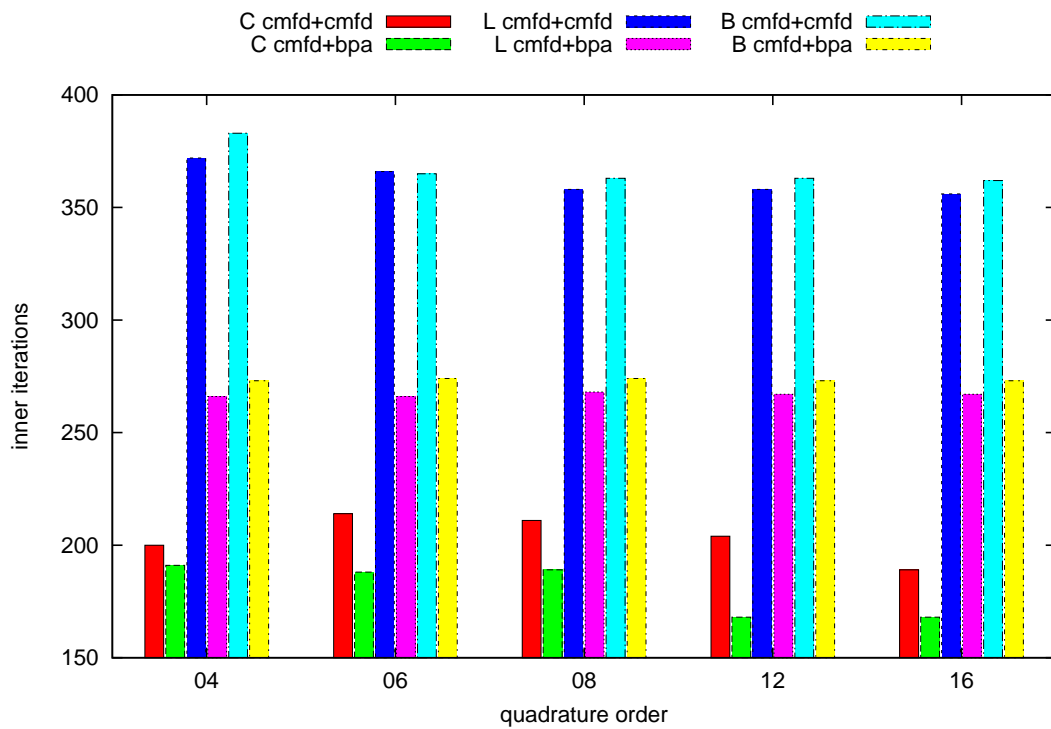


(a) inners

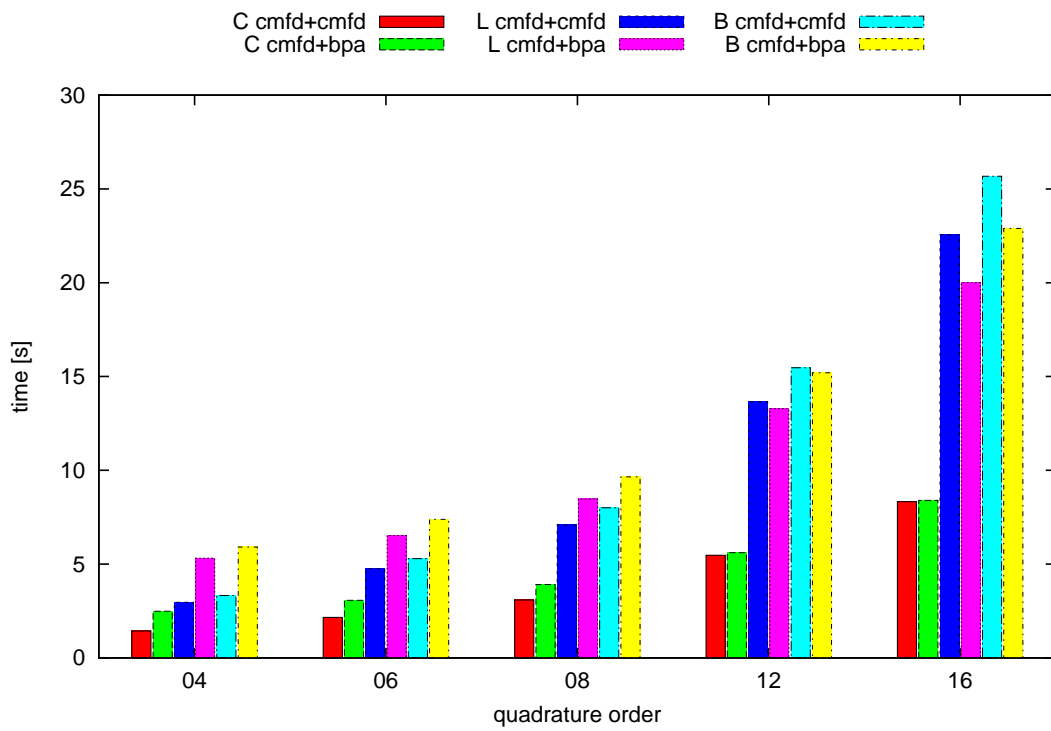


(b) time

Figure 1.11 C5G7 2D benchmark. Quadrature Level Symmetric. Inner iterations and total time varying MOC spatial order (constant, linear, bilinear), and SN quadrature order. Comparison CMFD (Inners) vs BPA (Inners).



(a) inners



(b) time

Figure 1.12 C5G7 2D benchmark. Quadrature Level Symmetric. Inner iterations and total time varying MOC spatial order (constant, linear, bilinear), and SN quadrature order. Comparison CMFD (Outers) + CMFD (Inners) vs CMFD (Outers) + BPA (Inners).

1.5.2 C5G7: 3D Rodded B configuration

For the 3D case, we considered only the Rodded B configuration.

Full 3D heterogeneous transport calculations are today still considered a challenge for their computational cost. In fact, the code needs an higher number of trajectories to compute the response matrices. We decided to limit our analysis to S_8 quadrature formula, that proved to be the more effective for the 2D version of this benchmark. Moreover, we discarded the bilinear characteristic scheme, that did not provide substantial benefits.

In our simulations, the regions of the mesh discretization are 61 290 and the external surfaces are 35 496. Regarding the latter, we opted for subdividing each mesh surface into two sub-surface, to achieve better numerical results. The number of flux moments needed to reconstruct the power distribution inside the domain are 429 030 and 11 716 120 for constant and linear expansions, respectively. The number of unknowns are therefore 2 orders of magnitude more than the 2D case, resulting in much longer simulation times.

The simulation has been repeated with the same acceleration options of the 2D case. The results are given in Table 1.2, that reports the eigenvalue and its difference with respect to the reference value 1.07777. The stability of the BPA algorithm is confirmed also for the 3D case, since the results obtained with the same discretization and different acceleration schemes are comparable.

Regarding the accuracy, the constant characteristic scheme is not sufficient for 3D computations. In fact, the relative error with the reference solution is always above 2%. Subsequently, the eigenvalue estimation does not provide the required precision for reactor core analysis. On the other hands, the linear scheme is able to produce much better results.

The spectral accuracy and the computational efficiency of the BPA with respect to the other acceleration schemes can be inferred from Figure 1.13. The BPA reduces on average by a factor of 6 the number of internal iterations needed to achieve convergence. When the CMFD scheme is employed for the outer iterations, a further 2-fold reduction in total inner iterations is manifested, resulting to a overall reduction of a factor of 12 of the total iterations.

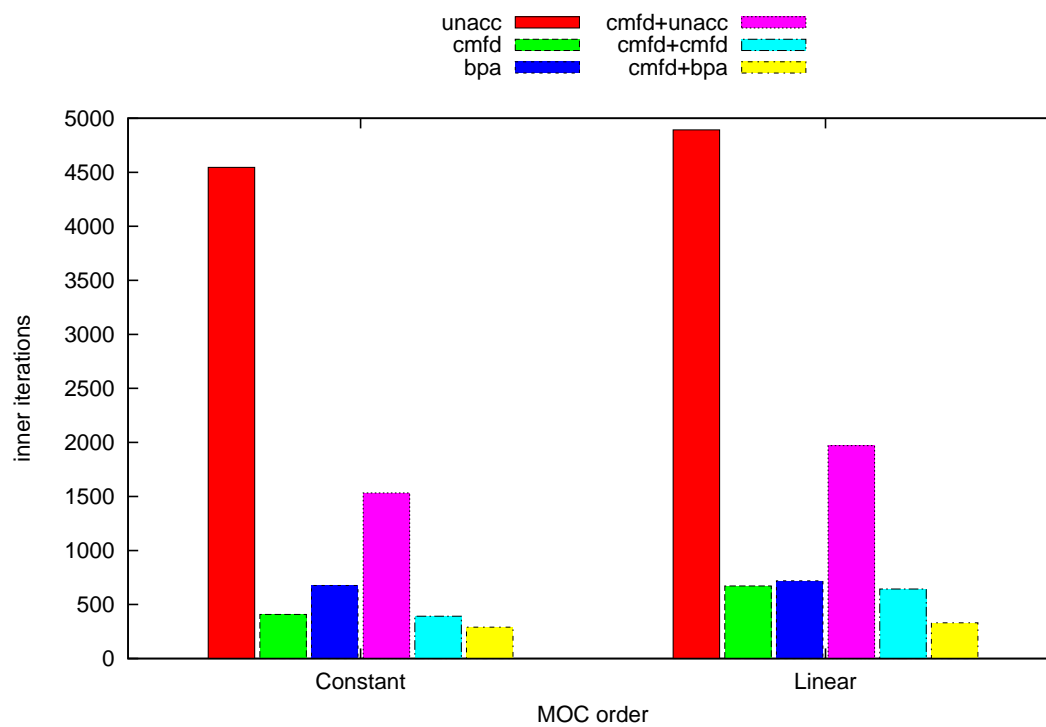
For the default acceleration of the outer and thermal iterations, the BPA is comparable to the CMFD, but it is more costly in term of floating point operations, and therefore the total time is greater. However, when the CMFD is employed for the outer iterations, the BPA provided comparable performances with respect to the CMFD used for inner iterations.

It may be speculated that the BPA would be even more efficient for higher angular representations. However, 3D calculations are intrinsically more demanding in term of CPU time, and therefore the synthetic acceleration should be coupled

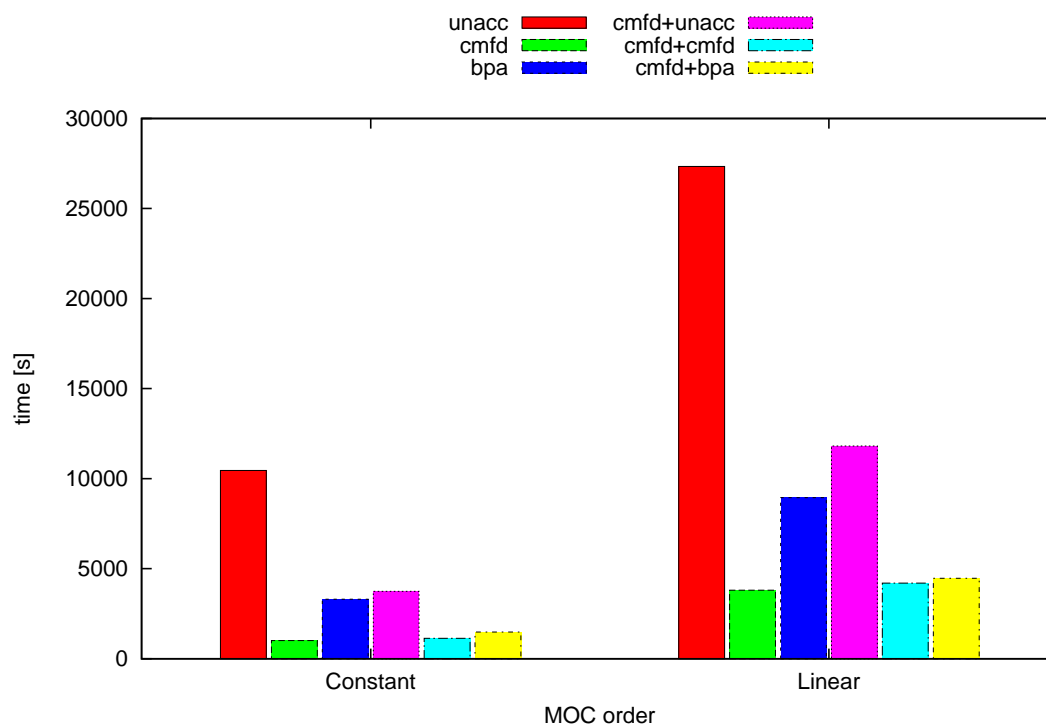
Table 1.2 C5G7 3D: eigenvalues and percent difference with respect to reference (1.07777), varying acceleration (outers and inners), MOC spatial moment order (Constant, Linear). Quadrature scheme: Level-Symmetric S_8^*

| Acceleration | MOC | eig | %diff |
|--------------|-----|---------|-------|
| unacc | C | 1.05258 | 2.338 |
| unacc | L | 1.07738 | 0.036 |
| bpa | C | 1.05259 | 2.336 |
| bpa | L | 1.07739 | 0.035 |
| cmfd | C | 1.05233 | 2.361 |
| cmfd | L | 1.07719 | 0.054 |
| cmfd+unacc | C | 1.05233 | 2.360 |
| cmfd+unacc | L | 1.07717 | 0.056 |
| cmfd+bpa | C | 1.05232 | 2.361 |
| cmfd+bpa | L | 1.07716 | 0.057 |
| cmfd+cmfd | C | 1.05234 | 2.360 |
| cmfd+cmfd | L | 1.07719 | 0.054 |

with other techniques, like parallel computing with domain decomposition.



(a) inners



(b) time

Figure 1.13 C5G7 3D benchmark. Quadrature S8*. Inner iterations and total time varying MOC spatial order (constant, linear) and acceleration scheme.

References

- M. L. Adams and E. W. Larsen (2002). "Fast iterative methods for discrete-ordinates particle transport calculations". In: *Progress in Nuclear Energy* 40.1, pp. 3–159. doi: 10.1016/S0149-1970(01)00023-3.
- M. L. Adams and W. R. Martin (1988). "Boundary Projection Acceleration: A New Approach to Synthetic Acceleration of Transport Calculations". In: *Nuclear Science and Engineering* 100.3, pp. 177–189.
- G. I. Bell and S. Glasstone (1970). *Nuclear Reactor Theory*. Van Nostrand Reinhold.
- B. G. Carlson and G. I. Bell (1958). "Solution of the transport equation by the Sn method". In: *Proceedings of the second international conference on the peaceful uses of atomic energy*. Vol. 16, p. 535.
- S. Cathalau, J. C. Lefebvre, and J. P. West (1996). *Proposal for a Second Stage of the Benchmark on Power Distributions within Assemblies*. OECD/NEA.
- S. Chandrasekhar (1960). *Radiative Transfer*. Dover.
- A. Hébert (2009). *Applied Reactor Physics*. Presses inter Polytechnique.
- K. D. Lathrop (1968). "Ray Effects in Discrete Ordinates Equations". In: *Nuclear Science and Engineering* 32.3, pp. 357–369.
- E. E. Lewis and W. F. Miller (1984). *Computational Methods of Neutron Transport*. Wiley-Interscience.
- E. E. Lewis, M. A. Smith, N. Tsoulfanidis, G. Palmiotti, T. A. Taiwo, and R. N. Blomquist (2003). *Benchmark Specification for Deterministic 2-D/3-D MOX Fuel Assembly Transport Calculations without Spatial Homogenisation*. OECD/NEA.
- E. Masiello (2004). "Résolution de l'équation du transport des neutrons par les méthodes des éléments finis et des caractéristiques structurées appliquées à des maillages hétérogènes". Ph.D. thesis. Université Evry Val d'Essonne.
- E. Masiello (2013). *Personal communication*.
- E. Masiello and T. Rossi (2013). "Improvements of the boundary projection acceleration technique applied to the discrete-ordinates transport solver in XYZ geometries". In: *International Conference on Mathematics and Computational Methods Applied to Nuclear Science & Engineering (M&C 2013)*. Sun Valley, Idaho, USA.
- E. Masiello, R. Sanchez, and I. Zmijarevic (2009). "New Numerical Solution with the Method of Short Characteristics for 2-D Heterogeneous Cartesian Cells in the APOLLO2 Code: Numerical Analysis and Tests". In: *Nuclear Science And Engineering* 161, pp. 257–278.
- NEA (2003). *Benchmark on Deterministic Transport Calculations Without Spatial Homogenisation. A 2-D/3-D MOX Fuel Assembly Benchmark*. NEA/NSC/DOC(2003)16. ISBN: 92-64-02139-6.

- NEA (2005). *Benchmark on Deterministic Transport Calculations Without Spatial Homogenisation. MOX Fuel Assembly 3-D Extension Case*. NEA/NSC/DOC(2005)16. ISBN: 92-64-01069-6.
- W. H. Press, B. P. Flannery, S. A. Teukolsky, and W. T. Vetterling (1992). *Numerical Recipes in Fortran 77: The Art of Scientific Computing*. Cambridge University Press.
- A. Quarteroni, R. Sacco, and F. Saleri (2007). *Numerical Mathematics*. Springer. ISBN: 3-540-34658-9.
- R. Sanchez and N. J. McCormick (1982). "A Review of Neutron Transport Approximations". In: *Nuclear Science and Engineering* 80, pp. 481–535.
- R. Sanchez, I. Zmijarevic, M. Coste-Delclaux, E. Masiello, S. Santandrea, E. Martinolli, L. Villate, N. Schwartz, and N. Guler (2010). "APOLLO2 year 2010". In: *Nuclear Engineering and Technology* 42, pp. 474–499.
- R. Sanchez (2012a). "On SN-PN Equivalence". In: *Transport Theory and Statistical Physics* 41.5-6, pp. 418–447. DOI: 10.1080/00411450.2012.672360.
- R. Sanchez (2012b). "Prospects in Deterministic Three-Dimensional Whole-Core Transport Calculations". In: *Nuclear Engineering and Technology* 44.2, pp. 113–150. DOI: 10.5516/NET.01.2012.501.
- R. Sanchez and J. Ragusa (2011). "On the Construction of Galerkin Angular Quadratures". In: *Nuclear Science and Engineering* 169, pp. 133–154.
- I. Zmijarevic (1998). "Résolution de l'équation de transport par des méthodes nodales et des caractéristiques dans les domaines à deux et trois dimensions". Ph.D. thesis. Université de Provence Aix-Marseille I.

Chapter 2

Thermal effects of neutron scattering off heavy isotopes

The first evidence that neutrons can experience large energy losses in collision with light nuclei was given by Fermi (1934) in a series of fundamental experiments involving neutron diffusion in paraffin wax. For these laboratory experiences Fermi concluded that the elastic cross section for neutrons impinging with protons (i.e. hydrogen nuclei) is much greater than the corresponding absorption cross section, and that after a sufficient number of collisions neutrons speed can be substantially slower (Williams, 1966). Subsequently, Fermi (1936) discussed mathematically the problem of neutron slowing down, diffusion, and thermalization, formulating the infinite medium balance equation, thus deducing the well known $1/E$ neutron energy spectrum.

With the advent of nuclear reactors, and given the predominance of thermal reactor technology, it has become customary to deal with fast and thermal neutron separately. After a fission event, a variable number of neutrons are emitted at high energy in the MeV region. They are consequently slowed down by elastic scattering with the nuclei composing the moderator until they reach a sort of equilibrium with the medium in which they diffuse. Besides scattering events, neutrons can be also absorbed during the slowing down process. As we have seen in Chapter 1, the neutron population inside a reactor core may be described through the linear Boltzmann equation involving appropriate constants (cross sections) describing the events of absorption, scattering, and fission. Accurate modeling of the scattering phenomenon after the birth of a neutron is thus essential for nuclear reactor analysis.

For reactor calculations the energy range of interest to be considered ranges from thermal energies until the top of the fission spectrum, that is around 15 MeV (Henry, 1975). An accurate description of the cross sections in these domain is

therefore required. Absorption involves the formation of a compound nucleus. Instead, scattering reactions can occur due to two contributions: potential scattering, where the collision of the neutron with the nucleus can be represented as an elastic collision between two billiard balls with conservation of momentum and kinetic energy, and real reaction, that comprise the formation of an intermediate compound nucleus before the remission of the neutron. The latter can result both in an elastic or inelastic resonant scattering (Reuss, 2008).

The absorption cross sections present the well known $1/v$ behavior, thus showing an increase probability of absorption for lower energies. The $1/v$ behavior persists up to high energies for most light elements. On the other hand, intermediate and heavy isotopes manifest a complex behavior comprising several peaks above 1 eV. These very sharp variations of the absorption cross sections are called *resonances*. In fact, when the energy of the compound nucleus resulting from a given impinging neutron speed corresponds to one of its excitation levels, the formation of the compound is greatly favored, resulting in large resonance peaks (Henry, 1975). By contrast, the overall behavior of the scattering cross sections is a constant, that corresponds to the potential scattering. However, intermediate and heavy nuclides present resonances as well (Reuss, 2008).

For low kinetic energies of the neutrons and therefore low excitation energies, the levels are clearly separated and the resulting resonances are *resolved*. For higher energies they can no longer be distinguished by measurement: it is the *unresolved* domain. For example, ^{238}U presents three big a absorption resonances at 6.67 eV, 20.9 eV, and 36.7 eV. Generally resonances are more oriented towards either absorption or scattering; however both components always exists (Reuss, 2008).

The resonances are characterized by their peak value and their widths, i.e. the energy range for which the cross section is greater than its peak value. The latter is greatly influenced by the the thermal agitation of the medium in which the neutron diffuse. In fact, the motion of the target nuclei increase the resonance widths as long as the temperature of the medium is increased. In this case the resonance is said to be *Doppler broadened*.

Having presented the general behavior of the interaction cross section we can turn back to the concept of slowing down. The slowing down of the fission neutrons in a thermal reactor in traditionally treated in two parts. As long as the neutron energy is above 1 eV, the thermal agitation of the target nuclei may be neglected, since the neutron energy is much higher than the corresponding average kinetic energy of the medium and its chemical binding energy. In such zone the scattering events can be analyzed by means of the slowing-down, i.e. considering only down-scattering. At energy below 1 eV, i.e. in the thermal region, neutron

energies become comparable with those of the nuclei, and therefore neutron may gain energy as a consequence of a collision. Also, we need to take into account the effects of molecular and/or metallic binding. Since up-scattering can not be neglected, the previous slowing-down approximation cannot be employed anymore (Bell and Glasstone, 1970; Hébert, 2009).

In reactor core analysis, and specifically in the preparation of group cross sections, the differential scattering cross section $\Sigma_s(\mathbf{r}, \boldsymbol{\Omega} \rightarrow \boldsymbol{\Omega}', E \rightarrow E')$ should be calculated taking into account the effect of temperature. The differential scattering cross section is defined by the product of the scattering cross section (1.8) and of the scattering kernel (2.30). The result, expressed in (1.15), has to be convoluted with the energy spectrum of the targets.

Current production codes devoted at this task, like NJOY (MacFarlane and Muir, 2000), assumes the following simplifications:

- at thermal energies $E \approx kT$ both cross section and transfer kernel are convoluted;
- at higher energies $E \gg kT$, and for resonant isotopes, only the cross section is Doppler-broadened;
- otherwise none is convoluted.

Therefore the transfer kernel for energies above the thermal zone is always considered to be equal to the asymptotic one, i.e. considering the target at rest in the laboratory system. This assumption neglects any up-scattering in the resonance domain.

The validity of this approximation for heavy isotopes was firstly questioned by Ouisloumen and Sanchez (1991), who introduced a new deterministic approach to represent the temperature and resonance dependent isotropic scattering kernel into a host medium behaving like a free gas. Their model showed a non-negligible up-scattering for neutrons colliding with heavy isotopes like ^{238}U in the vicinity of resonances slightly above the thermal region. This study was soon corroborated and extended by a series of papers where the fully double-differential kernel was explicitly derived (Rothenstein, 1996; Rothenstein and Dagan, 1998). The resonant kernel has been included as an option into NJOY by Rothenstein (2004), and its results compared with the formulation of Ouisloumen and Sanchez (1991).

The accuracy of using a Maxwellian velocity distribution to describe the motion of target nuclei has been verified by means of MCNP analysis of experimental results at energies in the range of the second ^{238}U resonance, confirming the validity of the gas model (Danon et al., 2009). The physical problem has been assessed also through the theoretical study of the binding forces in a UO_2 crystal lattice,

showing relatively small differences with respect to the analysis based on the free gas scattering kernel (Courcelle and Rowlands, 2007).

The exact scattering kernel has been implemented using the Monte Carlo approach and the generated resonance integral data has been included into CASMO-5 deterministic lattice code by Lee et al. (2008). The impact of ^{238}U resonance elastic scattering for Doppler reactivity has been subsequently assessed for thermal reactors, demonstrating that the asymptotic elastic scattering model traditionally used in the epithermal energy range in NJOY and Monte Carlo codes leads to $\approx 10\%$ under prediction of Doppler coefficients of light water reactor lattices. Reactivity effects from the implementation of a more exact scattering kernel was evaluated of ≈ 200 pcm for PWRs and ≈ 450 pcm for high temperature pebble-bed reactors. This reactivity drop and the associated noticeable changes in the fuel inventory at the end of a fuel cycle has been further evaluated using an enhanced version of TRIPOLI-4 Monte Carlo code (Zoia et al., 2013).

In this chapter, we deal with the numerical computation of the energy and angular dependent scattering kernel, and its Legendre moments. In fact, discrete ordinates codes based on the S_N methodology requires the generation of multi-group transfer matrices, that comprise the Legendre moments of the scattering kernel. After a review of the basic quantities involved in elastic scattering, we concentrate on the theoretical formulation of the Doppler convolution. The range of integration has been evaluated following the approach of Sanchez et al. (2013). The numerical implementation of the calculation of the scattering kernel and its angular moments is then explained, including a convergence analysis of the computation of the Legendre moments and discussing the techniques employed to limit the range of integration while eliminating difference effects. Numerical simulations are subsequently compared with previously published results computed by direct analytical and numerical evaluation and by Monte Carlo (Arbanas et al., 2011).¹

2.1 Mathematical formulation of Doppler convolution

2.1.1 Definitions and dynamics of elastic scattering

Hereafter we should use a *prime* to denote quantities after the scattering event. Also, lowercase and uppercase velocities refer to the neutron and the target, respectively. The ratio between the target mass M and the neutron mass is indicated

¹This work has been realized in cooperation with CEA/DEN/DANS/DM2S/SERMA/LTSD, center of Saclay, France. Part of this chapter has been presented in the the following conference proceeding. A. Previti, R. Sanchez, D. Mostacci, Computation of the Doppler-broadened scattering kernel and its Legendre moments. SNA+MC 2013, Paris, France, October 27-31, 2013.

with A . The Center of Mass system is denoted with the subscript COM and the Laboratory system with LAB. We consider only isotropic media, therefore the elastic scattering and the associated deflection law is assumed to be dependent only upon the deviation angle depicted in Figure 1.3.

The probability of neutron having energy E to be scattered at the energy E' and cosine μ_{LAB} of the deviation angle in laboratory frame is given by the Doppler-broadened transfer kernel $P_T(E \rightarrow E', \mu_{\text{LAB}})$. To compute this quantity, we start defining the velocities before and after the elastic collision in the LAB:

- v, v' designate the neutron;
- V, V' refer to the nucleus.

The corresponding scalar speeds are indicated without the bold font. Introducing the directions Ω and Ω_{COM} of the neutron, the velocities of the neutron in the LAB are in the COM are:

$$\mathbf{v} = v\Omega; \quad \mathbf{v}' = v'\Omega; \quad \mathbf{u} = u\Omega'_{\text{COM}}; \quad \mathbf{u}' = u'\Omega'_{\text{COM}}. \quad (2.1)$$

The deviation angles in the LAB are in the COM are:

$$\mu_{\text{LAB}} = \Omega \cdot \Omega' = \frac{\mathbf{v} \cdot \mathbf{v}'}{vv'}, \quad (2.2a)$$

$$\mu_{\text{COM}} = \Omega_{\text{COM}} \cdot \Omega'_{\text{COM}} = \frac{\mathbf{u} \cdot \mathbf{u}'}{uu'}. \quad (2.2b)$$

From the conservation of linear momentum in the LAB

$$\mathbf{v} + A\mathbf{V} = \mathbf{v}' + A\mathbf{V}', \quad (2.3)$$

it is possible to obtain the velocity of the center of mass

$$\mathbf{c} = \frac{\mathbf{v} + A\mathbf{V}}{A + 1}. \quad (2.4)$$

The relative neutron-target velocity is:

$$\mathbf{v}_r = \mathbf{v} - \mathbf{V}. \quad (2.5)$$

The velocities in the COM are:

$$\mathbf{u} = \mathbf{v} - \mathbf{c} = \beta^{-1}\mathbf{v}_r, \quad (2.6a)$$

$$\mathbf{U} = \mathbf{V} - \mathbf{c} = -\frac{A}{A + 1}\mathbf{v}_r, \quad (2.6b)$$

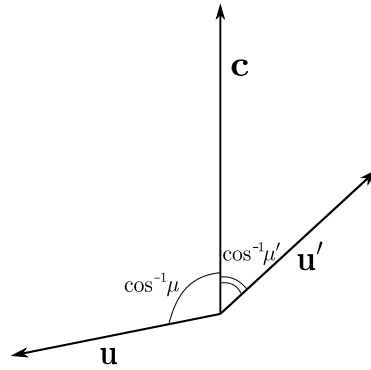


Figure 2.1 Reference system with c as polar axis.

where

$$\beta = \frac{A+1}{A} \quad (2.7)$$

The conservation of linear momentum in the COM

$$\mathbf{u} + A\mathbf{U} = \mathbf{u}' + A\mathbf{U}' \quad (2.8)$$

gives the relations between the velocities of the neutron and of the nucleus in the COM, i.e.:

$$\mathbf{u} = -A\mathbf{U}; \quad \mathbf{u}' = -A\mathbf{U}'. \quad (2.9)$$

The latter result, together with the energy conservation in the COM

$$u^2 + AU^2 = u'^2 + AU'^2, \quad (2.10)$$

is used to determine the velocity after scattering, giving:

$$U = U'; \quad u = u'. \quad (2.11)$$

We now illustrate the relations involving the deviation angles in the LAB and in the COM. Since c is preserved during scattering, we can introduce a system where c plays the role of polar axis, as we can see from Figure 2.1. Squaring (2.6), and considering the latter reference system, we get:

$$v^2 = c^2 + u^2 - 2cu\mu, \quad (2.12a)$$

$$v^2 = c^2 + u'^2 - 2cu'\mu', \quad (2.12b)$$

where

$$\mu = \frac{\mathbf{u} \cdot \mathbf{c}}{uc}; \quad \mu' = \frac{\mathbf{u}' \cdot \mathbf{c}}{uc}. \quad (2.13)$$

Making use of (2.12) we obtain

$$\mu = \frac{v^2 - c^2 - u^2}{2uc} = \frac{1}{m c u} \left[E - \frac{m}{2}(c^2 + u^2) \right], \quad (2.14a)$$

$$\mu' = \frac{v'^2 - c^2 - u^2}{2uc} = \frac{1}{m c u} \left[E' - \frac{m}{2}(c^2 + u^2) \right]. \quad (2.14b)$$

Following (Ouisloumen and Sanchez, 1991), it is possible to express μ_{COM} and μ_{LAB} using μ and μ' . Using the polar axis c , $\mathbf{\Omega}_{\text{COM}}$ and $\mathbf{\Omega}'_{\text{COM}}$ are defined by the usual two angles in polar coordinates, i.e. (μ, ϕ) and (μ', ϕ') . Trigonometric relations give:

$$\mu_{\text{COM}} = \mathbf{\Omega}_{\text{COM}} \cdot \mathbf{\Omega}'_{\text{COM}} = \mu\mu' + \sqrt{(1 - \mu^2)(1 - \mu'^2)} \cos(\phi' - \phi). \quad (2.15)$$

At the same time we have

$$\mu_{\text{LAB}} = \mathbf{\Omega} \cdot \mathbf{\Omega}' = \frac{(\mathbf{u} + \mathbf{c}) \cdot (\mathbf{u}' + \mathbf{c})}{vv'} = \frac{c^2 + cu(\mu + \mu') + u^2\mu_{\text{COM}}}{vv'}. \quad (2.16)$$

By substituting (2.15) and (2.14) into (2.16), the dot product $\mathbf{\Omega} \cdot \mathbf{\Omega}'$ can be expressed in terms of the speeds v, v', c, u, u' and ϕ' (Ouisloumen and Sanchez, 1991; Rothenstein, 2004):

$$\mathbf{\Omega} \cdot \mathbf{\Omega}' = \frac{\mathbf{v} \cdot \mathbf{v}'}{vv'} = \frac{B + C \cos(\phi' - \phi)}{4c^2vv'}, \quad (2.17)$$

where

$$B = [v^2 - (u^2 - c^2)] [v'^2 - (u^2 - c^2)], \quad (2.18a)$$

$$C^2 = [v^2 - (u + c)^2] [v^2 - (u - c)^2] [v'^2 - (u + c)^2] [v'^2 - (u - c)^2]. \quad (2.18b)$$

The dynamics of elastic scattering may be represented by the probability that a neutron with velocity \mathbf{v} would emerge with a velocity \mathbf{v}' about $d\mathbf{v}'$ after a collision with a nucleus having velocity \mathbf{V} , i.e.:

$$P(\mathbf{v}, \mathbf{V} \rightarrow \mathbf{v}') d\mathbf{v}'. \quad (2.19)$$

A change of variable from \mathbf{v}' to the center of mass velocity \mathbf{u}' is required to impose the condition $u = u'$. The velocity c is fully determined by the couple (\mathbf{v}, \mathbf{V}) , and therefore $d\mathbf{v}' = d\mathbf{u}'$. Expressing the direction $\mathbf{\Omega}'_{\text{COM}}$ in spherical coordinates, we may write:

$$d\mathbf{u}' = u^2 du' d\mu' d\phi'. \quad (2.20)$$

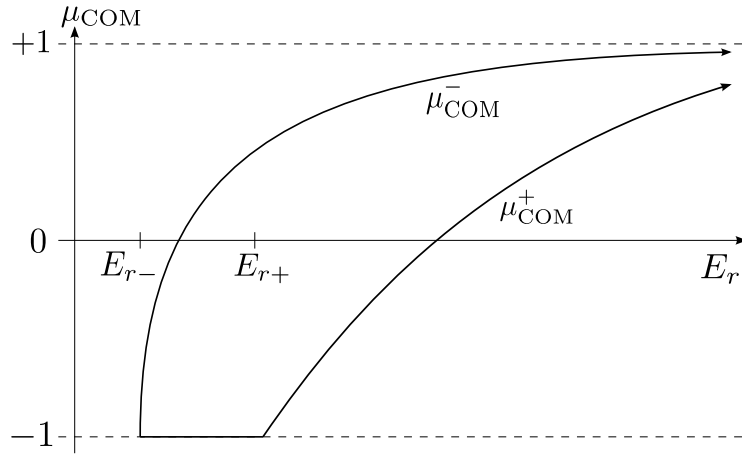


Figure 2.2 Bounds for μ_{COM} versus E_r .

Since $u = u'$, the dynamics of elastic scattering is dependent only on the deviation angle in the COM, i.e.:

$$P(\mathbf{v}, \mathbf{V} \rightarrow \mathbf{v}') = P(\mathbf{u} \rightarrow \mathbf{u}') = \frac{\delta(u - u')}{2\pi u'^2} P(\mu_{\text{COM}}), \quad (2.21)$$

where we considered the invariance by rotation around \mathbf{u} , and $P(\mu_{\text{COM}})$ derives from interaction models or measurements. For isotropic scattering it is equal to one half.

2.1.2 Range of integration

From kinematic arguments we can find the allowed neutron exiting energies depending on the deviation angle. Eliminating c from (2.6a), and squaring the result, we obtain the basic relation between μ_{LAB} and μ_{COM} :

$$v^2 + v'^2 - 2vv'\mu_{\text{LAB}} = 2u^2(1 - \mu_{\text{COM}}). \quad (2.22)$$

The latter can be conveniently re-expressed in terms of energies:

$$\mu_{\text{COM}} = 1 - \beta^2 \frac{\hat{D}}{2E_r}, \quad (2.23)$$

where

$$\hat{D} = E + E' - 2\sqrt{EE'}\mu_{\text{LAB}}. \quad (2.24)$$

and E_r is the relative energy.

The Doppler-broadened transfer kernel will be obtained by an integration over E_r . The range of allowed E_r and μ_{COM} per given E , E' , and μ_{LAB} can be found

considering (2.23). Imposing the condition $|\mu_{\text{LAB}}| \leq 1$ we found a constrain for the product $E_r(1 - \mu_{\text{COM}})$, i.e.:

$$E_r^- \leq E_r \frac{1 - \mu_{\text{COM}}}{2} \leq E_r^+ \quad (2.25)$$

where

$$E_r^\pm = \left[\frac{\beta}{2} (\sqrt{E} \pm \sqrt{E'}) \right]^2. \quad (2.26)$$

Upon defining

$$E_* = \left(\frac{\beta}{2} \right)^2 \hat{D} = E_r \frac{1 - \mu_{\text{COM}}}{2}, \quad (2.27)$$

and considering the condition $|\mu_{\text{COM}}| \leq 1$, the range of integration is given by (Sanchez et al., 2013):

$$E_* \leq E_r \leq \infty. \quad (2.28)$$

Figure 2.2, based on Sanchez et al. (2013), represents graphically the bounds for μ_{COM} versus E_r .

2.1.3 Computation of the transfer kernel

The Doppler-broadened transfer kernel is given by the convolution integral

$$P_T(E \rightarrow E', \mu_{\text{LAB}}) = \frac{1}{v\sigma_T(E)} \int_{\infty} dV M_T(V) v_r \sigma(E_r) P(\mathbf{v}, \mathbf{V} \rightarrow E', \mu_{\text{LAB}}), \quad (2.29)$$

where $\sigma_T(E)$ is the Doppler-broadened cross-section for neutrons with initial energy E , $M_T(V)$ is the Maxwellian distribution for the target nuclei speed V at temperature T in K, and $\sigma(E_r)$ is the scattering cross section at 0 K.

The dynamics of the collision are described by the scattering kernel,

$$P(\mathbf{v}, \mathbf{V} \rightarrow E', \mu_{\text{LAB}}) = \int_{\infty} d\mathbf{v}' P(\mathbf{v}, \mathbf{V} \rightarrow \mathbf{v}') \delta \left(E' - \frac{m}{2} v'^2 \right) \delta (\mu_{\text{LAB}} - \boldsymbol{\Omega} \cdot \boldsymbol{\Omega}'), \quad (2.30)$$

which gives the density of probability for a scattering event (\mathbf{v}, \mathbf{V}) to result in a scattered neutron with energy E' and cosine of scattering in the laboratory frame of reference μ_{LAB} . It comes from the integration of (2.19) over the neutron velocity \mathbf{v}' after scattering imposing delta functions to select the desired couple (E', μ_{LAB}) .

Following Ouisloumen and Sanchez (1991), we first simplify (2.30) by introducing the change of variables $\mathbf{u}' = \mathbf{v}' - \mathbf{c}$. Taking into account (2.20) and (2.21)

we get:

$$P(\mathbf{v}, \mathbf{V} \rightarrow E', \mu_{\text{LAB}}) = \int_{\infty} du' u'^2 \int_{-1}^1 d\mu' \int_0^{2\pi} d\phi' \frac{\delta(u - u')}{2\pi u'^2} P(\mu_{\text{COM}}) \delta\left(E' - \frac{m}{2}v'^2\right) \delta(\mu_{\text{LAB}} - \boldsymbol{\Omega} \cdot \boldsymbol{\Omega}'). \quad (2.31)$$

Using the scaling and symmetry properties of the delta function and with the help of (2.14b), we may write:

$$\delta\left(E' - \frac{m}{2}v'^2\right) = \frac{1}{mcu} \delta\left(\mu' - \frac{1}{mcu} \left[E' - \frac{m}{2}(c^2 + u^2)\right]\right). \quad (2.32)$$

Inducing this result into (2.31) and considering the constrain $|\mu'| \leq 1$, we get:

$$P(\mathbf{v}, \mathbf{V} \rightarrow E', \mu_{\text{LAB}}) = \frac{H(E_+ - E')H(E' - E_-)}{mcu} Q, \quad (2.33)$$

where H is the Heaviside step function, $E_{\pm} = (m/2)(u \pm c)^2$ are the maximum and the minimum energies after scattering and

$$Q = P(\mu_{\text{COM}}) \frac{1}{\pi} \int_0^{\pi} d\phi' \delta(\mu_{\text{LAB}} - \boldsymbol{\Omega} \cdot \boldsymbol{\Omega}'). \quad (2.34)$$

We note that the integrand in the last integral is a function of $\cos(\phi' - \phi)$. However, since ϕ is arbitrary, we can replace the argument of Q with ϕ' . Furthermore, we have taken $P(\mu_{\text{COM}})$ out of the integral, because for a given kernel integration E , E' , and μ_{LAB} are fixed, and thus μ_{COM} does not depend on ϕ' , as we can see from (2.23). The interval of the integral over ϕ' is reduced by half, since the integrand is a function of $\cos \phi'$, that is even.

We turn now to (2.29). By introducing the change of variable $\mathbf{V} \rightarrow \mathbf{v}_r$ we have

$$d\mathbf{V} = d\mathbf{v}_r = v_r^2 dv_r d\boldsymbol{\Omega}_{\text{COM}}. \quad (2.35)$$

In the new integration variable \mathbf{v}_r , c depends on \mathbf{v}_r , as expressed in (2.6a). We consider therefor a spherical coordinates system having \mathbf{v} as polar axis, in which $\boldsymbol{\Omega}_{\text{COM}}$ is defined by the couple (μ_v, ϕ_v) with $\mu_v = \cos(\mathbf{v}, \mathbf{v}_r)$. The Doppler-broadened transfer kernel results:

$$P_T(E \rightarrow E', \mu_{\text{LAB}}) = \frac{1}{v\sigma_T(E)} \int_0^{\infty} dv_r v_r^3 \sigma(E_r) \int_{-1}^1 d\mu_v \int_0^{2\pi} d\phi_v M_T(V) P(\mathbf{v}, \mathbf{V} \rightarrow E', \mu_{\text{LAB}}). \quad (2.36)$$

The integral over $d\phi_v$ is easily found considering the invariance by rotation around v . Regarding $d\mu_v$, by squaring $c = v - \beta^{-1}v_r$ we can express μ_v in terms of c , namely:

$$\mu_v = \frac{\beta^2(v^2 - c^2) + v_r^2}{2\beta v v_r}. \quad (2.37)$$

Equation (2.36) is subsequently re-expressed as:

$$P_T(E \rightarrow E', \mu_{\text{LAB}}) = \frac{2\pi\beta}{v^2\sigma_T(E)} \int_0^\infty dv_r v_r^2 \sigma(E_r) \int dc H(E_+ - E) H(E - E_-) c M_T(V) P(v, \mathbf{V} \rightarrow E', \mu_{\text{LAB}}), \quad (2.38)$$

where the two Heaviside step functions emerge from the constrain $|\mu_v| \leq 1$.

The Maxwellian spectrum is given by (Bell and Glasstone, 1970):

$$M_T(V) = \frac{Am^{\frac{3}{2}}}{2\pi kT} \exp\left(-\frac{AmV^2}{2kT}\right) \quad (2.39)$$

where k is the Boltzmann constant, and V can be conveniently expressed in terms of v , c , and v_r . Defining the constant (in s m^{-1}):

$$\xi = \sqrt{\frac{(A+1)m}{2kT}}, \quad (2.40)$$

we can introduce the following dimensionless quantities:

$$x = \xi c, \quad (2.41a)$$

$$t = \xi u, \quad (2.41b)$$

$$\varepsilon = \xi v = \xi \sqrt{\frac{2}{m}} \sqrt{E}, \quad (2.41c)$$

$$\varepsilon' = \xi v' = \xi \sqrt{\frac{2}{m}} \sqrt{E'}, \quad (2.41d)$$

$$D = \xi^2 \frac{2}{m} \hat{D}. \quad (2.41e)$$

After replacement of (2.33), (2.39), and (2.41) in (2.38), we obtain

$$P_T(E \rightarrow E', \mu_{\text{LAB}}) = \frac{A\beta^{3/2}}{2\sqrt{\pi}kTE\sigma_T(E)} \int_0^\infty dE_r e^{-(E_r - \beta E)/\gamma} \sigma(E_r) \int dx H(E_+ - E_{\text{max}}) H(E_{\text{min}} - E_-) e^{-x^2} Q, \quad (2.42)$$

where $\gamma = \beta kT$, $E_{\text{max}} = \max(E, E')$, and $E_{\text{min}} = \min(E, E')$.

The calculation of $P_T(E \rightarrow E', \mu_{\text{LAB}})$ requires the computation of Q , that in turn involves an integration over ϕ' . Making use of (2.41), (2.17) can be reformulated in the reduced energy variables:

$$\mathbf{\Omega} \cdot \mathbf{\Omega}' = \frac{\tilde{B} + \tilde{C} \cos \phi'}{4x^2 \varepsilon \varepsilon'}, \quad (2.43)$$

where

$$\tilde{B} = \zeta^4 B = [\varepsilon^2 - \lambda] [\varepsilon'^2 - \lambda], \quad (2.44a)$$

$$\tilde{C}^2 = (\zeta^4 C)^2 = [(\varepsilon^2 - \lambda)^2 - (2\varepsilon x)^2] \left[(\varepsilon'^2 - \lambda)^2 - (2\varepsilon' x)^2 \right], \quad (2.44b)$$

with

$$\lambda = t^2 - x^2. \quad (2.45)$$

Employing the properties of symmetry and scaling of the delta function, and using the expression (2.43) for $\mathbf{\Omega} \cdot \mathbf{\Omega}'$, the integral over ϕ' in (2.34) becomes:

$$Q = P(\mu_{\text{COM}}) H(\mu_{\text{LAB}}^+ - \mu_{\text{LAB}}) H(\mu_{\text{LAB}} - \mu_{\text{LAB}}^-) \frac{1}{\pi} \frac{4x^2 \varepsilon \varepsilon'}{\tilde{C} |\sin \phi'|}, \quad (2.46)$$

where the Heaviside step functions come from the condition $|\cos \phi'| \leq 1$, with $\mu_{\text{LAB}}^\pm = (\tilde{B} \pm \tilde{C}) / (4x^2 \varepsilon \varepsilon')$. The condition $|\cos \phi'| \leq 1$ applied to (2.43) gives:

$$F = \tilde{C}^2 - (4x^2 \varepsilon \varepsilon' \mu_{\text{LAB}} - \tilde{B})^2 \geq 0. \quad (2.47)$$

Since $\tilde{C}^2 \sin^2 \phi' = \tilde{C}^2 - \tilde{C}^2 \cos^2 \phi'$, (2.46) may be reformulated as follows:

$$Q = P(\mu_{\text{COM}}) H(F) \frac{1}{\pi} \frac{4x^2 \varepsilon \varepsilon'}{\sqrt{F}}. \quad (2.48)$$

Also, since μ_{COM} does not depend on x for given E , E' , μ_{LAB} , and E_r , it can be taken outside the innermost integral of (2.42).

After a bit of algebra, the integral over x in (2.42) can be recast as (Sanchez, 2013):

$$\int dx H(E_+ - E_{\text{max}}) H(E_{\text{min}} - E_-) e^{-x^2} Q = H(E_r - E_*) P(\mu_{\text{COM}}) \frac{\varepsilon \varepsilon'}{\sqrt{D}} \exp(-\varepsilon \varepsilon' \mu_{\text{LAB}} - t^2) \frac{1}{\pi} \int_{-1}^1 dz \frac{e^{\eta z}}{\sqrt{1 - z^2}}, \quad (2.49)$$

with

$$\eta = \varepsilon \varepsilon' \sqrt{(1 - \mu_{\text{LAB}}^2) \left(\frac{4t^2}{D} - 1 \right)}, \quad (2.50)$$

and

$$\eta z = \lambda + \varepsilon \varepsilon' \mu_{\text{LAB}}. \quad (2.51)$$

Following Blackshow and Murray (1967), after a change of variable we have:

$$\frac{1}{\pi} \int_{-1}^1 dz \frac{e^{\eta z}}{\sqrt{1-z^2}} = \frac{1}{\pi} \int_0^\pi d\phi e^{\eta \cos \phi} = I_0(\eta). \quad (2.52)$$

Wrapping-up all the elements of the Doppler-broadened transfer kernel integral, we obtain the final expression:

$$P_T(E \rightarrow E', \mu_{\text{LAB}}) = \left(\frac{\beta}{kT} \right)^{\frac{3}{2}} \frac{A\sqrt{A+1}}{2\sqrt{\pi}\hat{D}\sigma_T(E)} \sqrt{\frac{E'}{E}} \int_{E_*}^{\infty} dE_r e^{-\frac{A}{kT}(E_r - E_0)} \sigma(E_r) P(\mu_{\text{COM}}) I_0(\eta), \quad (2.53)$$

where

$$E_0 = E/A - \beta\sqrt{EE'}\mu_{\text{LAB}}. \quad (2.54)$$

We note that (2.53) was derived earlier in a different way by Blackshow and Murray (1967). This equation contains a divergence term at $E' = E$ for $\mu_{\text{LAB}} \rightarrow 1$, that corresponds to the delta behavior for coherent scattering at constant energy.

2.1.4 Calculation of the angular moments

Once the calculation of the Doppler-broadened transfer kernel has been done, it is possible to compute its moments by quadrature:

$$P_{m,T}(E \rightarrow E') = \int_{-1}^1 d\mu_{\text{LAB}} P_T(E \rightarrow E', \mu_{\text{LAB}}) P_m(\mu_{\text{LAB}}), \quad (2.55)$$

where $P_m(\mu_{\text{LAB}})$ is the Legendre polynomial of order m .

It has to be underlined that this methodology to compute the moments is different from that in previous works, where the moments were directly calculated from (2.38), resulting in μ_{COM} being a function of ϕ' via the relation $\mu_{\text{LAB}} = \mathbf{\Omega} \cdot \mathbf{\Omega}'$ and preventing taking the $P_m(\mu_{\text{COM}})$ out of the integral in ϕ' , as we have done for the calculation of the kernel in (2.34).

2.2 Numerical implementation

2.2.1 Kernel computation

The Doppler-broadened transfer kernel given in (2.53) involves the computation of two non-algebraical functions: the exponential and the modified Bessel function

of order 0, that have been both tabulated at constant step to speed-up the computation of the integral. In particular, the tabulation of the exponential function is constructed for $x \in [0, x_{\text{exp}}]$ such that $e^{-x_{\text{exp}}}$ is very small. The Bessel function has been represented as $I_0(\eta)e^{-\eta}$ to avoid overflows, with a complementary asymptotic expansion for higher η values².

Since the total integration over E_r has to be done from the minimum energy E_* to infinity, we can introduce a method to limit the integration range. With the contribution e^η the exponent of the exponential in the integral in E_r in (2.53) becomes

$$-\frac{A}{kT}(E_r - E_0) + \eta, \quad (2.56)$$

that can be rewritten as

$$-(x - b)^2 + c + b^2, \quad (2.57)$$

with

$$x = \sqrt{\frac{A}{kT}(E_r - E_*)}, \quad (2.58a)$$

$$c = \frac{A}{kT}(E_0 - E_*), \quad (2.58b)$$

$$b = \sqrt{\frac{AEE'(1 - \mu_{\text{LAB}}^2)}{kT\hat{D}}}. \quad (2.58c)$$

Since we set to zero the exponential function if the exponent is a negative number whose absolute value is greater than x_{exp} , we can greatly restrict the range of integration in E_r in (2.53).

Considering that c and b do not depend on E_r , the effective range of integration in E_r is constrained by

$$(x - b)^2 \leq x_{\text{exp}} + c + b^2 = x_c^2. \quad (2.59)$$

Noting that $c + b^2 \leq 0$ we proceed as follows. If $x_c^2 = 0$ we set the kernel directly to zero, otherwise we solve for E_r to obtain the final range of integration:

$$E_* + \frac{kT}{A}(\max(0, b - x_c))^2 \leq E_r \leq E_* + \frac{kT}{A}(b + x_c)^2. \quad (2.60)$$

Finally, since $\sigma(E_r)$ is given as a continuous piecewise linear tabulation by NJOY (MacFarlane and Muir, 2000), the integral in (2.53) is computed by applying a Gauss-Legendre quadrature to each piece were $\sigma(E_r)$ is linear.

²The Bessel function $I_0(\eta)$ has been computed using a modified version of the routines provided in the SPECFUN package: <http://www.netlib.org/specfun>.

2.2.2 Angular moments calculation

We calculate the moments via numerical Gauss-Legendre quadrature of (2.55):

$$P_{m,T}(E \rightarrow E') \approx \sum_n w_n P_T(E \rightarrow E', \mu_n) P_m(\mu_n). \quad (2.61)$$

Moreover, instead of computing the kernel at the quadrature abscissas, we introduce a representation of the kernel as a continuous function $f(\mu)$ and we use it to compute the values at the quadrature abscissas. This gives

$$\begin{aligned} P_T(E \rightarrow E', \mu_n) &= \sum_k \left[P_T(E \rightarrow E', \mu_k) \prod_{k \neq k'} \frac{\mu_n - \mu_{k'}}{\mu_k - \mu_{k'}} \right] \\ &= \sum_k [P_T(E \rightarrow E', \mu_k) f_k(\mu_n)], \end{aligned} \quad (2.62)$$

where we have assumed that the representation is locally polynomial over the nodes $\{\mu_k\}$ and where $f_k(\mu_n)$ represents the contribution of the value of the kernel at the representation node μ_k to the interpolated value of the kernel at the quadrature node μ_n . Then, by inserting (2.62) into (2.61) we get:

$$P_{m,T}(E \rightarrow E') \approx \sum_k P_T(E \rightarrow E', \mu_k) \sum_n w_n f_k(\mu_n) P_m(\mu_n). \quad (2.63)$$

We have implemented two types of representations: a Gauss-Legendre collocation (GLC) and a continuous piecewise linear interpolation (CPL). In the former $f(\mu)$ is a Legendre polynomial of order K and it is fully determined by evaluating the kernel at the zeros of the Legendre polynomial $P_{K+1}(\mu)$. This global representation is not ensured to be always positive over $[-1, 1]$. The latter, instead, is based on partitioning $[-1, 1]$ into K segments on which we construct a continuous piecewise function which is fully determined by the values of the kernel at the $K + 1$ nodes (including -1 and 1) used for the partitioning. There are two advantages for using a representation. The first is that the kernels need to be evaluated only at the nodes of the representation and not at the quadrature nodes, and the second is that knowing the representation one can adapt the type and order of the numerical quadrature so it gives the exact integral.

There is still a special case to be considered, i.e. $E' = E$, for which it is found that (2.53) behaves as $1/\sqrt{1 - \mu_{\text{LAB}}}$ and hence is singular at $\mu_{\text{LAB}} = 1$. However, with an appropriate change of variables it is possible to compute the Doppler-broadened angular moments for $E' = E$. Following Abramowitz and Stegun (1964), we perform the change of variable $\mu = 1 - 2x^2$ to rewrite the angular

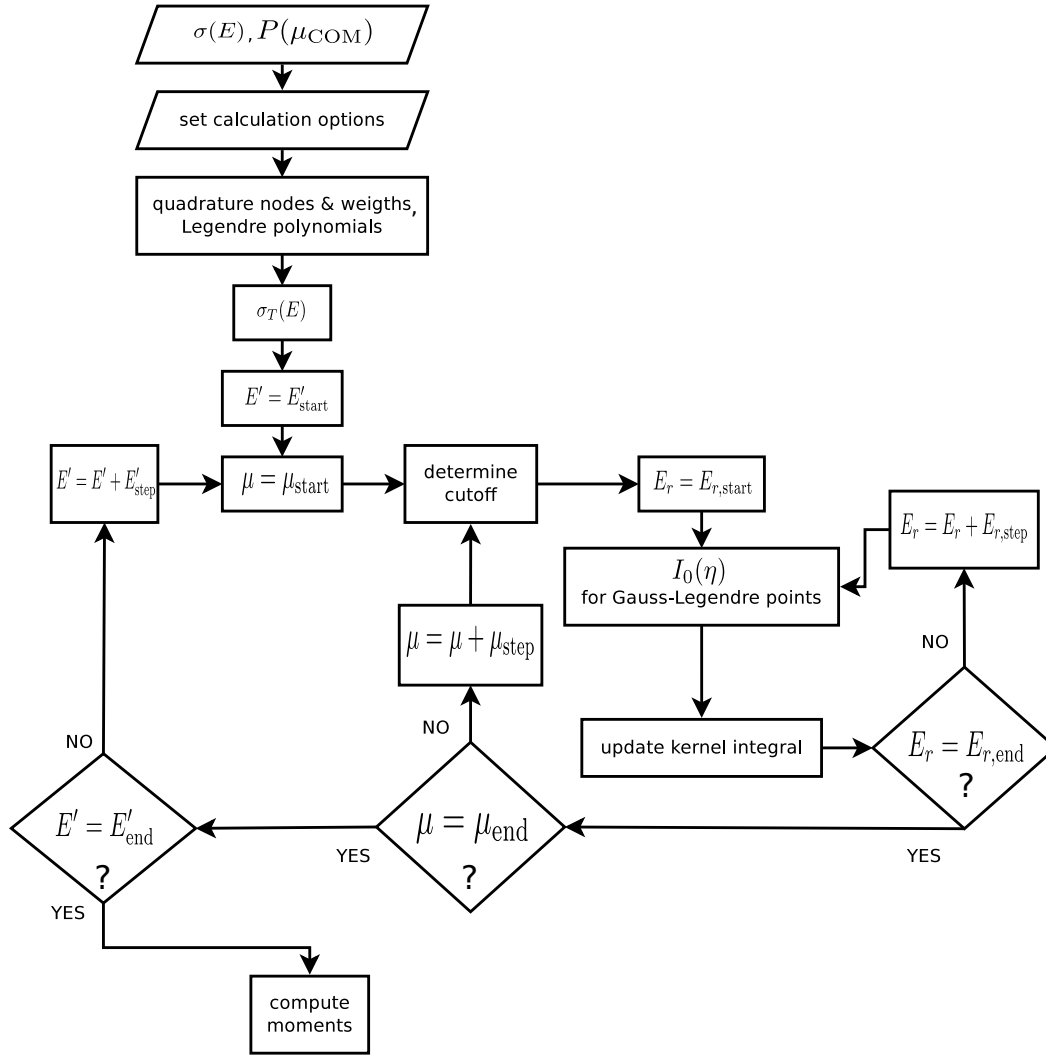


Figure 2.3 Flowchart of the computation of Doppler-broadened angular moments.

moment integral as:

$$\int_{-1}^1 d\mu \frac{P(\mu)}{\sqrt{1-\mu}} P_m(\mu) = 2\sqrt{2} \int_0^1 dx P(\mu) P_m(\mu), \quad (2.64)$$

where $P(\mu)$ is the value of the kernel excluding the troublesome factor $1/\sqrt{1-\mu_{\text{LAB}}}$.

2.2.3 Flowchart of the implementation

The implementation of the algorithm described so far is depicted in the flowchart of Figure 2.3. There are three main steps:

1. pre-processing;

2. kernel computation;
3. angular moments calculation.

The cross section data $\sigma(E_r)$ to be used for the computation of the Doppler-broadened transfer kernel is provided by a continuous piecewise linear tabulation at 0 K. In our case we used the mesh computed with NJOY (MacFarlane and Muir, 2000), that contains more than 451 000 entries covering the domain $E_r \in [1 \times 10^{-5} \text{ eV}, 30 \text{ MeV}]$. The deviation probability $P(\mu_{\text{COM}})$ is loaded as well; otherwise the scattering is supposed to be isotropic the the COM. Afterwards, we compute the nodes and weights for the selected quadrature and the Legendre polynomials needed for the integral of (2.61). The constant step tabulation for exp and I_0 is subsequently prepared and loaded into memory. Also, the code perform the Doppler convolution of the cross section for the impinging energy E to obtain $\sigma_T(E)$.

For a given E' and μ_{LAB} , we perform the kernel computation by means of (2.53), considering the cutoff (2.60). The integration over E_r is performed with a Gauss-Legendre approach for each interval defined by the cross section tabulation provided by NJOY. The computation is repeated for all the μ_{LAB} of the given moments representation, either GLC or CPL. Finally, the angular moments up to the order requested are evaluated for all the desired exiting energies E' by numerical quadrature. The user can decide to compute only the Doppler-broadened transfer kernel if the angular moments are not needed.

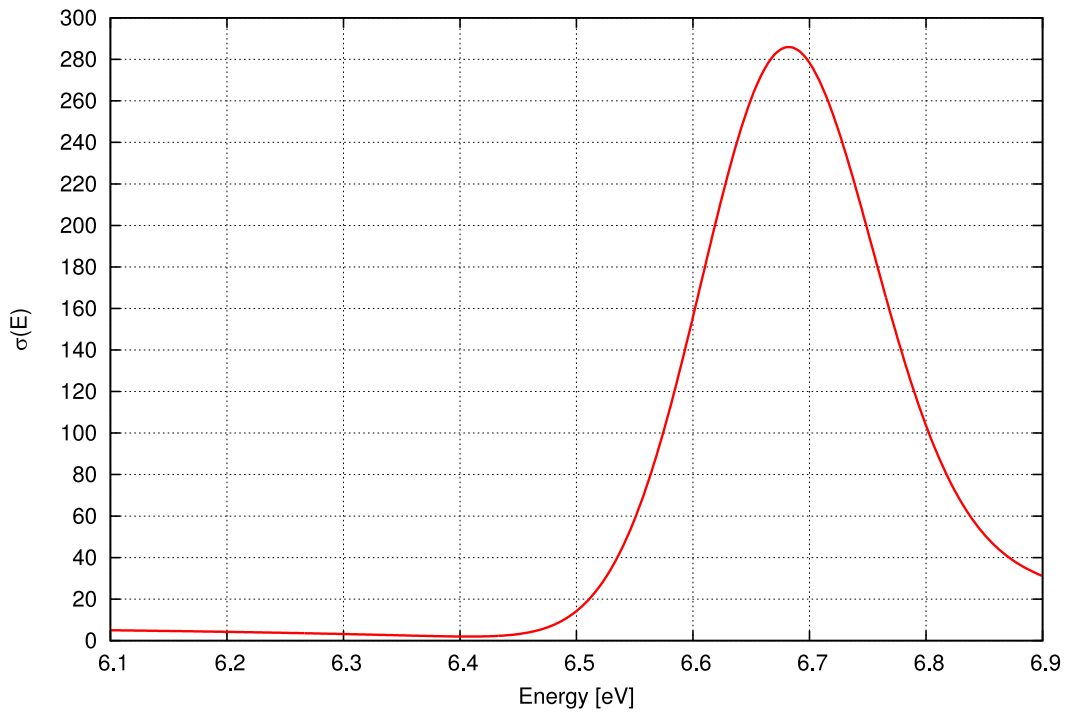
All our calculations are performed with a double precision floating point representation to provide maximum accuracy.

2.3 Numerical results

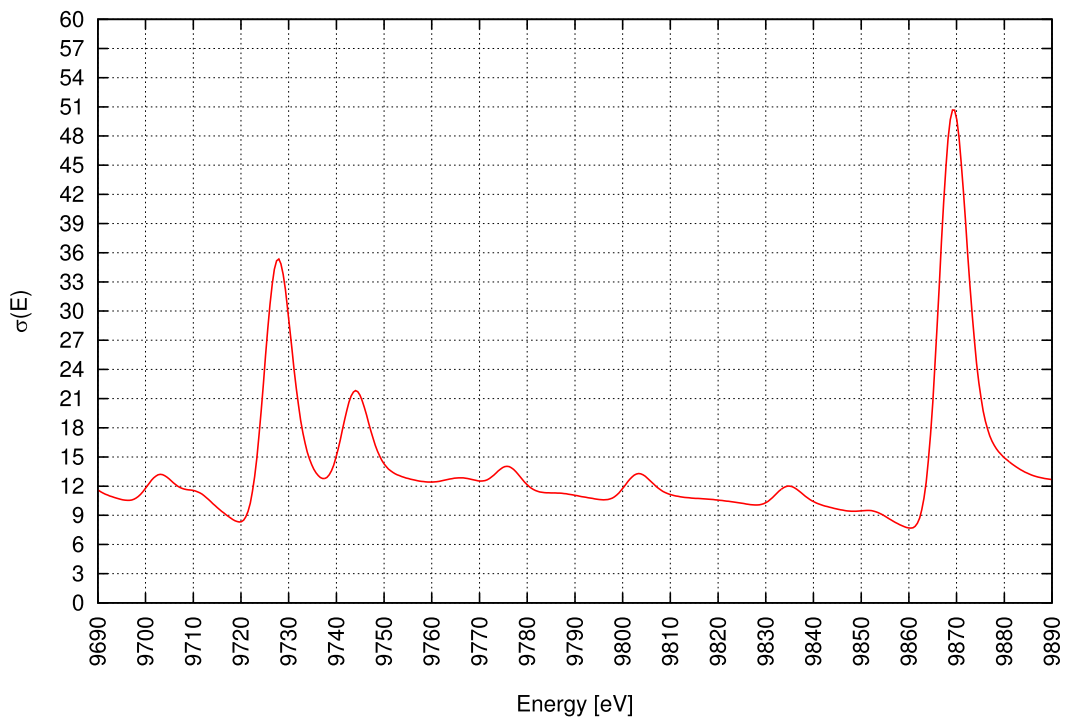
Having illustrated the mathematical formulation and the numerical implementation of the algorithm, we shall now proceed with the presentation of the capabilities of this approach, including comments on the peculiar behavior of the Doppler-broadened scattering kernel and its angular moments in the vicinity of the resonance for heavy isotopes. The results will be compared with the asymptotic kernel rigorously valid only at 0 K (Hébert, 2009):

$$P_{T=0}(E \rightarrow E', \mu_{\text{LAB}}) = \frac{1}{1-\alpha} \delta \left[\mu - \frac{1}{2}(A+1)\sqrt{\frac{E'}{E}} + \frac{1}{2}(A-1)\sqrt{\frac{E}{E'}} \right] H(E' - \alpha E) H(E - E') \quad (2.65)$$

where $\alpha = (A-1)^2 / (A+1)^2$.

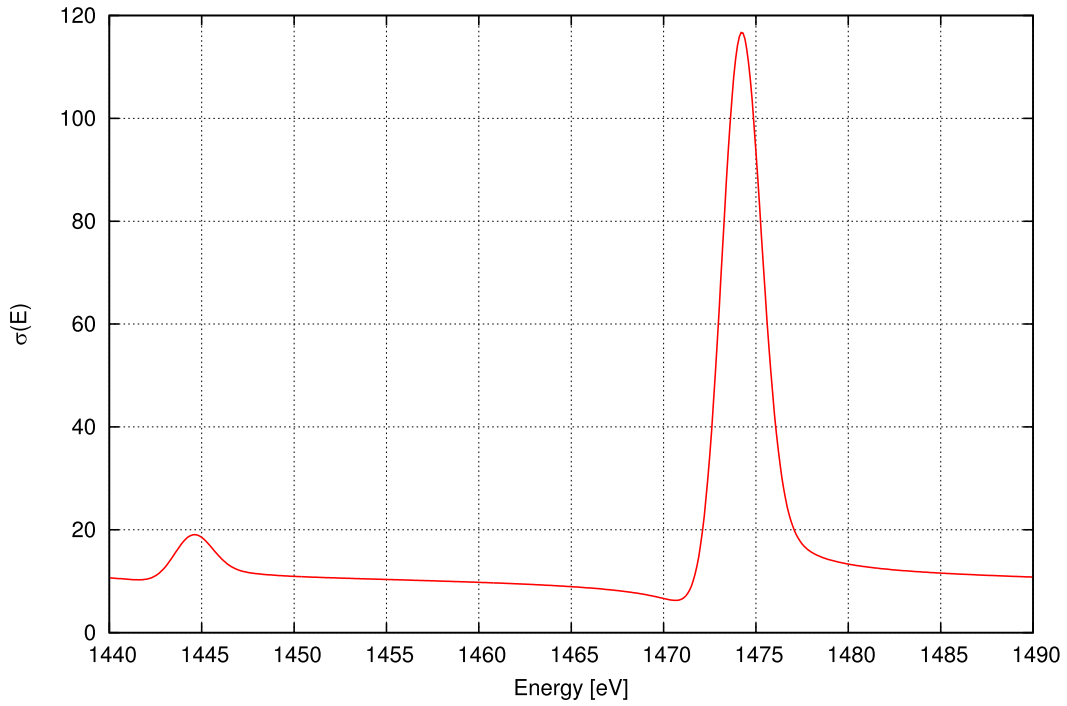


(a) around 6.67 eV

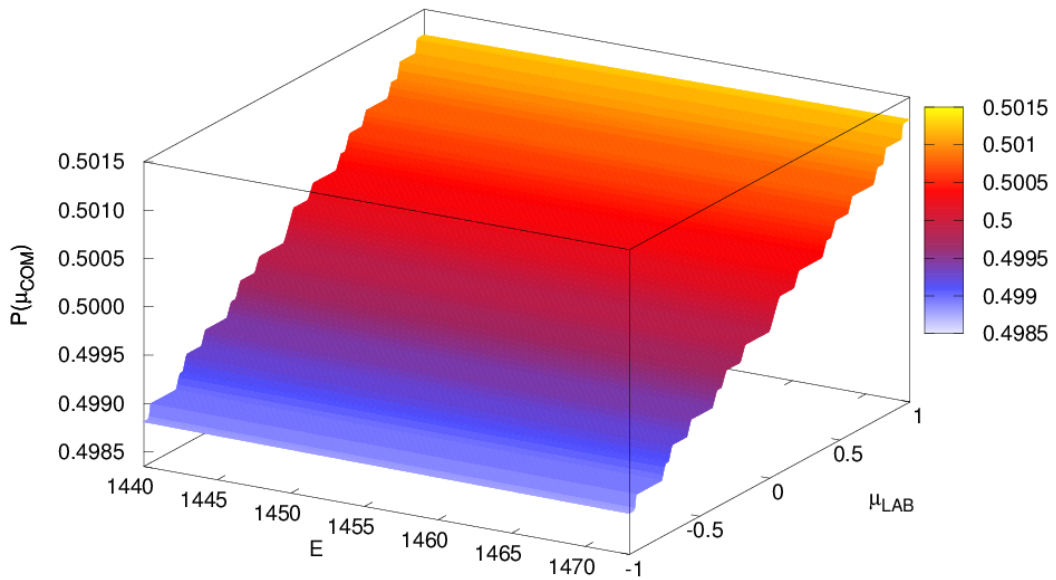


(b) around 9869 eV

Figure 2.4 Elastic scattering cross section for ^{238}U at 1000 K near various resonances.



(a) cross section



(b) anisotropy

Figure 2.5 Elastic scattering cross section for ^{238}U near the 1474 eV resonance at 1000 K and its degree of anisotropy.

In doing so, we examine the cases of constant cross section and real cross section of ^{238}U around the resonances at various temperature, for both isotropic and anisotropic scattering law. More specifically, we refer to the resonances of ^{238}U at 6.67 eV and 9869 eV for the isotropic case (Figure 2.4), and at 1474 eV for the anisotropic case (Figure 2.5)

2.3.1 Kernel computation

First of all we consider the constant cross section case for isotropic scattering in the COM, for which a closed analytic representation of $P_T(E \rightarrow E', \mu_{\text{LAB}})$ is already known and is reported by Bell and Glasstone (1970). It is a simple case useful to test the efficiency and the precision of our methodology.

We performed the computation with a Gauss-Legendre quadrature of order $N = 5$ with $M = 2$ subdivisions in each interval of the cross section tabulation, and we set $x_{\text{exp}} = 30$, for which the cutoff discussed in the previous section is given by $e^{-30} \simeq 9 \times 10^{-14}$. As expected, the absolute difference between the numerical and the analytical calculation is bigger for $E' \approx E$ and $\mu_{\text{LAB}} \approx 1$, where the Doppler-broadened kernel is close to a singularity. Still, this difference is found always less than 1×10^{-6} , confirming the validity of our approach and in particular of the exponential cutoff of (2.60). Figure 2.6 depicts $P_T(E \rightarrow E', \mu_{\text{LAB}})$ close to this singularity. It is interesting to note the peculiar behavior given by the analytical formula: while for $E = E'$ there is a delta-like trend for $\mu_{\text{LAB}} = 1$, in the other cases the Doppler-broadened kernel presents a maximum before dropping to zero at $\mu_{\text{LAB}} = 1$.

Dependence on medium temperature

We now proceed to some realistic results for ^{238}U with isotropic scattering law in the COM, keeping the same settings regarding tabulations and cutoff.

Figure 2.7 and Figure 2.9 reports the full dependency of the Doppler-broadened scattering kernel at 50 K, 273 K, and 1000 K for an entering neutron energy $E = 6.5$ eV, for both the constant and ^{238}U cross sections, respectively. These figures have been generated from the computation of the Doppler-broadened kernel on a grid of 1000 points in the E' variable and 500 points in the μ_{LAB} variable.

For the constant cross section case we computed the transfer kernel using the analytic expression given by Bell and Glasstone (1970), while for the ^{238}U case we employed the algorithm described so far. The computing time for the latter, including the overhead for initialization, statistics and printouts for the later 3D rendering, was 105 s on an Intel® Xeon® E5645 at 2.4 GHz. This time accounts for an average of 2.1×10^{-4} s per kernel integration.

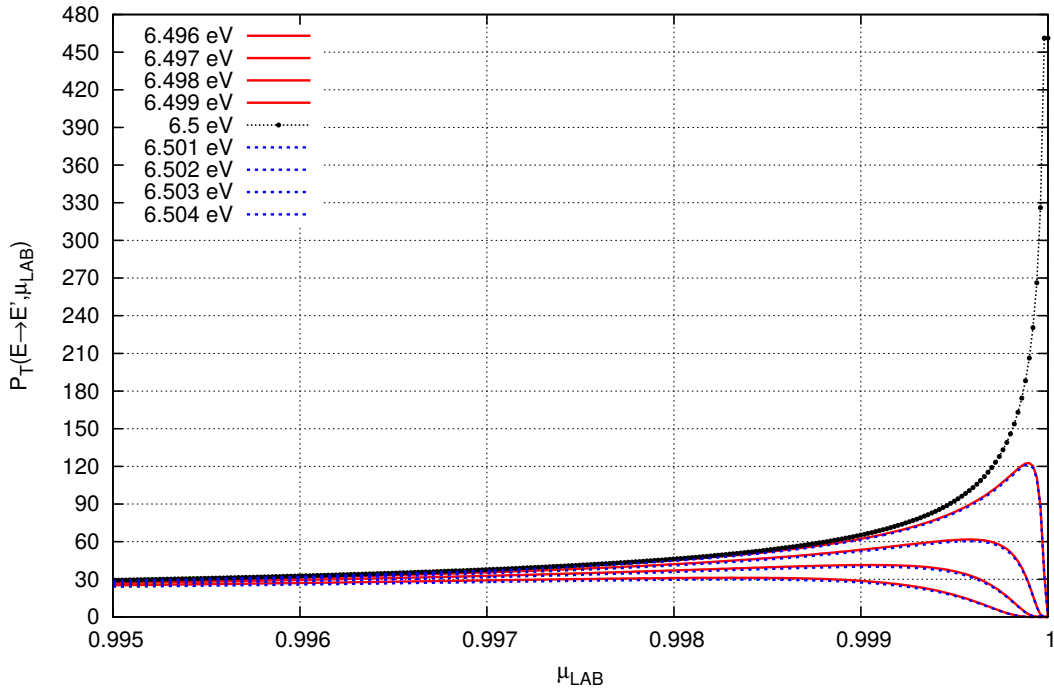


Figure 2.6 Analytical kernel at 1000 K for different E values versus μ_{LAB} for $\sigma = 1$ and $E = 6.5$ eV.

For the analytic case, the shape of the transfer kernel resembles the asymptotic expression (2.65) at low temperature. Once the temperature is increased, the transfer probability drift apart the rigid delta-like behavior, while maintaining its maximum values in the down-scattering range, and maintaining the singularity at $E' = E$ for $\mu_{\text{LAB}} = 1$. The broadening of the peaks is also depicted in Figure 2.8, that shows the the values of the kernel ranging from back-scattering ($\mu_{\text{LAB}} = -1$) to forward-scattering ($\mu_{\text{LAB}} = 0.99^3$).

For the ^{238}U case, at the lowest temperature the kernel resembles the asymptotic one, for which the probability is uniformly distributed between $E' \in [\alpha E, E]$. Once the temperature is raised, an increasing pronounced up-scattering is found, due to the presence of the resonance at 6.67 eV, with a peak around $\mu_{\text{LAB}} = -1$. This is even more evident in Figure 2.10, that shows the kernel cuts for various μ_{LAB} . For higher temperature the behavior at $\mu_{\text{LAB}} = -1$ is significantly different with respect the constant cross section case: the curve is in fact mostly in the up-scattering domain. At room temperature, instead, the discrepancy with respect to the asymptotic case is less evident, but still present.

As already found before (Ouisloumen and Sanchez, 1991; Sanchez et al., 2013),

³The Doppler-broadened scattering kernel is singular for $\mu_{\text{LAB}} = 1$. $\mu_{\text{LAB}} = 0.99$ has been chosen to depicts the behavior for forward-scattering

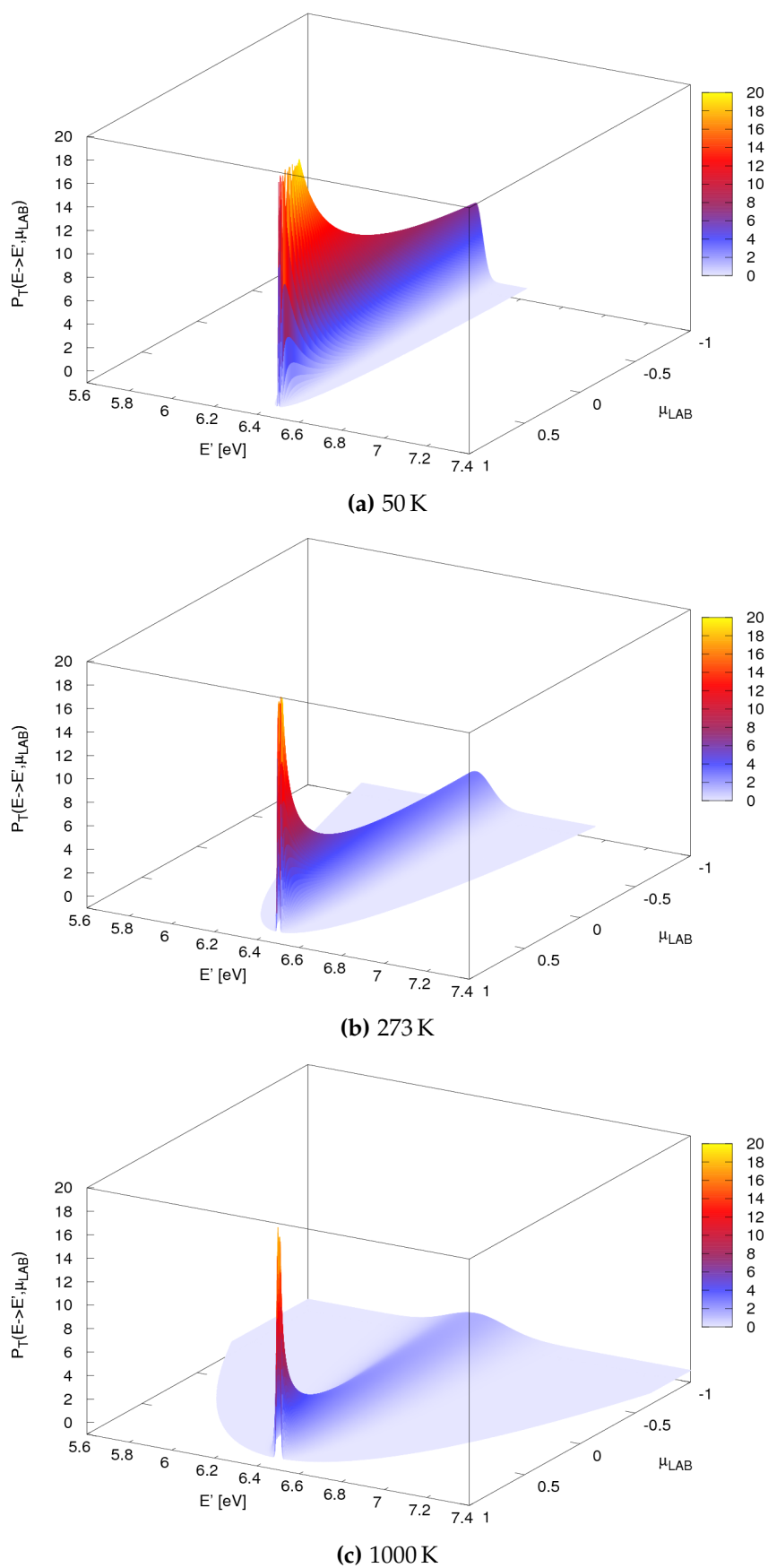
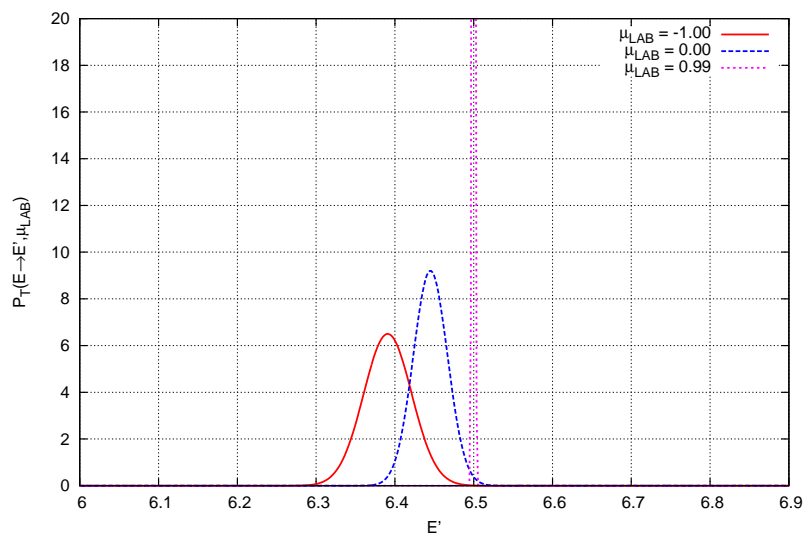
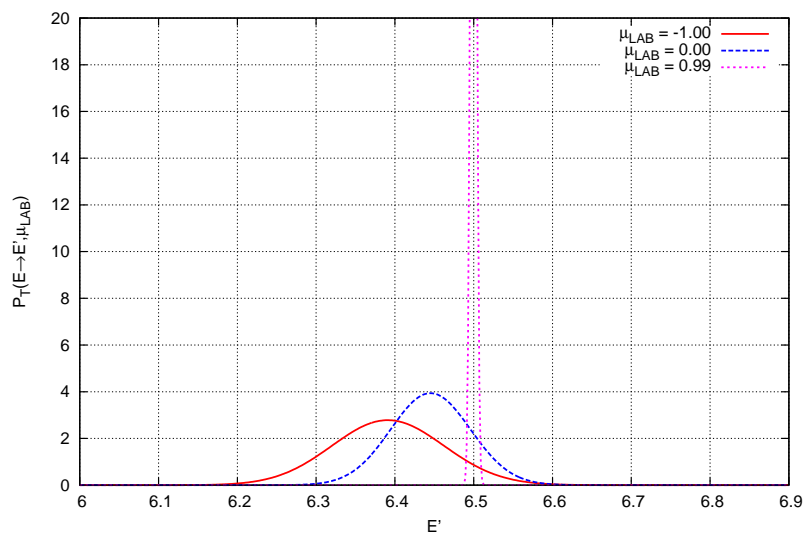


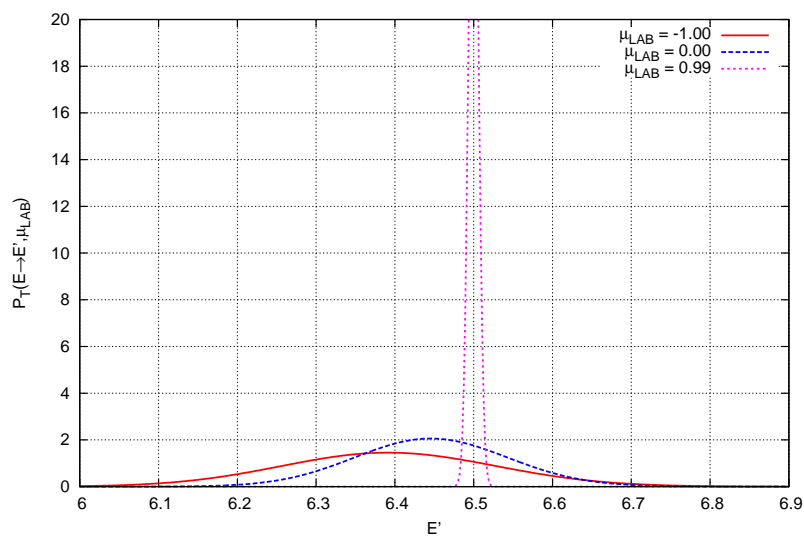
Figure 2.7 $P_T(E \rightarrow E', \mu_{\text{LAB}})$ for $E = 6.5$ eV near 6.67 eV for $\sigma = 1$. 3D rendering of the dependency upon μ_{LAB} and E' .



(a) 50 K



(b) 273 K



(c) 1000 K

Figure 2.8 $P_T(E \rightarrow E', \mu_{\text{LAB}})$ for $E = 6.5 \text{ eV}$ near 6.67 eV for $\sigma = 1$. Cuts for most significant μ_{LAB} . Higher temperatures result in a broadening of the peaks.

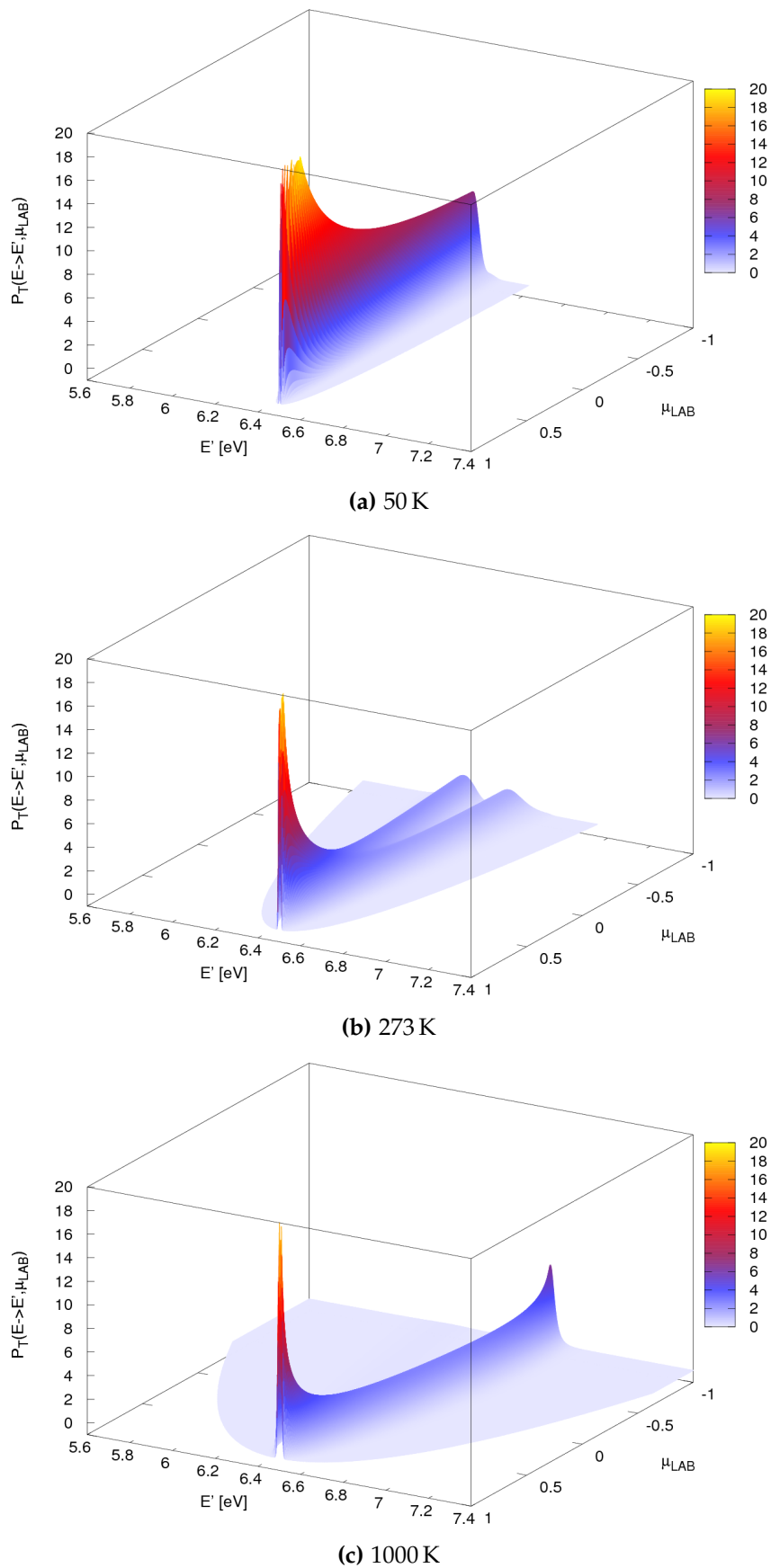
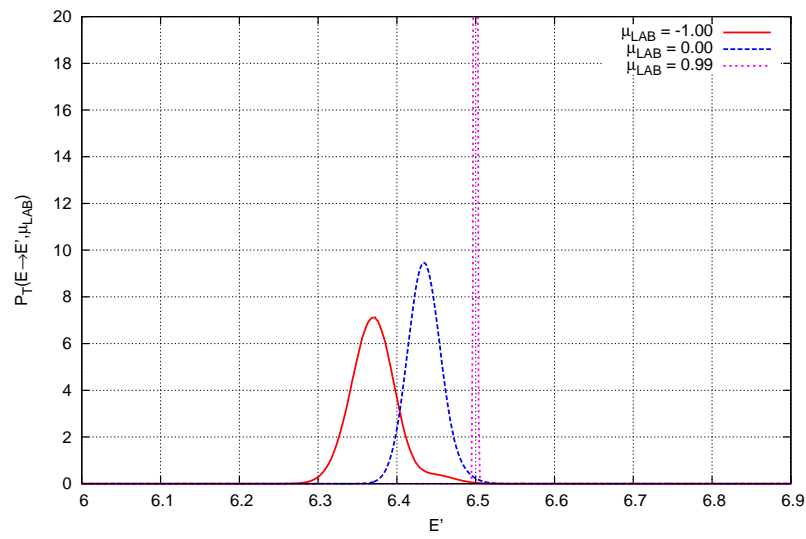
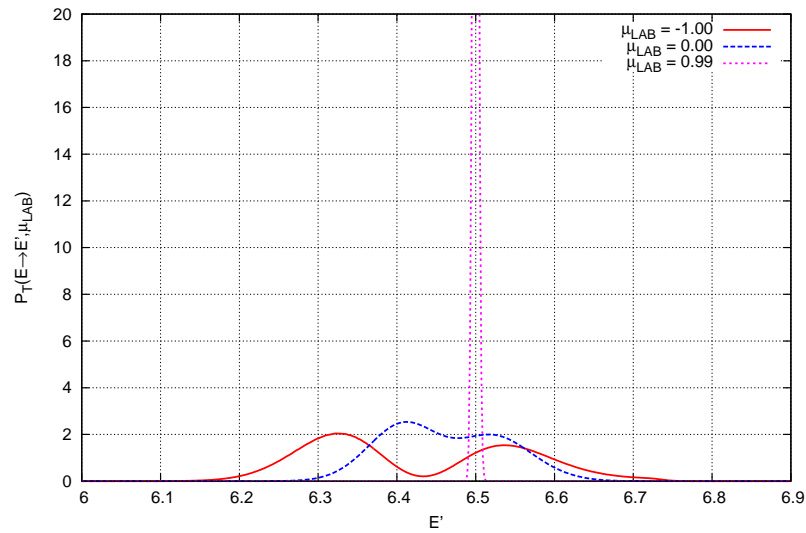


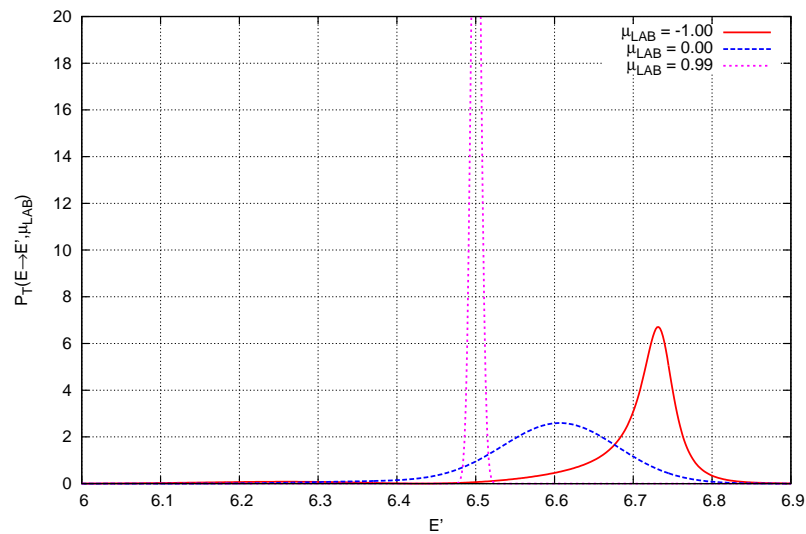
Figure 2.9 $P_T(E \rightarrow E', \mu_{\text{LAB}})$ for $E = 6.5$ eV near the 6.67 eV resonance of ^{238}U . 3D rendering of the dependency upon μ_{LAB} and E' .



(a) 50 K



(b) 273 K



(c) 1000 K

Figure 2.10 $P_T(E \rightarrow E', \mu_{\text{LAB}})$ for $E = 6.5$ eV near the 6.67 eV resonance of ^{238}U . Cuts for most significant μ_{LAB} . A strong up-scattering in backward directions is manifested for higher temperatures.

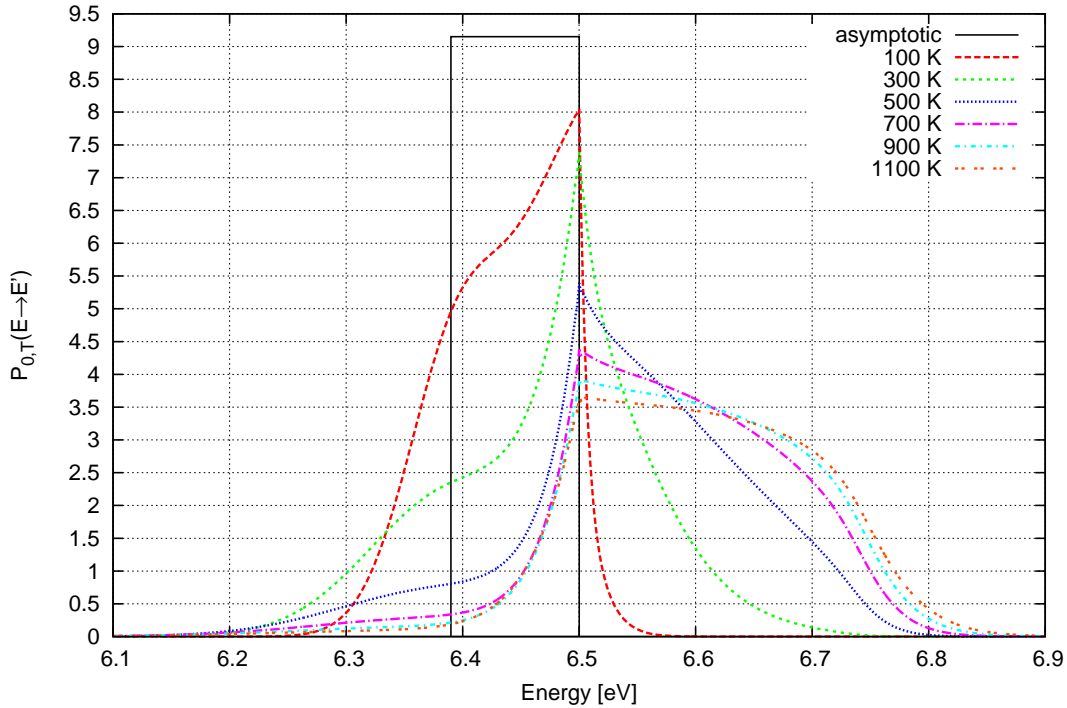


Figure 2.11 $P_{0,T}(E \rightarrow E')$ for ^{238}U for different values of T . The asymptotic model is depicted as a solid black line.

this up-scattering effect is pronounced only in the vicinity of the resonance energy, in particular on the left side. Outside the resonance energy, the behavior resembles the one of the constant cross section case. This effect promotes an increased probability of absorption, changing the reactivity feedback (Lee et al., 2008) and the final burn-up at the end of a fuel cycle in nuclear power plants (Zoia et al., 2013).

2.3.2 Angular moments calculation

The effect of temperature on the 0th angular moment for ^{238}U and $E = 6.5\text{eV}^4$ is depicted in Figure 2.11. It has been obtained from integration over μ_{LAB} of the temperature-dependent scattering kernel just presented. The figure reproduces with a black solid line the asymptotic model valid for $T = 0\text{K}$.

For the analysis of the plot, we note a progressive deviation for the asymptotic model once the temperature is raised, due to the combined influence of the thermal agitation and the resonance at 6.67 eV. Indeed, most of the probability moves from the down-scattering to the up-scattering domain. Therefore, in the following analysis of our algorithm for the computation of the angular moments we

⁴on the left side of the 6.67 eV resonance

concentrate to the cases at 1000 K, to better show the impact of thermal agitation.

We shall now proceed with the analysis of the behavior of the angular moments as a function of the representation used and of the energy of the impinging neutron.

Convergence analysis

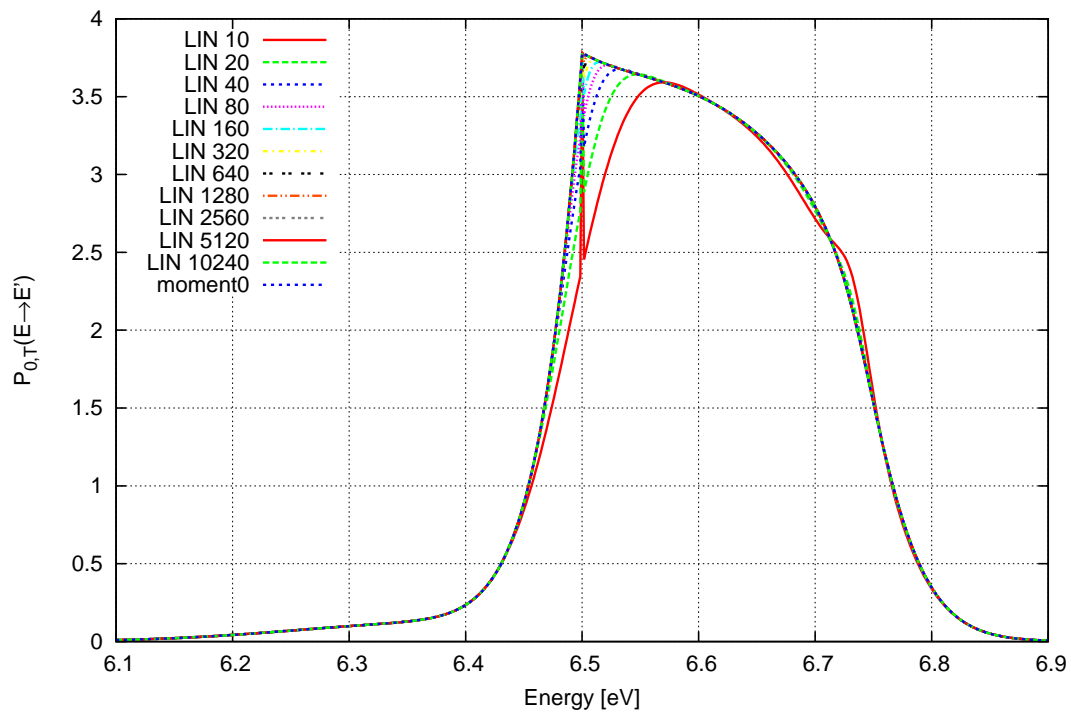
The accuracy of the angular moments calculation via (2.61) has been assessed for both CPL and GLC method. Figure 2.12 presents a convergence analysis for the values of the 0th moment for impinging neutrons at 6.5 eV. The reference values have been computed with the different methodology proposed by Sanchez et al. (2013). The cutoff and the quadrature order for the computation of the Doppler-broadened scattering kernel are the same of the previous section, while the quadrature order in the μ_{LAB} variable has been automatically determined considering the maximum possible order of the polynomial to be integrated.

As expected, a numerical difficulty shows up for energies $E' \simeq E$ because of the delta-like behavior of the kernel, while for $E' = E$ the change of variable of integration (2.64) provides always the correct result. Still, convergence is achieved by increasing the order of the representation. In particular, for the comparison between the present calculation and the reference, it turns out that the maximum relative difference for CPL is in the order of 1×10^{-2} with 640 points in the μ_{LAB} representation and in the order of 1×10^{-4} with 10 240 points. For GLC the maximum relative differences are 1×10^{-4} and 1×10^{-6} with 160 and 640 points, respectively. We should point out that difference appears only for $E' \approx E$, while outside this region smaller quadrature orders attain convergence.

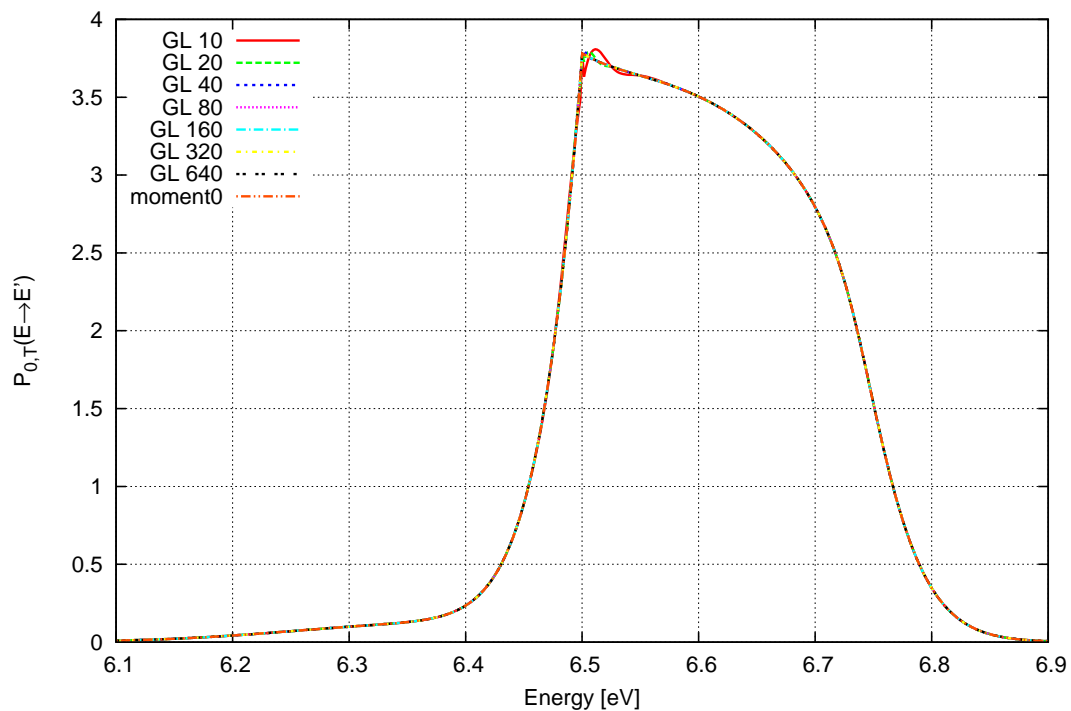
Angular moments near the thermal region

Having established the accuracy of the angular representation, we turn now to the analysis near the thermal region, considering also higher moments. We focus our attention of the case for $E = 6.5$ eV near the first resolved resonance of ^{238}U at 6.67 eV. To provide maximum accuracy, angular moments have been computed using a CPL representation with 10 000 points, and considering 500 points in the range $E' \in [6.1 \text{ eV}, 6.9 \text{ eV}]$. Other calculation parameters, like cutoff, tabulation, and precision of integration in E_r are maintained constant from previous sections. At first, our calculations have been checked against previous published data (Arbanas et al., 2011) obtained with both deterministic and Monte Carlo approach, observing a good agreement.

$P_{0,T}(E \rightarrow E')$ for both constant and ^{238}U cross sections is depicted in Figure 2.13. Once again, we notice that the temperature modifies the 0th moment for



(a) continuous piecewise linear



(b) Gauss-Legendre collocation

Figure 2.12 Convergence analysis of computation of $P_{0,T}(E \rightarrow E')$ for ^{238}U increasing the angular representation with $E = 6.5$ eV at 1000 K.

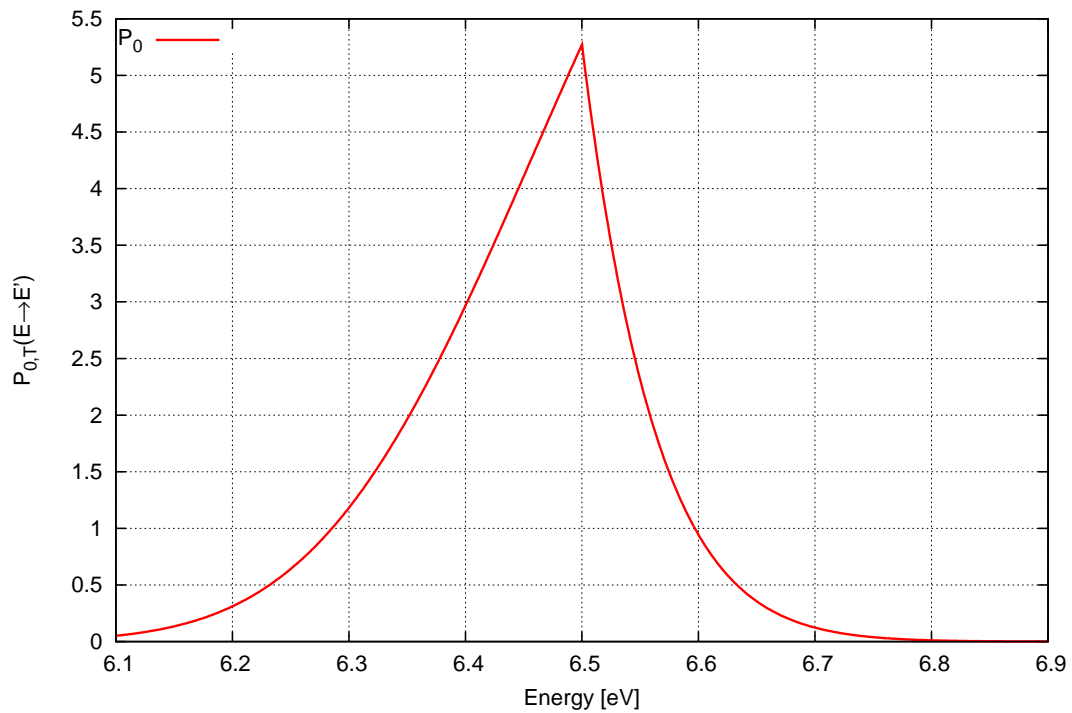
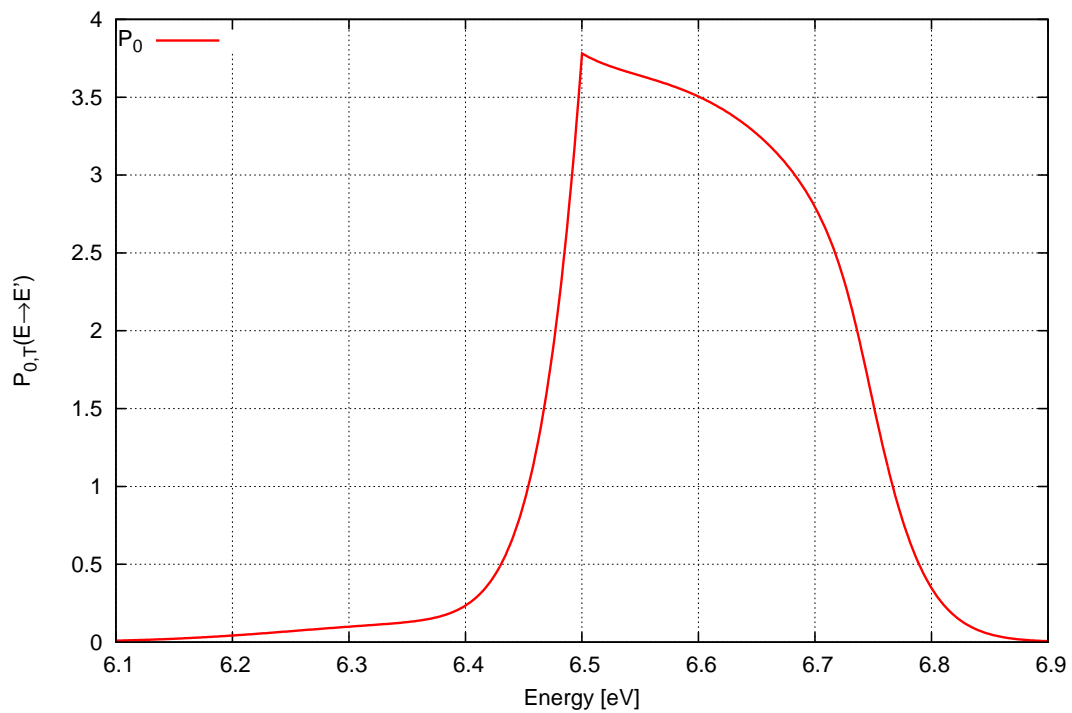
(a) $\sigma = 1$ (b) ^{238}U

Figure 2.13 $P_{0,T}(E \rightarrow E')$ for constant and ^{238}U cross sections at 1000 K for $E = 6.5$ eV. A pronounced up-scattering is found when the Doppler convolution is fully taken into account.

the $\sigma = 1$ case, while maintaining the predominance of down-scattering. When the effect of the resonance is included, the behavior changes abruptly moving increasing sensibly the probability of up-scattering.

We turn now our analysis on higher moments, normalizing the results by $P_{0,T}(E \rightarrow E')$. The results for analytical and real cross section are illustrated in Figure 2.14. We note that, for fixed E , the first normalized angular moment gives the distribution on E' of the deviation angle $\overline{\mu_{\text{LAB}}}$. The comparison of the two plots manifests the asymmetry of the curves with respect to $E' = E$ for ^{238}U , caused by the up-scattering effect.

Behavior around the resonances

A study on the behavior of the moments varying E around the resonance at 6.67 eV of ^{238}U for the 0th, 1st, 2nd, and 3rd angular moment is reported in Figure 2.15, 2.16, 2.17, 2.18. It is illustrated how the presence of the resonance affects the shape of the angular moments. The variation is more pronounced for $E \in [6.5 \text{ eV}, 6.7 \text{ eV}]$ and, in particular, for the first angular moment.

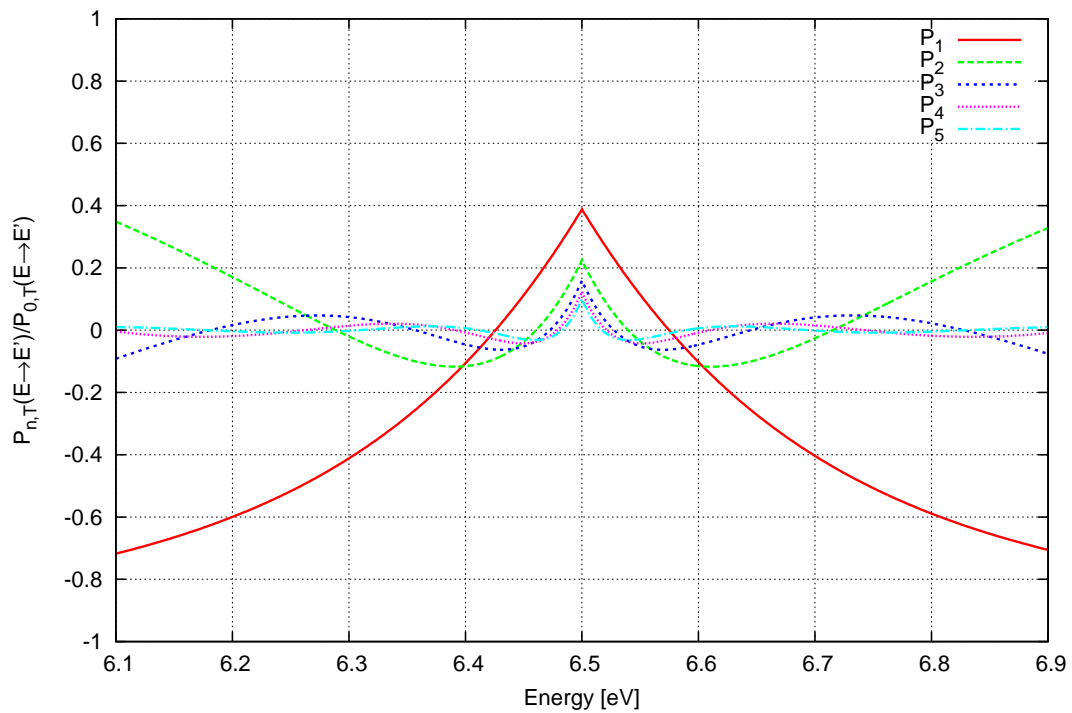
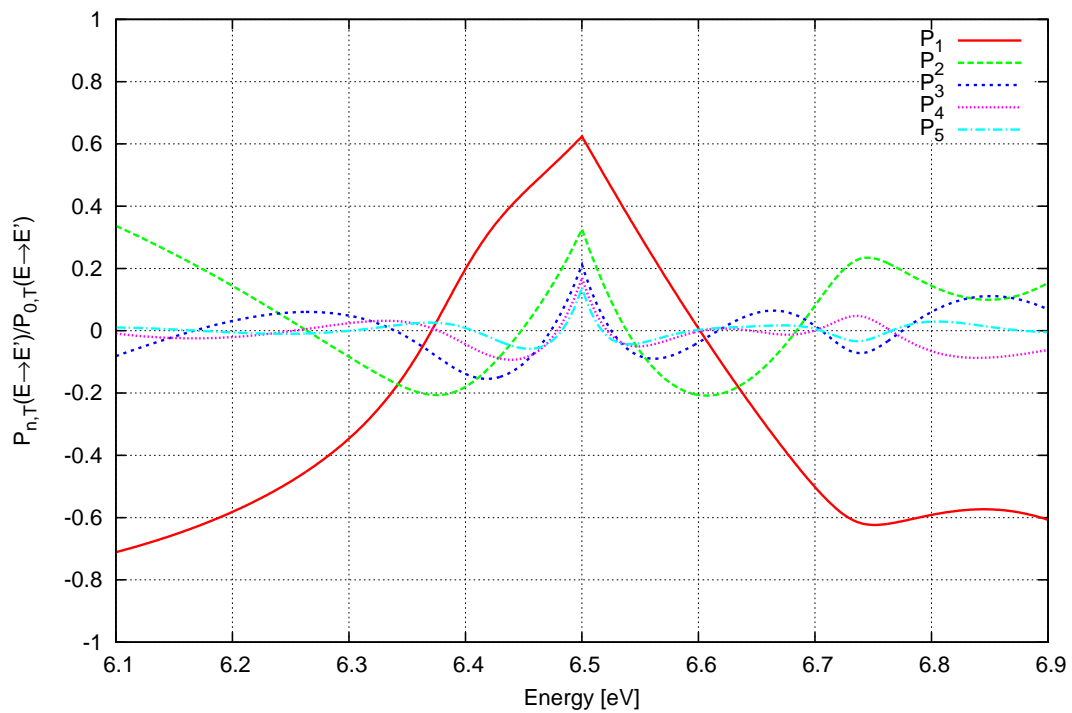
(a) $\sigma = 1$ (b) ^{238}U

Figure 2.14 $P_{n,T}(E \rightarrow E')$ for constant and ^{238}U cross sections at 1000 K for $E = 6.5$ eV. A pronounced up-scattering is found when the Doppler convolution is fully taken into account.

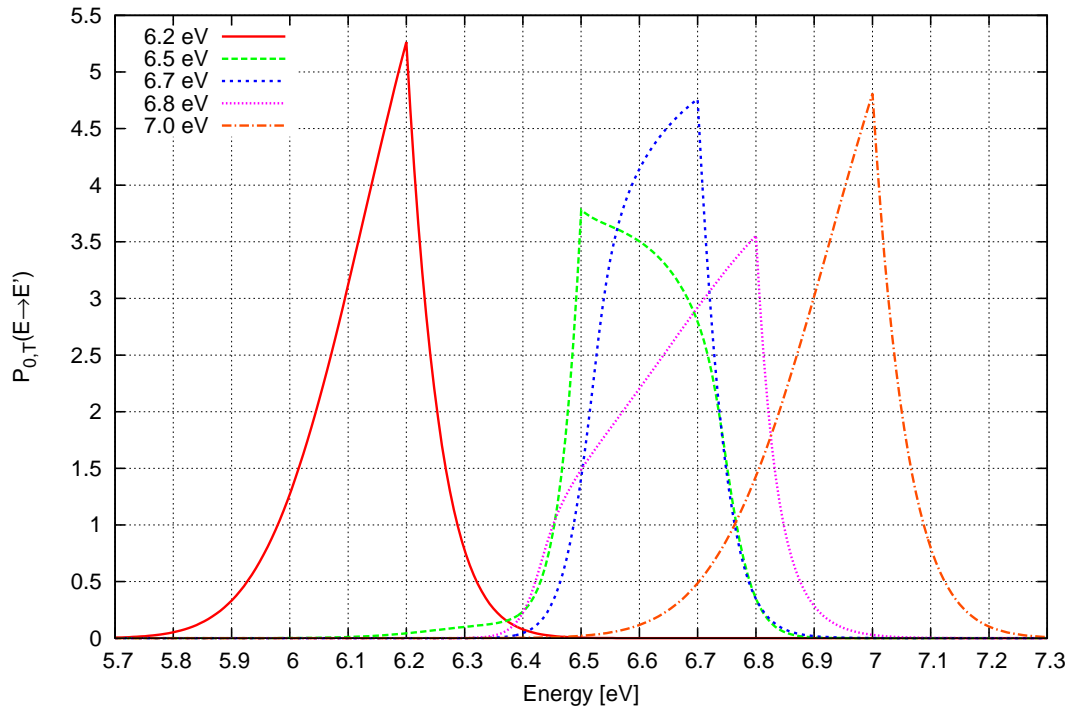


Figure 2.15 $P_{0,T}(E \rightarrow E')$ for ^{238}U for different values of E .

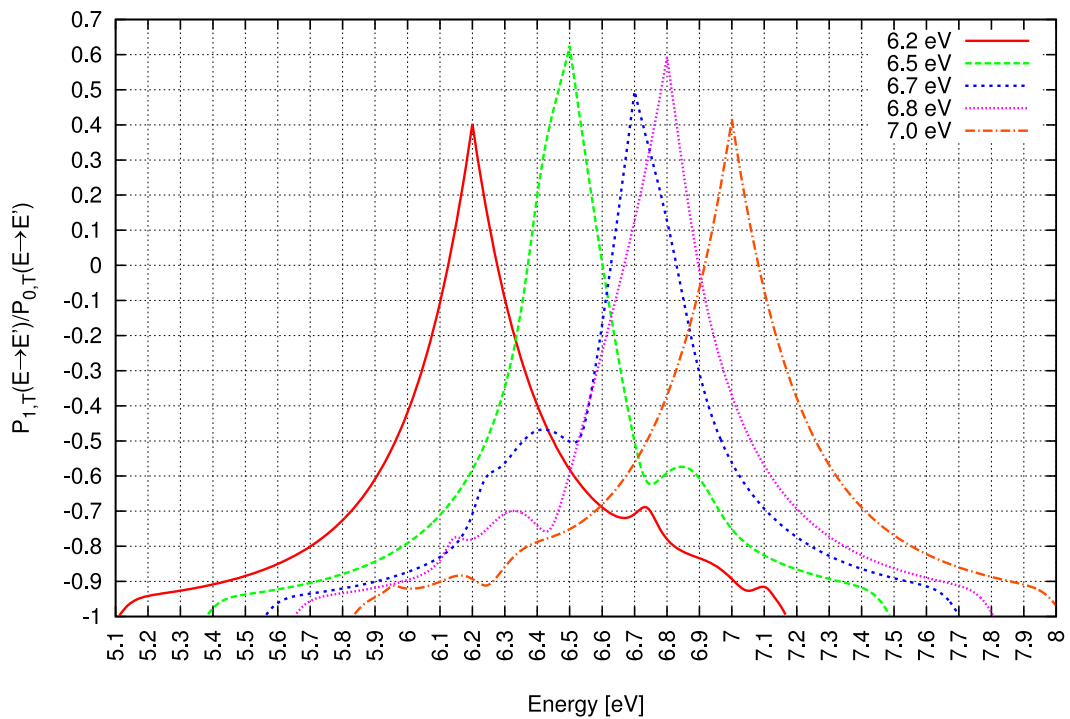


Figure 2.16 $P_{1,T}(E \rightarrow E')/P_{0,T}(E \rightarrow E')$ for ^{238}U for different values of E .

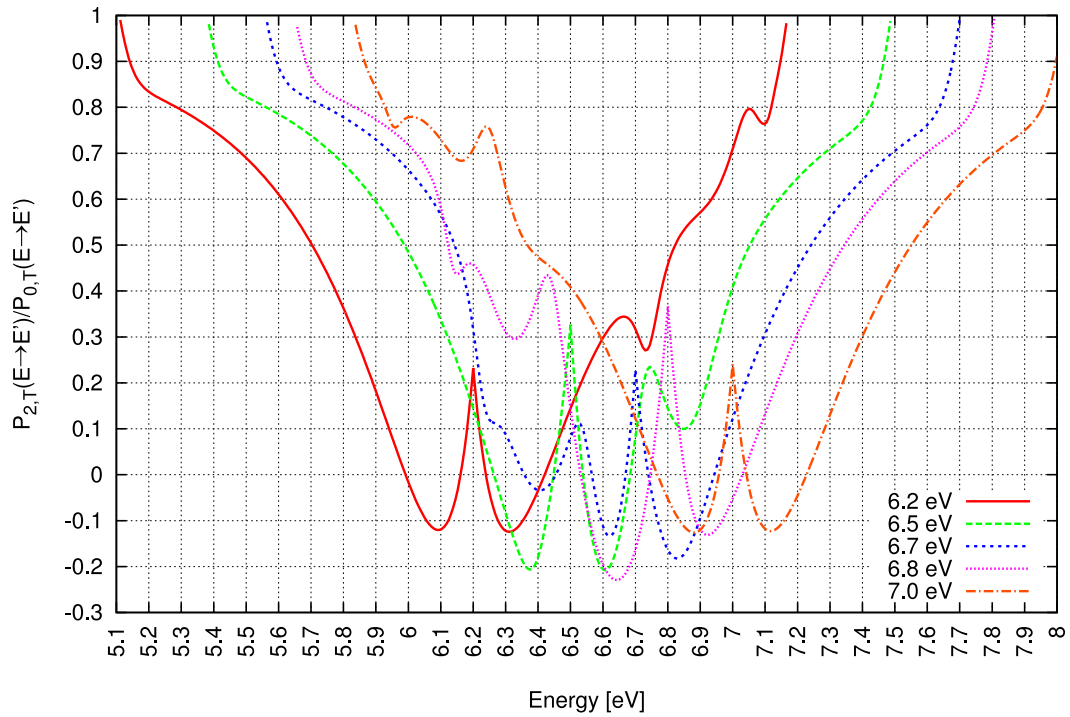


Figure 2.17 $P_{2,T}(E \rightarrow E')/P_{0,T}(E \rightarrow E')$ for ^{238}U for different values of E .

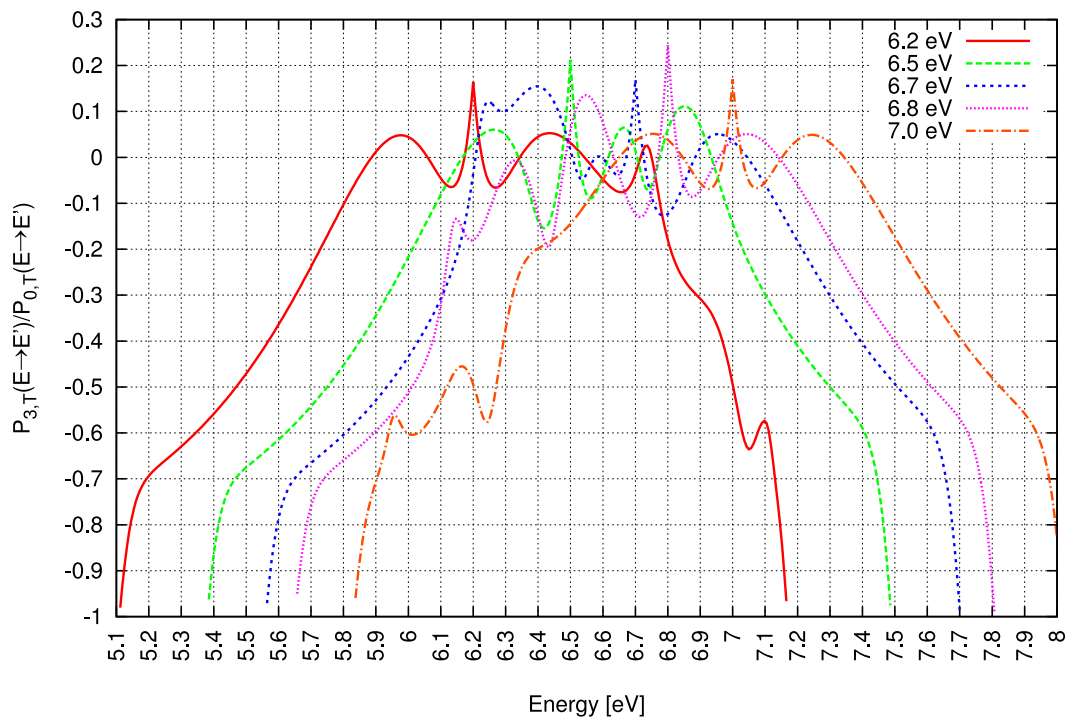


Figure 2.18 $P_{3,T}(E \rightarrow E')/P_{0,T}(E \rightarrow E')$ for ^{238}U for different values of E .

Effects at higher energies

So far we have concentrated our efforts in the study near the resonance at 6.67 eV for ^{238}U . An additional set of simulations have been performed around 9869 eV resonance for $E = 9865$ eV. The angular moments are reported in Figure 2.19.

As we can see, for higher neutron impinging energies the combined influence of the thermal agitation and the resonance is not present, confirming the validity of the asymptotic model in such cases. For these computations at higher neutron impinging energies, the plot manifests a numerical difficulty for $E' \approx \alpha E$ because of sharp variation of the kernel.

2.3.3 Influence of anisotropy of the scattering

Last but not least, we focus on the effects of anisotropy of the scattering law. So far only the isotropic case, for which $P(\mu_{\text{COM}}) = 1/2$, has been studied. From the analysis of the cross section ENDF database, it turns out that for ^{238}U a modest anisotropy begins to appear above 1000 eV. We consider then the effect of the Doppler broadening near the 1474 eV resonance of ^{238}U .

Figure 2.20 shows 0th angular moment for $E = 1473$ eV at 1000 K. The discrepancy with respect to the isotropic case is very slight. Moreover, the angular moment shown does not manifest a tangible contribution of the up-scattering due to the combined presence of the resonance and of the thermal agitation. We conclude that for heavy isotopes, given the lack of anisotropy of the elastic scattering for smaller neutron energies, the Doppler convolution does not affect substantially the results.

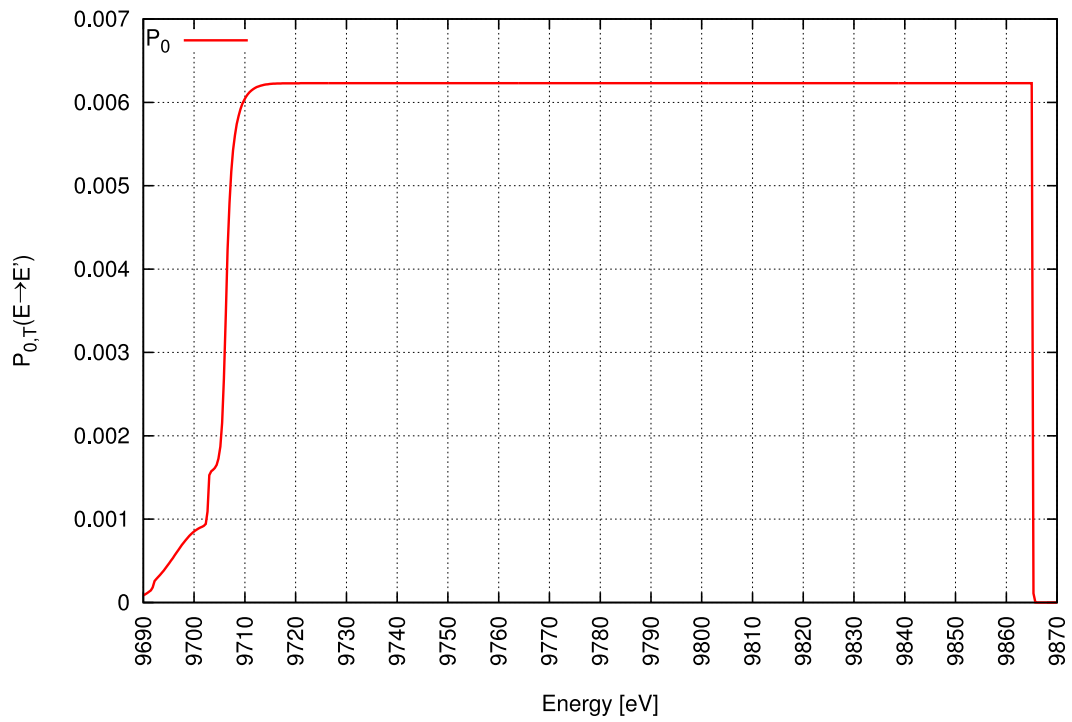
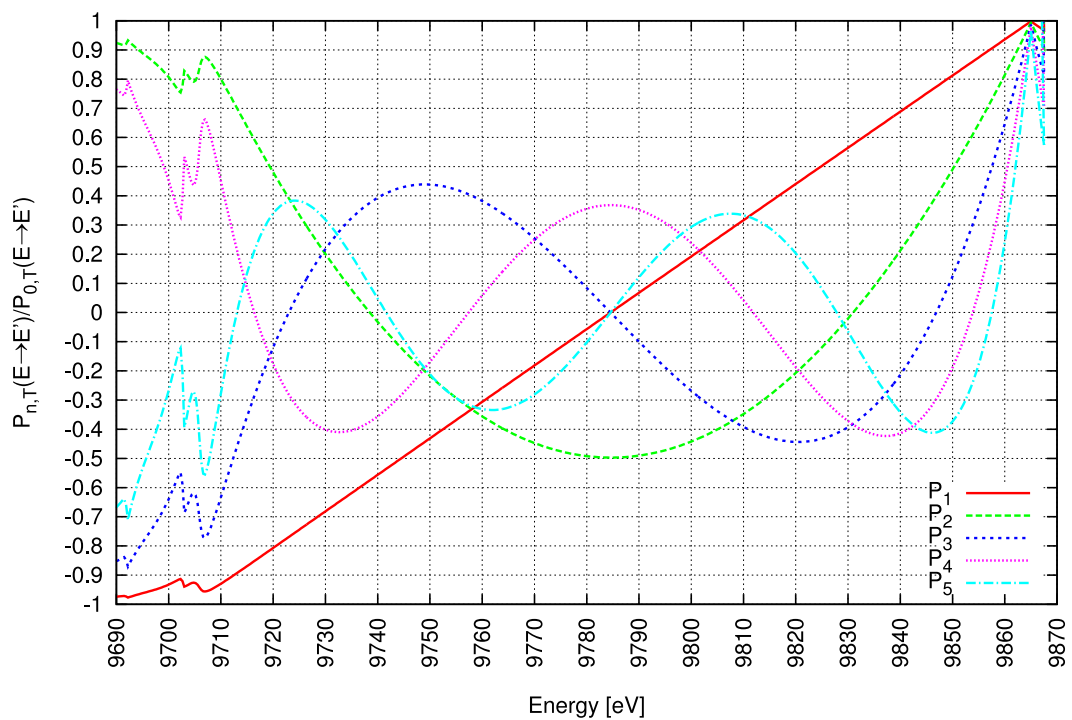
(a) $P_{0,T}(E \rightarrow E')$ (b) $P_{n,T}(E \rightarrow E') / P_{0,T}(E \rightarrow E')$

Figure 2.19 Angular moments for ^{238}U at 1000 K for $E = 9865$ eV. The complete Doppler convolution does not affect the Legendre moments.

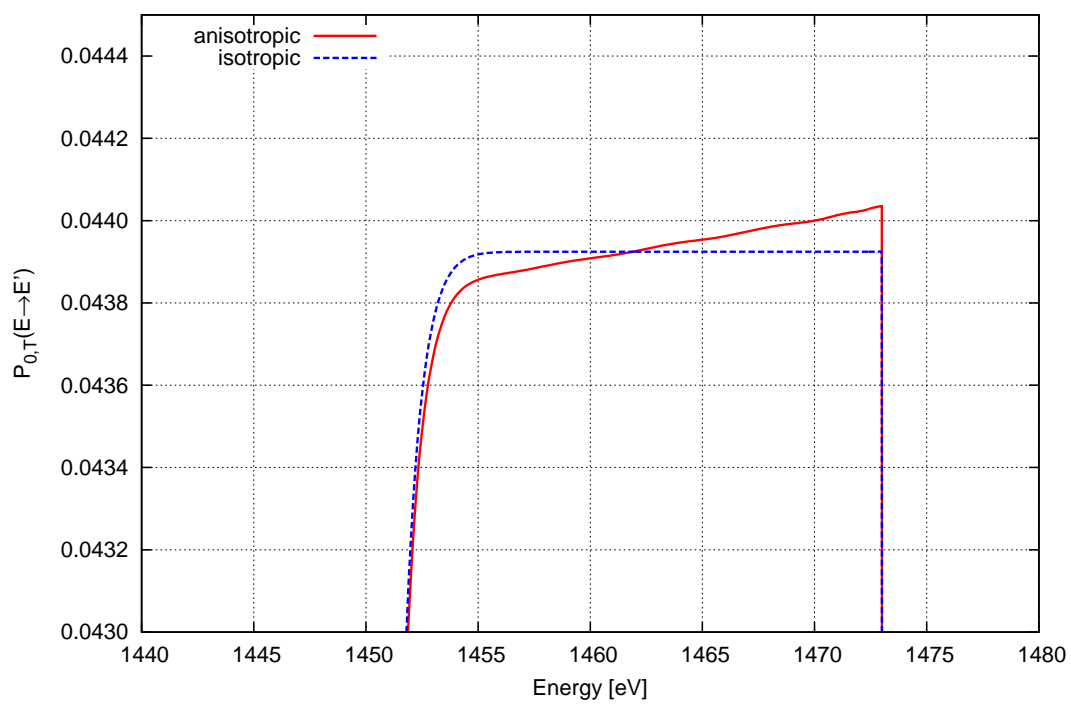


Figure 2.20 $P_{0,T}(E \rightarrow E')$ with and without anisotropy of scattering for ^{238}U near the 1474 eV resonance.

References

- M. Abramowitz and I. A. Stegun (1964). *Handbook of Mathematical Functions with Formulas, Graphs, and Mathematical Tables*. Dover.
- G. Arbanas, M. E. Dunn, N. M. Larson, L. C. Leal, M. L. Williams, B. Becker, and R. Dagan (2011). "Computation of Temperature-dependent Legendre Moments of a Double-Differential Elastic Cross Section". In: *International Conference on Mathematics and Computational Methods Applied to Nuclear Science and Engineering (M&C 2011)*. Rio de Janeiro, Brazil.
- G. I. Bell and S. Glasstone (1970). *Nuclear Reactor Theory*. Van Nostrand Reinhold.
- G. L. Blackshow and R. L. Murray (1967). "Scattering functions for low-energy neutron collisions in a Maxwellian monoatomic gas". In: *Nuclear Science and Engineering* 27, pp. 520–532.
- A. Courcelle and J. Rowlands (2007). "Approximate Model of Neutron Resonant Scattering in a Crystal". arXiv:0709.2767.
- Y. Danon, E. Liu, D. P. Barry, T. I. Ro, and R. Dagan (2009). "Benchmark experiment of neutron resonance scattering models in Monte Carlo codes". In: *International Conference on Mathematics, Computational Methods and Reactor Physics (M&C 2009)*. Saratoga Springs, New York, USA.
- E. Fermi (1934). "Radioattività provocata da bombardamento di neutroni". In: *Ricerca Scientifica* 5.1, p. 283.
- E. Fermi (1936). "Sul moto dei neutroni nelle sostanze idrogenate". In: *Ricerca Scientifica* 7.2, pp. 13–52.
- A. Hébert (2009). *Applied Reactor Physics*. Presses inter Polytechnique.
- A. F. Henry (1975). *Nuclear-reactor analysis*. The MIT Press.
- D. Lee, K. Smith, and J. Rhodes (2008). "The impact of ^{238}U resonance elastic scattering approximations on the thermal reactor Doppler reactivity". In: *International Conference on Reactor Physics, Nuclear Power: A Sustainable Resource (PHYSOR 2008)*. Interlaken, Switzerland.
- R. E. MacFarlane and D. W. Muir (2000). *NJOY99.0 Code System for Producing Point-wise and Multigroup Neutron and Photon Cross Sections from ENDF/B Data*. Tech. rep. PSR-480/NJOY99.00. Los Alamos National Laboratory.
- M. Ouisloumen and R. Sanchez (1991). "A Model for Neutron Scattering Off Heavy Isotopes That Accounts for Thermal Agitation Effects". In: *Nuclear Science and Engineering* 107, pp. 189–200.
- P. Reuss (2008). *Neutron Physics*. EDP Sciences.
- W. Rothenstein (1996). "Neutron scattering kernels in pronounced resonances for stochastic Doppler effect calculations". In: *Annals of Nuclear Energy* 23.4–5, pp. 441–458. DOI: 10.1016/0306-4549(95)00109-3.

- W. Rothenstein (2004). "Proof of the formula for the ideal gas scattering kernel for nuclides with strongly energy dependent scattering cross section". In: *Annals of Nuclear Energy* 31, pp. 9–23.
- W. Rothenstein and R. Dagan (1998). "Ideal gas scattering kernel for energy dependent cross-sections". In: *Annals of Nuclear Energy* 25.4–5, pp. 209–222. doi: 10.1016/S0306-4549(97)00063-7.
- R. Sanchez (2013). *Personal communication*.
- R. Sanchez, C. Hewko, and S. Santandrea (2013). "Numerical Computation of Doppler-Broadening in the Resonance Domain". In: *International Conference on Mathematics and Computational Methods Applied to Nuclear Science and Engineering (M&C 2013)*. Sun Valley, Idaho, USA.
- M. M. R. Williams (1966). *The slowing down and thermalization of neutrons*. North-Holland.
- A. Zoia, E. Brun, C. Jouanne, and F. Malvagi (2013). "Doppler broadening of neutron elastic scattering kernel in TRIPOLI-4". In: *Annals of Nuclear Energy* 54, pp. 218–226.

Chapter 3

Radiative transfer modeling for remote sensing of the cryosphere

The problem of describing the light propagation through a medium can be addressed using both wave propagation and a particle approach. The former requires the solution of the Maxwell equations through the medium, which in turn depends on the complete representation of the electromagnetic scattering and all the secondary waves generated by each oscillating charge, taking into account their phase differences. This approach is very demanding given the enormously large number of elementary charges in each micrometer-sized particle. If the medium can be considered as a collection of macroscopic scatterers, the problem can be addressed using the particle approach employing the radiative transfer equation. This mathematical formulation presents the same form as the neutron transport equation considered in Chapter 1.

There are basically two different strategies to formulate the radiative transfer equation: the vector and the scalar models. To take in account all the polarization effects it is necessary to employ the vector formulation, that relies on the determination of all the four components of the Stokes's vector (I , Q , U , V). The scalar model, instead, assumes that the photons never modify the average polarization state and leads to the determination of only the first component, I (intensity). This approximation is not necessarily good for Rayleigh scattering (which, as a matter of fact, modify the polarization state of the incident beam of light), but appears to be sufficiently accurate for particles greater than or equal to the wavelength considered (Mishchenko, Dlugach, et al., 1999). For the purposes of our work we use the scalar model.

The scattering parameters to be included in the linear transport formulation of the radiative transfer problem are usually taken from measures of the complex index of refraction of each medium or from solution of the Maxwell equations in

simpler geometries. A classical model employed in this field is the Lorenz-Mie scattering theory (1908), that provides the mathematical rigorous solution of the electromagnetic equations for spherical particles randomly distributed in space.

The ability to solve the photon field in a medium is of paramount importance in remote sensing using multispectral sensors, and in particular in studies connected to space exploration, investigations into atmospheric phenomena, and glacier mapping. Regarding the latter, at-sensor radiance depends on glacier surface material composition and intermixture of materials, solar and sensor geometry, and surface topography. As a consequence, interpreting the measured electromagnetic signal requires establishing a proper modeling of the properties of the observed surface and the light propagation.

Since the force of gravitation impose a density stratification, the medium properties tend to vary primarily in the vertical direction (Thomas and Stammes, 1999). In addition, in many remote sensing applications the surface dimension that correspond to every pixel detected is big enough to consider every position uniform horizontally and independent from the neighbor points. This is particularly true when the main source of illumination (i.e. the Sun) is high enough in the horizon that the non-flat shape of the planet is unimportant. For this reason the radiative transfer problem to be solved is usually modeled in slab geometry. Even with this simplification, the radiative transfer equation (RTE) presents significant numerical challenges for its solution, since its integro-differential form.

In this chapter the problem of determining the radiation field within, at the surface of, and above glaciers and debris fields is analyzed by means of linear transport theory. Here an extended multilayered version of the ADO (Analytical Discrete Ordinates) method is applied to solve the radiative transfer equation. First proposed by Chandrasekhar (1960), it has been revised recently by Siewert (2000), who devised a compact solution scheme in a matrix formulation, transforming the problem of finding the separation constants as an eigenvalue problem, instead of the original zeros roots finding. It was confirmed to lead to extremely accurate results, with reasonably fast computation time (Previti et al., 2011).

Modeling of the optical properties of single material particles (ice or snow, lithic debris, and carbon soot) is discussed in the framework of glaciers observations, including common methods employed to determine single-scattering albedo and scattering-phase function, for both single-type particles and mixtures

Examples of calculations of the Bidirectional Reflectance Function (BRF) and the spectral albedo are included to show how remotely measurable quantities depend on morphological and mineralogical properties of the medium, i.e. BRF for mixtures of snow and debris, and spectral albedo variation for snow and

carbon soot with varying grain size and particle concentration.¹

3.1 Fundamentals of radiative transfer

In radiative transfer theory, interference and diffraction of light are usually not considered and the index of refraction across the transport medium of interest is assumed constant. Using these hypothesis, it is possible to derive the classic radiative transfer equation as photon balance in the phase space. In this section shall proceed in the definition of all the quantities involved in such balance, discussing the approximations employed in remote sensing studies.

3.1.1 Particle and wave models for photon transport

Complete and detailed description of light field through matter requires the study of propagation of the electromagnetic radiation. A parallel monochromatic beam of light in vacuum proceeds without any change in intensity or polarization. If light encounters a small particle two main different phenomena can take place: conversion of the energy of the beam into heat (*absorption*), and diversion of the beam of a given angle (*scattering*). Also, the particle itself can emit radiation if its absolute temperature is above zero (*thermal emission*).

Let's consider the wave approach to light propagation: a beam of light is an oscillating plane electromagnetic wave and the particle is an aggregation of many electric charges. The solution of the electromagnetic field in a dense medium can be therefore extremely heavy in term of computation burden, since one needs to take into account all the secondary waves generated by each oscillating charge. This is impracticable even with the aid of modern computers (Mishchenko, Travis, et al., 2002).

Fortunately, for typical engineering and physical problems it is possible to consider a large collection of charges as a macroscopic body with a given refractive index. One often should consider situations where light is scattered by a large random group of particles comprising the medium, but fortunately these particle can be modeled as independent scatterers. If the particles are sufficiently small, the secondary waves generated in the scattering processes are negligible compared to

¹This work is a part of GLIMS project (Global Land Ice Measurements from Space, <http://www.glims.org/>), in cooperation with The University of Arizona, USA. The chapter presents a completely revisited version of the following publication, with extended additions in historical background and numerical methods, and with only the results of the author of this dissertation. R. Furfaro, A. Previti, P. Picca, J. S. Kargel, M. P. Bishop, Radiative Transfer Modelling in the Cryosphere, in: Global Land Ice Measurements from Space, J. S. Kargel, G. J. Leonard, M. P. Bishop, A. Kääb, and B. Raup (Editors), Praxis-Springer (Publishers), Heidelberg (2013), ISBN: 978-3-540-79817-0.

the external field, and the total scattered field can be approximated as a sum of the fields generated by every individual particles (*single scattering approximation*).

When the medium contains a very large number of particles, like an ordinary planet surface or a cloud atmosphere, it is needed to explicitly take into account the multiply scattered radiation. This approach yields to the formulation of the radiative transfer equation, which is a representation of the radiation field by means of statistical mechanics and linear transport theory. The hypothesis under which this model can be used are:

- far-field approximation: the propagation of the light beams occurs in a plane perpendicular to the oscillation of its associated electric field, the propagation of the scattered wave is away from the particle, and the amplitude of the scattered field decreases inversely with distance from the particle;
- the electromagnetic field associated with light propagation is not too strong and Kerr effect, i.e. perturbation of the refractive index of the medium, does not take place;
- the collision of each photon consists always of a single scattering event, without any collective phenomenon.

Also, we explicitly exclude Raman and Brillouin scattering and fluorescence, i.e. electromagnetic scattering occurs only without change of frequency.

Thus, the analysis of light propagation through media comprises three steps (Mishchenko, Travis, et al., 2002):

1. computation of the scattering and absorption properties of an individual particle using Maxwell equations under far-field approximation;
2. calculation of scattering and absorption of a small volume element containing a tenuous particle collection by using the single-scattering approximation;
3. solution of the multiple scattering problem using the radiative transfer equation.

Regarding the first point, Lorenz-Mie scattering theory (1908) stays prominent as a rigorous mathematical solution of the electromagnetic equation in the case of scattering by spherical particles. A generalization of the model to non-spherical aggregates is known as *T-matrix* theory.

3.1.2 Transport modeling for remote sensing

In radiative transfer theory, the medium is assumed to be a collection of scattering and absorbing centers uniformly distributed in a differential volume. The photons'

behavior is determined by the probability of scattering and absorption within the host medium. If the conservation of photons is applied in the six-dimensional phase-space (i.e. position and velocity), the following equation is utilized:

$$\frac{1}{c} \frac{\partial I_\lambda(\mathbf{r}, \boldsymbol{\Omega}, t)}{\partial t} + \boldsymbol{\Omega} \cdot \nabla I_\lambda(\mathbf{r}, \boldsymbol{\Omega}, t) + \Sigma_\lambda(\mathbf{r}) I_\lambda(\mathbf{r}, \boldsymbol{\Omega}, t) = \frac{1}{4\pi} \int_{4\pi} d\boldsymbol{\Omega}' \Sigma_{\lambda,s}(\mathbf{r}, \boldsymbol{\Omega}' \rightarrow \boldsymbol{\Omega}) I_\lambda(\mathbf{r}, \boldsymbol{\Omega}', t) + \Sigma_{\lambda,a}(\mathbf{r}) B_\lambda(T). \quad (3.1)$$

where $I_\lambda(\mathbf{r}, \boldsymbol{\Omega}, t)$ is the spectral radiance [$\text{W m}^{-2} \text{sr}^{-1} \text{s}^{-1}$] of photons at the location \mathbf{r} traveling in the direction $\boldsymbol{\Omega} = (\mu, \phi)$ within the cone $d\boldsymbol{\Omega}'$. The spectral radiance, or intensity, is the physical quantity that describes the light distribution within, entering, and exiting the host medium, and it is the unknown of the radiative transfer problem. The subscript λ underlines that spectral nature of the intensity, i.e. the fact that this equation is valid for every wavelength of interest.

The first term in (3.1) is the temporal variation of the spectral radiance, where c is the speed of light. The second term, summed to the first one, represents the net energy loss of photons streaming out of the phase space. This is balanced by the energy loss due to the scattering and absorption (third term left-hand side), the inscattering of photons in the phase space (first term right-hand side), and the thermal-induced emission of photons (second term right-hand side).

The participating medium is described by the absorption and scattering coefficients: $\Sigma_\lambda(\mathbf{r})$ is the total interaction coefficient [m^{-1}], defined as the sum of the absorption ($\Sigma_{\lambda,a}(\mathbf{r})$) and scattering coefficient ($\Sigma_{\lambda,s}(\mathbf{r})$). More specifically, $\Sigma_{\lambda,s}(\mathbf{r}, \boldsymbol{\Omega}' \rightarrow \boldsymbol{\Omega})$ is the differential scattering coefficient (also called differential scattering cross section or inscattering coefficient), that describes the probability that photons traveling in the $\boldsymbol{\Omega}'$ direction are scattered in the $d\boldsymbol{\Omega}$ about $\boldsymbol{\Omega}$ direction. In conventional radiative transfer theory, like in neutron transport applications for reactors, the host medium is assumed to be *rotationally invariant*, i.e. the differential scattering coefficient depends only on the angle between $\boldsymbol{\Omega}'$ and $d\boldsymbol{\Omega}$, called deviation angle $\Theta = \boldsymbol{\Omega}' \cdot \boldsymbol{\Omega}$. There are situations where this hypothesis is precluded, like in photon transport in canopies, and the complete angular representation of the scattering term is necessary (Furfaro and Ganapol, 2007). Finally, $\Sigma_{\lambda,a}(\mathbf{r}) B_\lambda(T)$ depicts the thermal emission of photons, as a function of the Planck's law of radiation $B_\lambda(T)$ for a blackbody at temperature T and under the assumptions of the Kirchhoff's law. The latter states that in thermodynamical equilibrium the spectral emissivity, which is the ratio between the energy emitted by a medium of a given temperature T and the energy emitted by a blackbody at the same temperature and frequency, is equal to the spectral absorptivity $\Sigma_{\lambda,a}$.

To complete the mathematical description of the balance of photons interacting with the host medium, proper boundary conditions that account for the radiative

flux of photons entering the medium must be provided. Since for the case of snow, ice, and debris scattering phenomena do not change the energy of the photons, (3.1) can be solved independently at each wavelength to determine the radiative regime.

Equation (3.1) does not have a general analytical closed-form solution, given its integro-differential form. Although it is the basis of the physical models used in remote sensing, several assumptions should be enforced to derive a more manageable form, allowing fast and accurate numerical solutions. The first immediate simplification comes from the observation that the $1/c$ term factoring the time-derivative of $I_\lambda(\mathbf{r}, \mathbf{\Omega}, t)$ is smaller than the intensity flux time-rate (Davis and Knyazikhin, 2005). The latter implies that a steady-state is reached almost instantaneously. Indeed, radiative transfer in passive remote sensing applications is generally modeled as a stationary phenomenon: time-dependent radiative transfer problems are considered only when modeling the response of the surface to active pulsed illumination by remote-sensing instruments (e.g. LiDAR).

The dimensionality of the complete radiative transfer problem described by (3.1) make it extremely difficult to be solved in a fast and accurate way. Still, simplified geometries can be used considering the the actual material and particle-size arrangements typically found in remote sensing applications. Since the force gravitation imposes a density stratification and the surface dimension that corresponds to every pixel detected by sensors is big enough, we consider a 1D approach, where the medium varies only in the vertical direction and is infinite in the horizontal one. For example, ASTER² and MODIS³ pixel resolution are 15m and 250m. Therefore for glaciers environments the major glaciological features would be fully resolved and a 1D configuration is sufficient, where every pixel is independent from neighbor pixels⁴. Also, so long as photons do not penetrate through grains far enough to interact with different types of minerals, the reflectance signature of mixtures of snow, air, and debris is simply the area-averaged reflectance spectra of the mineral components making up the surface.

The spectral radiance depends then spatially only on the optical depth defined as:

$$\tau = \int_0^x dx' \Sigma_\lambda(x'). \quad (3.2)$$

At the same time, the dependence on space and deviation of the differential scat-

²Advanced Spaceborne Thermal Emission and Reflection Radiometer. It is a Japanese sensor launched into Earth orbit for remote sensing purpose by NASA in 1999.

³Moderate-Resolution Imaging Spectroradiometer. Launched by NASA in 1999, it is designed to provide measurements in large-scale global dynamics including changes in Earth's environment.

⁴Independent Pixel Approximation (IPA)

tering is usually represented as:

$$\frac{\Sigma_{\lambda,s}(\tau, \mathbf{\Omega}' \cdot \mathbf{\Omega})}{\Sigma_{\lambda}(\tau)} = \omega_{\lambda}(\tau) p_{\lambda}(\tau, \cos \Theta), \quad (3.3)$$

where $\omega_{\lambda}(\tau)$ and $p_{\lambda}(\tau, \cos \Theta)$ are the single-scattering albedo and the scattering-phase function, respectively. Under these assumptions radiant intensity depends only on one spatial and two angular variables. This is different compared to neutron transport, where usually one needs the full 3D spatial representation, but only one angle is considered.

3.1.3 Mathematical setting for layered media

The linear transport equation governing the radiative regime in a vertical heterogeneous medium writes (Chandrasekhar, 1960):

$$\mu \frac{\partial I_{\lambda}(\tau, \mu, \phi)}{\partial \tau} + I_{\lambda}(\tau, \mu, \phi) = \frac{\omega_{\lambda}(\tau)}{4\pi} \int_0^{2\pi} d\phi' \int_{-1}^1 d\mu' p(\tau, \cos \Theta) I_{\lambda}(\tau, \mu', \phi') + [1 - \omega_{\lambda}(\tau)] B_{\lambda}(T(\tau)). \quad (3.4)$$

For cryosphere studies, given the typical wavelengths analyzed and the media temperature, the thermal source $[1 - \omega_{\lambda}(\tau)] B_{\lambda}(T(\tau))$ is usually neglected.

Boundary conditions are necessary to fully specify the radiance field $I_{\lambda}(\tau, \mu, \phi)$. Even though the general conditions for a linear transport problem include both direct and diffusive illumination, specular and diffuse reflectance, and surface thermal emission, the most relevant contributions at the upper boundary for radiative transfer problems are the first two terms, that take into account the effect of the Sun illumination. In radiative transfer problems with remote applications, the medium is generally optically thick and hence vacuum boundary conditions are considered at the bottom surface.

Therefore, the boundary conditions to be coupled with (3.4) are:

$$I_{\lambda}(0, +\mu, \phi) = f_0 \pi \delta(\mu - \mu_0) \delta(\phi - \phi_0) + f(\mu), \quad (3.5a)$$

$$I_{\lambda}(\tau_0, -\mu, \phi) = 0. \quad (3.5b)$$

where τ_0 is the total optical length of the medium, μ_0 (azimuthal angle) and ϕ_0 (polar angle) determine the inclination of the solar beam of total flux $f_0 \pi$, and the diffusive illumination due to the surrounding atmosphere is expressed as a function of μ . The direction of the τ -axis is considered positive in the downward direction and thus μ is negative for upward angles.

The vertical heterogeneity of the system to be analyzed can be represented assuming a multi-layer configuration where the medium is subdivided in multiple homogeneous layers, each having different optical properties. For each layer, the single scattering albedo and the scattering phase function are defined either for a single material or for a mixture, respectively as $\omega_\lambda^{(s)}$ and $p_\lambda^{(s)}(\cos \Theta)$, for $s = 1, \dots, N$. In every layer s , the radiative transfer equation is:

$$\mu \frac{\partial}{\partial \tau} I_\lambda^{(s)}(\tau, \mu, \phi) + I_\lambda^{(s)}(\tau, \mu, \phi) = \frac{\omega_\lambda^{(s)}}{4\pi} \int_0^{2\pi} d\phi' \int_{-1}^1 d\mu' p_\lambda^{(s)}(\cos \Theta) I_\lambda^{(s)}(\tau, \mu', \phi'), \quad (3.6)$$

where τ has to be considered in a local coordinate system (i.e. the s -th layer starts from $0^{(s)}$ and ends with $\tau_0^{(s)}$).

Moreover, the continuity of the intensity at each interface provides the boundary conditions in each layer:

$$I_\lambda^{(s)}(0^{(s)}, +\mu, \phi) = I_\lambda^{(s-1)}(\tau_0^{(s-1)}, +\mu, \phi), \quad (3.7a)$$

$$I_\lambda^{(s)}(\tau_0^{(s)}, -\mu, \phi) = I_\lambda^{(s+1)}(0^{(s+1)}, -\mu, \phi). \quad (3.7b)$$

In such configurations the bottom layer is generally assumed to be optically thick, i.e. semi-infinite.

3.1.4 Quantities of interest for remote sensing

Quantitative characterization of surface properties using remotely sensed data requires the definition of a functional relationship between surface properties and surface radiance. So far, we have considered only the *spectral radiance* or *intensity* $I_\lambda(\mathbf{r}, \mathbf{\Omega}, t)$, that is the energy transported across an element of area dA , whose orientation is defined by its unit normal \mathbf{n} , and in directions confined to an element of solid angle $d\mathbf{\Omega}$. The total energy traveling across an element of area dA , for every incident and outgoing direction is called *spectral irradiance* or *flux* (Davis and Knyazikhin, 2005). It can be calculated from integration of the intensity, i.e.:

$$F_\lambda(\mathbf{r}, t) = \int_{4\pi} d\mathbf{\Omega}' |\mathbf{n} \cdot \mathbf{\Omega}'| I_\lambda(\mathbf{r}, \mathbf{\Omega}', t). \quad (3.8)$$

The related half-range irradiance are obtained integrating only in one hemisphere, say $\mathbf{n} \cdot \mathbf{\Omega}' > 0$ and $\mathbf{n} \cdot \mathbf{\Omega}' < 0$. Note that the flux/irradiance is the first moment of the intensity/radiance.

When a flat surface emits isotropically in all the directions, the intensity does not depend on the angle considered, say $I_\lambda(\mathbf{\Omega}) = I_\lambda = \text{constant}$. This is the

so-called *Lambertian* surface. Using a system of polar coordinates with the z -axis in the direction of the outward normal to dA , we can calculate the hemispherical irradiance in a straightforward way, say:

$$F_L = \int_0^{2\pi} d\phi' \int_0^{\pi/2} d\theta' I_L \cos \theta' \sin \theta' = \pi I_L \quad (3.9)$$

where the subscript L highlights the fact that we are speaking about a Lambertian surface. Of course, the net flux is equal to zero.

In the 1D, two-angle radiative transfer theory the two hemispherical photon fluxes are conventionally defined as:

$$q_+ = \int_0^{2\pi} d\phi' \int_0^{+1} d\mu' I(0, \mu', \phi') \quad (3.10a)$$

$$q_- = \int_0^{2\pi} d\phi' \int_{-1}^0 d\mu' I(0, \mu', \phi'). \quad (3.10b)$$

Making use of these definitions, useful quantities can be obtained. For the sake of clarity and simplicity of the notation, we shall suppress all the dependencies about wavelength. The *transmittance* is defined as the ratio between the outgoing flux at the lower boundary and the incoming irradiance at the upper one:

$$T_n = \frac{F^+(\tau_0)}{F^+(0)}, \quad (3.11)$$

where τ_0 is the thickness of the medium.

The *reflectance* or *spectral albedo*, instead, is the ratio between the outgoing and incoming flux at the upper boundary:

$$R_f = \frac{F^-(0)}{F^+(0)}. \quad (3.12)$$

For example, for a 1D system illuminated by a solar beam of flux $f_0\pi$, the spectral albedo is $q_-/(f_0\pi)$.

Full dependence on angular direction of the reflected intensity is obtained through the Bidirectional Reflectance Distribution Function (BRDF). It is the ratio of reflected radiance per unit of incoming irradiance, and it is dependent on both the incoming and outgoing angle considered (Davis and Knyazikhin, 2005):

$$\text{BRDF}((\mu_0, \phi_0) \rightarrow (\mu, \phi)) = \frac{I(0, -\mu, \phi)}{q_+}, \quad [\text{sr}^{-1}] \quad (3.13)$$

where (μ_0, ϕ_0) is the angle of the collimated incident beam, and (μ, ϕ) the angle of reflection.

Another popular quantity is the *Bidirectional Reflectance Factor (BRF)*, that is closely correlated to the *BDRF*. The nadir radiance, propagating vertically upward, is $I(\Omega = \mathbf{n})$. If we use the Lambertian hypothesis, we can predict the outgoing flux and, from there, the apparent albedo of the medium:

$$\text{BRF} = \frac{\pi I(\Omega = \mathbf{n})}{q_+}. \quad (3.14)$$

In case of collimated incoming beam, (3.14) becomes:

$$\text{BRF} = \frac{\pi I(\Omega = \mathbf{n})}{q_+} = \pi \text{BDRF} \quad (3.15)$$

Note that the BRF, unlike the original out/in flux ratio, is not bounded between 0 and 1 (Davis and Knyazikhin, 2005).

The Bidirectional Reflectance Distribution Function (BRDF) and/or the closely related Bidirectional Reflectance Factor (BRF), as well as the spectral albedo, are the typical parameters employed to describe the surface reflectance given irradiance, surface morphology and composition variations.

3.2 Radiative transfer modeling for glaciers surfaces monitoring

Remote sensing of the Earth's cryosphere is an active research area, since glaciological processes are closely linked to atmospheric, hydrospheric, and lithospheric processes (Bush, 2000). Global understanding of cryospheric processes involves analysis of glacier dynamics since they are affected by and can influence climate change (Maisch, 2000). Consequently, characterization and estimation of glacier surface properties, such as ice grain-size, rock debris cover, and surface water distribution, becomes critical to advancing our understanding of glacier-climate relationships and glacier fluctuations (Bishop et al., 2004; Kargel et al., 2005). These information can be obtained by orbiting platforms, that measure the magnitude of reflected/emitted surface radiance in the visible, infrared, and thermal portions of the spectrum. Satellite imagery provide global and continuous coverage of vast portions of Earth's surface, and can thus be processed to estimate surface properties.

Glacier surfaces are generally comprised of a variety of materials and exhibit a complex reflectance distribution depending on the spatial structure of the surface constituents. Spatial and temporal variations in debris cover and intimate or areal mixtures between coarse-grained glacier ice, snow, liquid water, vegetation, and

rock debris contribute to highly variable reflectance as observed by in-situ and platform-based sensors (Kargel et al., 2005; Raup et al., 2007).

Modeling plays a central role in investigating the relationships between surface mixtures and reflectance, and can assist glacier mapping and characterization. BRDF and BRF modeling are important functional components of scientific inquiry because they help bridge the gap between investigative findings and field-based and remote observations. For example, Mishchenko, Dlugach, et al. (1999) modeled the directional reflectance pattern and its effect on the albedo for four types of soils, each characterized by a different index of refraction. The BRF patterns were generated for snow using three different scattering phase functions (hexagonal ice, fractal ice and spherical ice) to examine the effect of ice morphology on reflected radiation.

The radiative transfer equation is the framework and physical basis of for modeling the directional reflectance measured by orbiting sensors as a function of the surface properties (e.g. composition, grain size) and the solar/sensor/medium geometry. The photon field depends on the scattering properties of the system considered, and in particular on the single-particle optical behavior. As seen in previous sections, absorption and scattering efficiencies are related to the probability that a photon will be scattered or absorbed by a single particle of defined shape and size. Scattering and absorption processes are accounted for via two optical-property parameters single-scattering albedo ω_λ and scattering phase function $p_\lambda(\cos \Theta)$.

The single-scattering albedo is a scalar parameter ranging between 0 and 1, representing the ratio between scattering and total extinction. The phase function, instead, is customarily described using a series expansion, in which the coefficients represent the projection of $p_\lambda(\cos \Theta)$ on a basis of Legendre polynomials:

$$p(\cos \Theta) = \sum_{l=1}^L \beta_l P_l(\cos \Theta). \quad (3.16)$$

Generally, snow, ice, and soil exhibit a strongly forward-peaked scattering function, i.e. relatively large single particles tend to scatter radiation primarily in the forward direction. The latter implies that a very large numbers of coefficients (order of hundreds) is required to accurately characterize the single-particle phase function. The asymmetry parameter g , which is the defined as the cosine of the average of deviation, may be conveniently employed to reduce the number of parameters required to described the optical properties of a single particle. Under this scheme, the Henyey-Greenstein model (Henyey and Greenstein, 1941)

is widely employed to approximate the phase function for the particles of interest:

$$p(\cos \Theta) = \frac{1 - g^2}{(1 - 2g \cos \Theta + g^2)^{3/2}}, \quad g \in [-1, +1], \quad (3.17)$$

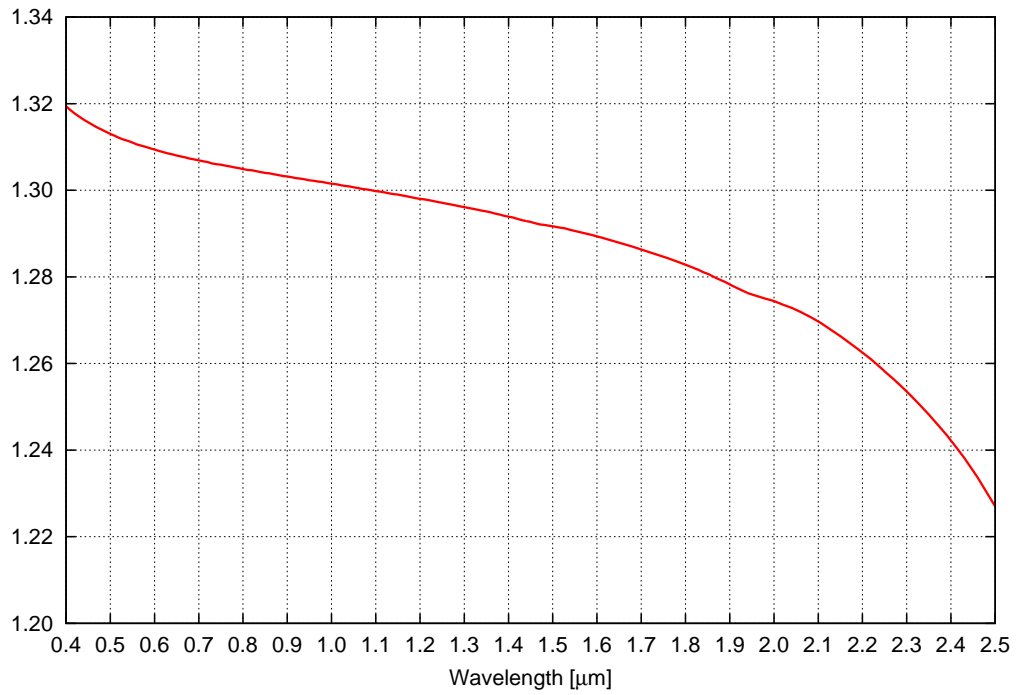
and the coefficients of the Legendre expansion are:

$$\beta_l = (2l + 1)g^l. \quad (3.18)$$

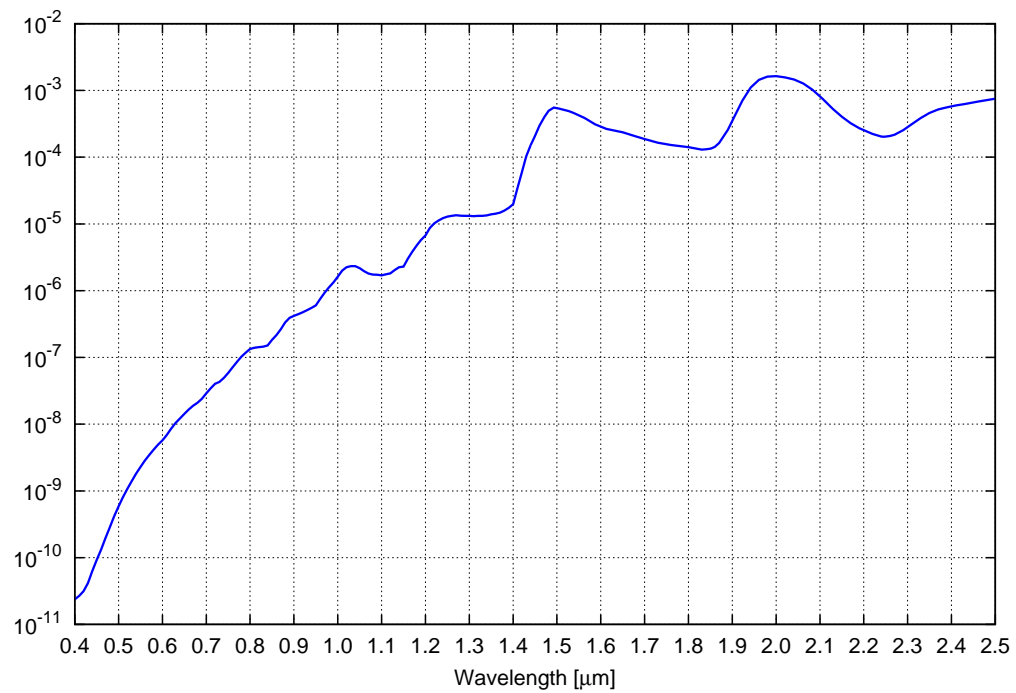
Therefore, the single particle optical properties can be, at minimum, characterized by knowledge of the single-scattering albedo and asymmetry parameter. Where a more accurate modeling is required, a number of additional scattering coefficients are requested to describe the particle phase function. Such parameters depend on the size of the particle, wavelength, index of refraction, and the shape of the particle. The most common approach to determine the optical properties is to assume that the particle is a perfect sphere, for which closed-form solution of the Maxwell equations is known. This approach is known as Mie theory (Wiscombe, 1980). This model has been widely used to describe the optical properties of snow, ice, and soil. More involved approaches, e.g. T-matrix (Mishchenko, Travis, et al., 2002), have been developed to account for arbitrary and irregular shapes, but tend to be computationally expensive.

3.2.1 Snow

From a radiative transfer perspective, snow can be viewed as a collection of ice particles immersed in air. A single particle of ice has variable shape and size and an exact description of the single-scattering albedo and phase function involves using methods of geometric optics. Monte Carlo based ray-tracing algorithms can be applied to retrieve the optical properties of ice crystals for a substantial variety of shapes including plates, hollow columns, bullet rosettes and ice aggregates. Accurate description of scattering properties for such complex shapes requires handling thousands of phase function coefficients, that results in impractical computationally expensive calculations. A more popular approach employed to describe snow particle optical properties makes extensive use of the Mie theory, enabling the computation of single-scattering albedo and asymmetry parameters as a function of the grain size (Wiscombe, 1980). Although single snow particles are not spheres, an ensemble of snow particles can be represented as optically equivalent to a collection of snow grains having the same volume/surface ratio. For example, Mugnai and Wiscombe (1980) demonstrated that a collection of non-oriented small spheroids have a scattering behavior correctly approximated by an



(a) real part



(b) imaginary part

Figure 3.1 Spectral behavior of the complex index of refraction for pure ice.

ensemble of spherical particles of equivalent size, especially for smooth oscillations of the borders. Thus, this approximation appears to be adequate for snow representation.

Mie-based codes require knowledge of the complex index of refraction:

$$n = n_r - m_i. \quad (3.19)$$

Generally, the real part is interpreted as phase velocity and the imaginary part describes the absorption loss for an electromagnetic wave moving through the particle. For the case of ice, the imaginary part is linked to the volume absorption of ice (Wiscombe and Warren, 1980). Figure 3.1 depicts the real and the complex parts of index of refraction for pure ice as function of wavelength. It is based on the compilation prepared by Warren and Brandt (2008).

As we can see, the magnitude of the imaginary part varies across the visible and the Near InfraRed (NIR) by many orders of magnitude. As a consequence, ice is transparent in the visible region (small imaginary index of refraction), but it is moderately absorptive in the NIR (imaginary index of refraction is larger and increases with wavelength). Using Mie theory, Wiscombe and Warren (1980) showed that the extinction coefficient and asymmetry parameter are relatively insensitive to wavelength (typical value for g ranges between 0.88 and 1), and that ω_λ (or the co-albedo $1 - \omega_\lambda$) is mainly responsible for the spectral variation of the snow albedo. Generally, ω_λ is very close to 1 in the optical region (highly scattering snow medium across the visible) and decreases monotonically reaching a minimum value of 0.5 in the NIR. At the same time, increasing the grain size is shown to decrease ω_λ .

Generally, values of 50 μm are assumed for fresh snow, whereas 1 mm is assumed for grain clusters or wet snow. Water in the snowpack is not usually modeled, as the index of refraction of water is very close to the one for ice.

3.2.2 Glacier ice

The major components of glacier surfaces are snow and ice. Nevertheless, the physical state and optical properties of various glacier ice vary dramatically. In fact, snowfall is transformed to ice through a variety of mechanisms including: mechanical settling, sintering, refreezing of meltwater, and refreezing of sublimating ice. The grain size of surface ice and rate of annealing varies widely: typically over time grain size increases, porosity decreases, and scattering surfaces decrease along photon pathways. At the same time, fine snow may persist and dominate in the accumulation zone. In the firn zone (i.e. annealed/recrystallized snow), grain size may be in the range of several millimeters. In the ablation zone, bubbly

ice may have effective grain size of a few millimeters, but dense, well crystallized ice may have grain sizes of 1 cm to 10 cm. In some cases, glaciers may present a layered structure, i.e. a dusting of snow or bubbly ice overlying denser and coarser ice.

Multiple scattering of such complex structures require proper modeling of the properties of the single components which are usually mixed with other components. Glacier clean ice can thus be modeled as a collection of bubbles, ranging from nearly zero bubbles to a majority fraction of bubbles, trapped within a matrix of transparent ice. The firn, which is the snow material after the transformation process has begun, is initially porous and contains interconnected air channels. As the density increases above 0.88 Mg m^{-3} , the channels close off resulting in a mixture of ice and bubbles trapped within the glacier body.

A framework for modeling the volumetric scattering of such bubbly ice has been proposed by Mullen and Warren (1988). In a pure ice sample containing only air bubbles, the physics of interaction of the photons and the host medium is such that absorption occurs in the ice matrix and the scattering occurs at the ice-bubble boundaries. This means that the absorption process can be modeled separately from the scattering process.

Scattering is dominated by the size and distribution of the air bubbles within the ice. If bubbles are assumed to be spheres, Mie theory can be employed to compute the scattering efficiency (and subsequently the scattering coefficient) as well as the asymmetry parameter as a function of the bubble size. Following the approach of Mullen and Warren (1988) the scattering efficiency of the bubble-ice mixture is computed by running the Mie code for a particle with the radius as the bubble and the index of refraction only real and equal to the real part of the snow index of refraction as seen in the previous subsection. The absorption coefficient is subsequently computed as function of the amount of ice per unit volume, using the data provided by Kou et al. (1993). Once the scattering and absorption coefficients are available, both the extinction coefficient and single-scattering albedo can be computed to complete the optical characterization of the volumetric scattering of clean ice.

3.2.3 Rock debris

Debris-covered glaciers may include also varying amounts, grain sizes, and spatial arrangements of rock debris. For example fine rock flour can be intimately mixed with ice or debris patches can be scattered among clean-ice exposures. The optical characterization of single-particle absorption and scattering for soil/sediment is very difficult, since soil particles distributions can vary in size, shape and mineralogy. Mishchenko, Dlugach, et al. (1999) proposed a way to describe the

Table 3.1 Symbols used to describe optical properties of mixtures.

| Symbol | Definition | Units |
|------------|------------------------------------|-----------------|
| n | number of particle per unit volume | m^{-3} |
| r | particle radius | m |
| Q_a | absorption efficiency | unitless |
| Q_s | scattering efficiency | unitless |
| Q_t | extinction efficiency: $Q_a + Q_s$ | unitless |
| Σ_s | scattering coefficient | m^{-1} |
| Σ_t | extinction coefficient | m^{-1} |
| ω | single-scattering albedo | unitless |
| g | asymmetry parameter | unitless |

soil particles optical properties through Mie theory, allowing the selection of the size distribution of the components. Although this approach considers soil particles as sphere with an effective radius, it appears to be adequate for simulation of snow/soil mixtures of glaciers.

More recently, T-Matrix code has been made available to describe the optical properties of particles that are large and irregular. T-matrix methods are also available to compute the optical properties of particle clusters with defined orientation. However, such algorithms are computationally expensive, and recently some of the available code has been re-designed to run on parallel clusters of machines (Mackowski and Mishchenko, 2011).

3.2.4 Mixtures

Optical properties of single particles can be employed to determine the optical behavior of multi-component mixtures. Computing the single-scattering albedo and the asymmetry parameter for a mixture is fairly straightforward.

Assuming spherical particles, and considering the definitions reported in Table 3.1, the scattering and extinction coefficients are:

$$\Sigma_s = n\pi r^2 Q_s \quad (3.20a)$$

$$\Sigma_t = n\pi r^2 Q_t. \quad (3.20b)$$

Consequently, the single-scattering albedo of the mixture of two components can be computed as a weighted average, i.e.:

$$\omega = \frac{\Sigma_{s,1} + \Sigma_{s,2}}{\Sigma_{t,1} + \Sigma_{t,2}} = \frac{n_1 \pi r_1^2 Q_{s,1} + n_2 \pi r_2^2 Q_{s,2}}{n_1 \pi r_1^2 Q_{t,1} + n_2 \pi r_2^2 Q_{t,2}}. \quad (3.21)$$

If the particles are not spherical, πr^2 shall be replaced by the relative particle cross sectional area. If the particle size is modeled as a size distribution, then computing an integral with the weighted size distribution is required. Similarly, the combined phase function moments are computed by averaging the moment of each component and weighted by its scattering coefficient. Thus, the asymmetry parameter of the two-component mixture is computed as follows:

$$g = \frac{g_1 \Sigma_{s,1} + g_2 \Sigma_{s,2}}{\Sigma_{s,1} + \Sigma_{s,2}} = \frac{g_1 n_1 \pi r_1^2 Q_{s,1} + g_2 n_2 \pi r_2^2 Q_{s,2}}{n_1 \pi r_1^2 Q_{s,1} + n_2 \pi r_2^2 Q_{s,2}}. \quad (3.22)$$

3.3 Numerical solution method

Computing the radiative regime within glaciers, as well as the amount of radiation reflected by glacier surfaces, requires solving the radiative transfer equation formally presented in the previous sections. Due to its mathematical complexity, an analytical exact description of the light field is virtually impossible.

Over the past years, many approximate methods have been developed to provide analytical expressions for the multiple scattering of photons in snow, ice, and soil. Among them, the most common and widely used has been formulated by Bruce Hapke. The general philosophy of this method is to derive analytical approximate expressions, which describe the essential physics of the scattering process. Specifically, the hearth of this approach relies on the separation of the radiant field into two main contributions: the single scattering radiance and the multiply scattered radiance. The former can be evaluated exactly for any arbitrary phase function, since the intensity subject to scattering is just the collimated incident light exponentially attenuated by passage through the matter. To compute the latter, instead, the two-streams approximation for isotropic scattering is used, leading to an analytical solution. Chandrasekhar (1960) has emphasized that for a semi-infinite medium, which is one of the most used hypothesis in the remote sensing field, the multiply scattered portion of the radiance field is much less sensitive to the particle phase function than the singly scattered fraction. This approximation is proven to be good to better than 15% (Hapke, 1981).

Whereas this model has among its strengths a somewhat acceptable accuracy and, more importantly, a simple and straightforward implementation, it violates the basic principle of photons conservation expressed in the transport equation and therefore is able to produce unphysical results. The widespread availability of high-speed digital computers permitted researchers to develop and test more efficient and faster algorithms to compute radiance and the reflectance factor, solving the complete radiative transfer equation.

A variety of techniques have been developed to solve the linear transport equation for photons. All of them are based on some form of discretization of the spatial and angular variable.

One approach is called *Invariant Embedding*. While the mathematical problem described in (3.1) may be classified as a linear two-points boundary value problem, it can be converted into a set of initial-value problems. Thus, a difficult but linear boundary value problem is transformed into a set of simpler but partly non linear initial-value problems. Mishchenko, Dlugach, et al. (1999) applied this strategy to compute the bidirectional reflectance factor of an optically thick surface of particulate media, including snow, ice, debris, and mixtures. The method is based on iteratively solving a non-linear integral equation (Ambartsumian equation) derived from photon conservation. The method has been proven to be efficient because it does not need to solve for the light inside the medium, and may be ideal for modeling the reflected radiance. Nevertheless, the assumptions of this method (i.e. one thick layer only) limit the applicability range on real situations.

Another prominent class among the scientific community is the *Discrete Ordinates* methods, that are based on discretizing the angular variable in a set of finite directions, and then solving the resulting differential equations. Therefore, it is based on a given quadrature formula for the integration on the angular variable. For example, the most popular code in the remote sensing community based on the solution of the radiative transfer equation is DISORT (Stammes, Tsay, and Laszlo, 2000; Stammes, Tsay, Wiscombe, et al., 1988), and it has been widely used by the community to compute the reflectance factor and spectral albedo of snow as a function of grain size

The spatial dependency in discrete ordinates methods may be represented in discrete or analytical form.

The former has been employed in the so-called S_n (Segment- n) method (Carlson and Bell, 1958). It has been proven to perform remarkably well in solving the neutron transport equation, especially in two and three dimensions (Ganapol, 2011). One major drawback of the method is that accurate solutions can only be obtained if the discretization mesh is sufficiently fine. For optically thick media and settings with forward peaked phase functions, the method becomes very slow due to the multiple sweeps in the angular and spatial variable. Most of these issues can be addressed by the *Converged SN (CSN)* method, proposed by Ganapol and Furfaro (2008), that couple coarse mesh rebalancing with acceleration techniques. In particular, Wynn's epsilon acceleration is applied on the angular discretization while a combination of the Romberg and Wynn's epsilon extrapolations is applied to the spatial discretization.

The latter, instead, originates in the pioneer work of Chandrasekhar (1960).

Recently, Siewert (2000) revised this solution scheme in a matrix formulation, transforming the problem of finding the separation constants as an eigenvalue problem, instead of finding the zeros of a specified polynomial. The method, called Analytical Discrete Ordinate Method (ADO), is capable of computing the radiative regime for a single layer with specified optical properties and thickness. With this novel semi-analytic approach, the angular variable is discretized to determine a set of ordinary differential equations that have the radiant intensities along the discrete directions as unknown. The set of equations are solved by: numerically solving the resulting eigenvalue problem to compute the homogeneous solution, and using a modified Green's function formulation to compute the particular solution of the set of differential equations arising from angular discretization. More recently, the method has been extended to include multiple layers of optical properties with special routines that give the method the ability to quickly and efficiently handle thousands of layers (Picca, 2009; Previti, 2010). It was confirmed to lead to extremely accurate results, with reasonably fast computation time. Importantly, this code, called MADOC⁵ has been used to provide the simulation examples in the next section.

3.3.1 MADOC

The theoretical and numerical basis of MADOC is here explained.

Since the upper boundary condition introduces into $I(\tau, \mu, \phi)$ components that are generalized functions, we follow Chandrasekhar (1960) and express the complete solution to the problem as a sum of two components. The former represents the free propagation of the incident beam (uncollided or solar term, $I_u(\tau, \mu, \phi)$), while the latter corresponds to the particles that have scattered at least one (collided, diffused or reduced term, $I_c(\tau, \mu, \phi)$):

$$I(\tau, \mu, \phi) = I_u(\tau, \mu, \phi) + I_c(\tau, \mu, \phi). \quad (3.23)$$

By introducing a finite set of N propagating directions, the solution of the uncollided intensity can be carried out analytically. In fact, (3.4) does not have for this case the scattering integral at the right-hand side, and therefore the equation to be solved is a simple first-order differential equation, that allows simple exponential solutions.

Making use of the decomposition of the phase functions in Legendre polynomials, the two-angle transport problem for diffuse intensity can be decomposed into a sequence of one-angle problems by expansion of the collided component in

⁵Multi-layer Analytic Discrete Ordinate Code

a Fourier series and by invoking the addition theorem (Chandrasekhar, 1960):

$$I_c(\tau, \mu, \phi) = \frac{1}{2} \sum_{m=0}^L (2 - \delta_{0,m}) I^m(\tau, \mu) \cos[m(\phi - \phi_0)]. \quad (3.24)$$

The equation for each $I^m(\tau, \mu)$ writes:

$$\mu \frac{\partial}{\partial \tau} I^m(\tau, \mu) + I^m(\tau, \mu) = \frac{\omega}{2} \sum_{l=m}^L \beta_l P_l^m(\mu) \int_{-1}^1 d\mu' P_l^m(\mu') I^m(\tau, \mu') + f_0 \frac{\omega}{2} e^{-\tau/\mu_0} \sum_{l=m}^L \beta_l P_l^m(\mu) P_l^m(\mu_0). \quad (3.25)$$

The solution of (3.25) can be written as the sum of a homogeneous and a particular solution due to the illumination source:

$$I^m(\tau, \mu) = I_h^m(\tau, \mu) + I_p^m(\tau, \mu). \quad (3.26)$$

Having set an half range quadrature scheme (i.e. $2N$ direction symmetrical with respect to $\mu = 0$), the homogeneous solution is cast into an eigenvalue problem and expressed as a linear combination of eigenfunctions (Siewert, 2000), whereas the particular solution is expressed through the infinite medium Green's function (Barichello et al., 2000). In MADOC, the Gauss-Legendre quadrature scheme is adopted for the approximation of the scattering integral. With this approach, the direction of propagation are chosen to be the zeros of the Legendre polynomial of order N . As described in literature (Lewis and Miller, 1984), the Gauss-Legendre scheme is a typical choice as it allows an exact integration of polynomials of order $2N + 2$ and in general gives accurate results for a broad class of functions.

In the generic homogeneous s -th layer, the formal solution of (3.4) can still be found by applying this method. For each layer, the homogeneous part of the solution contains $2N$ arbitrary constants, that are found by imposing the boundary conditions of (3.5) and the continuity of the intensities at the each interface of (3.7). Finally, the intensity at each position τ can be calculated through an analytical post processing, where the discrete-ordinates solution found so far is used to approximate the integral part of the radiative transfer equation, and the required intensity is computed solving a first-order differential equation using the method of separation of constants.

The implementation and the optimization through convergence acceleration (Brezinski, 2000) of the ADO methodology to multi-layer configurations, as well as its validation through the benchmarks available in the literature has been the topic of previous works (Picca, 2009; Previti, 2010; Previti et al., 2011).

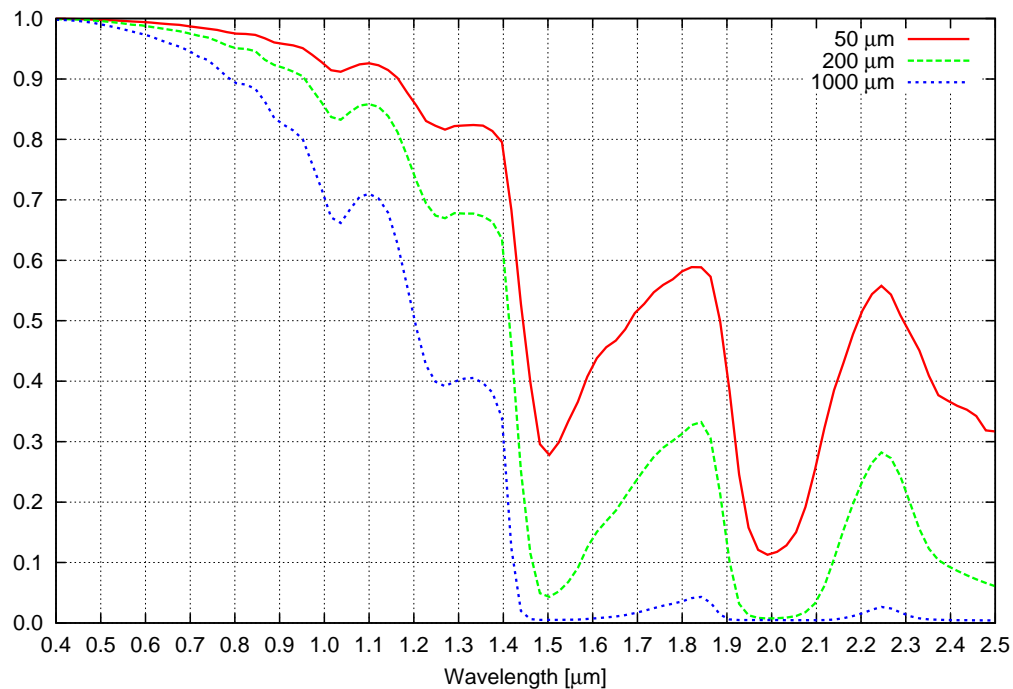


Figure 3.2 Spectral albedo for a layer of optically thick pure snow as a function of wavelength and grain size. The solar zenith angle is 30 degrees.

For the purpose of our simulations, we computed the single-scattering albedo as well as the coefficients of the Legendre expansion of the phase function using the Mie routines written in MATLAB® provided by Mätzler (2002). The latter has been coupled with MADOC to demonstrate how linear transport theory can be successfully employed to simulate radiative regimes typical of glacier environments.

3.4 Glacier simulations results

In this section, a set of numerical examples that show how radiative transfer theory can be employed to model BRF and spectral albedo for a variety of configurations typically found in alpine glaciers.

Figure 3.2 reports the *first* set of simulations. The radiative transfer theory has here been employed to evaluate the response of an optically thick layer of pure snow. The spectral albedo has been computed as a function of wavelength in the range $0.4\ \mu\text{m}$ to $2.5\ \mu\text{m}$ (i.e. subdividing the range into 100 parts, and repeating the transport calculation for each wavelength separately) and grain size. The solar zenith angle was set at 30° . The single-particle optical properties of single-scattering albedo and asymmetry parameter, were computed using the MATLAB-

based Mie-code provided by Mätzler (2002), using the collection of complex index of refraction for ice prepared by Warren and Brandt (2008). The ice grain sizes considered are: 50 μm (fresh fine snow), 200 μm (fresh coarse snow), and 1 mm (annealed snow, i.e. firn).

The overall single-scattering albedo and asymmetry parameter have been computed considering a mixture of ice particles and air. We have assumed a diffuse ice packaging of sphere totaling 10.9% by volume. This would be like spherical ice particles interconnected by radiatively and volumetrically negligible ice tendrils. Considering an ice density $\rho_{\text{ice}} = 0.918 \text{ g cm}^{-3}$, the overall density of snow is then 0.1 g cm^{-3} . We computed the number density of ice particles in snow as:

$$n_{\text{ice}} = \frac{\text{volume density of ice in snow}}{\text{volume ice particle}} = \frac{0.109}{\frac{4}{3}\pi r_{\text{ice}}^3}. \quad (3.27)$$

The simulation has been performed with $N = 50$ points for the quadrature of the scattering integral and with a $L = 50$ expansion of phase function. The Legendre coefficients of (3.16) have been computed using the Heyney-Greenstein model as specified in (3.18).

As shown in Figure 3.2, the albedo is very sensitive to the grain size and decreases as the radius of the snow particle increases. From a physical point view, photons have higher chances to be scattered at the boundary between fine snow grains and air. Incrementally larger grain size has the effect of increasing the free mean path, giving the photons a higher chance to travel through the ice, and a smaller chance to be scattered and exit the snowpack. Whereas larger snow particles are both more absorptive and more forward scattering, it can be shown that the decrease in albedo is mainly due to the fall of ω_{λ} in the NIR regime, where the asymmetry parameter increases only slightly (Wiscombe and Warren, 1980). Importantly, in the visible region of the spectrum, the snow particles are highly scattering (ω_{λ} very close to 1), that explains why snow has generally such a high albedo, independent of grain size.

The *second* set of simulations, reported in Figure 3.3, depict the variability of the spectral albedo with respect to the solar zenith angle. In this case the ice grain size was fixed and assumed to be 50 μm . Mie theory is used to compute the single-particle optical properties as in the previous set of simulations. As expected, the angle of incidence of the incoming radiation illuminating the snowpack has a large effect on the albedo. As shown in Figure 3.3, the albedo increases with an increasing solar zenith angle. Wiscombe and Warren (1980) explained this phenomenon by postulating that because of the high inclination with respect to the zenith, photons entering the medium travel close to the upper surface of the snowpack and therefore scattering events give light particles a higher probability

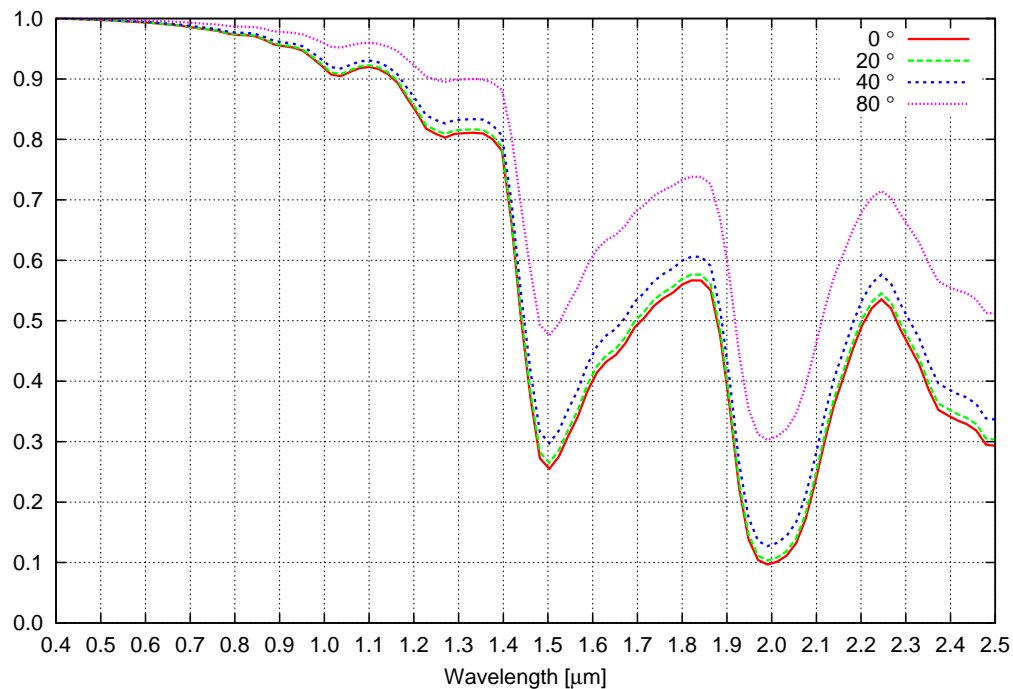


Figure 3.3 Spectral albedo for a layer of optically thick pure snow as a function of wavelength and solar zenith angle. The particle grain size is fixed and assumed to be $50\ \mu\text{m}$.

of exiting the snowpack surface.

For the *third* set of simulations, reported in Figure 3.4, we considered an optically thick mixture of pure snow and carbon soot, as a function of ice grain size ($50\ \mu\text{m}$, $20\ \mu\text{m}$, $1000\ \mu\text{m}$). The aim of these calculation is to mimic the reflectance of dirty snow. As usual, the optical properties of the two constituents have been independently computed using Mie theory. The optical properties of the carbon soot have been computed (assuming that soot particles are modeled as spheres) by setting the soot radius equal to $0.1\ \mu\text{m}$ and particle density equivalent to $0.3\ \text{ppmw}$. The soot complex index of refraction is assumed to be constant across the spectral range of interest and equal to $1.95 - 0.79i$ (Gardner and Sharp, 2010). Figure 3.4 shows the resulting spectral albedo as a function of wavelength with radius of the snow particles. The simulations show that a small amount of carbon soot is sufficient to lower the albedo in the visible region of the spectrum where ice has the lowest absorption (highly scattering media with single-scattering albedo very close to 1). As expected, the albedo reduction is more marked for larger snow particles. Relative high scattering between $0.4\ \mu\text{m}$ to $0.7\ \mu\text{m}$ increases the probability that photons are more likely to experience multiple scattering, therefore increasing the probability of encountering a carbon particle and being absorbed.

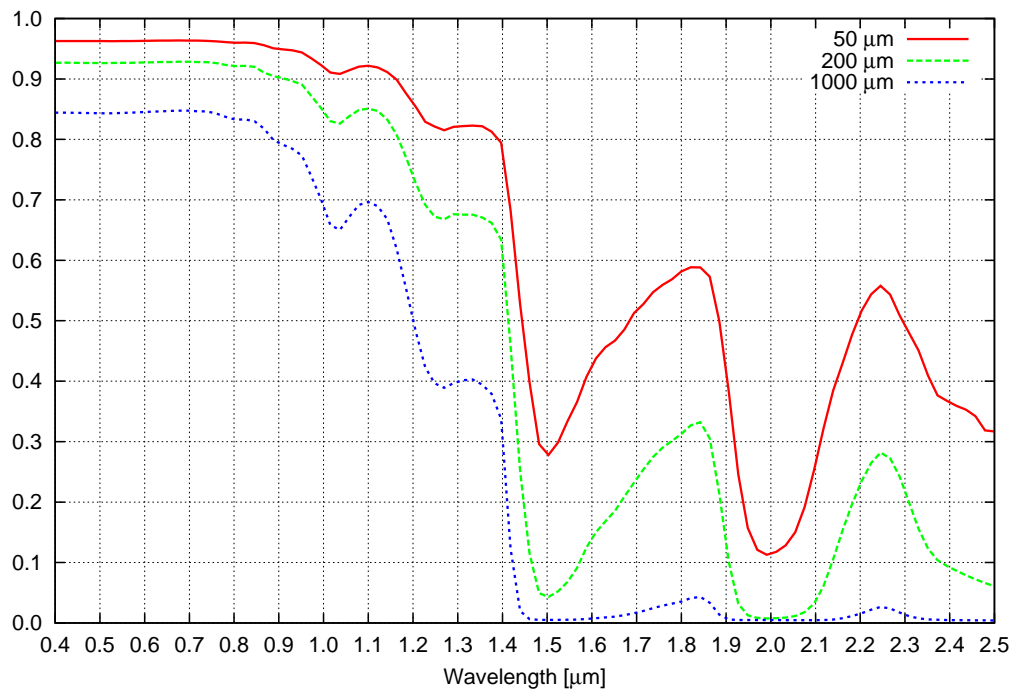


Figure 3.4 Spectral albedo for a layer of optically thick mixture of pure snow and carbon soot as a function of wavelength and snow grain size. Soot particle concentration is assumed to be 3 ppmw.

As discussed above, increasing the snow particle grain size increases the average free mean path, further increasing the probability of encountering a carbon particle and being absorbed. In the NIR region (i.e. above $0.9\ \mu\text{m}$) the influence of carbon particles on the albedo is limited, as its reduction is dominated by the stronger absorption of ice. This simulation shows that carbon soot and generally other impurities may have a large impact on the overall energy budget of glaciers.

Figure 3.5 reports the *fourth* set of simulations. Here we consider a two-layer medium: a snow layer of fine pure snow (grain size $50\ \mu\text{m}$) over an optically thick layer of glacier ice (air bubble filled). The computation has been repeated for various thickness of the snow layer. The optical properties of pure snow has been computed as in previous simulations. Instead, for bubbly ice we employed a different approach (Mullen and Warren, 1988). Assuming the radius of a bubble equal to $0.3\ \text{mm}$, the scattering efficiency of the bubble-ice mixture has been calculated running the Mie code for a particle with the radius as the bubble and index of refraction equal only real and equal to the one of ice. The absorption coefficient has then been computed multiplying the absorption coefficient of pure ice (Kou et al., 1993) per the volume fraction of ice. In our case we assumed $V_{\text{air}} = 0.15$ and $V_{\text{ice}} = 0.85$. Finally, the optical thickness of the layer of pure snow has been

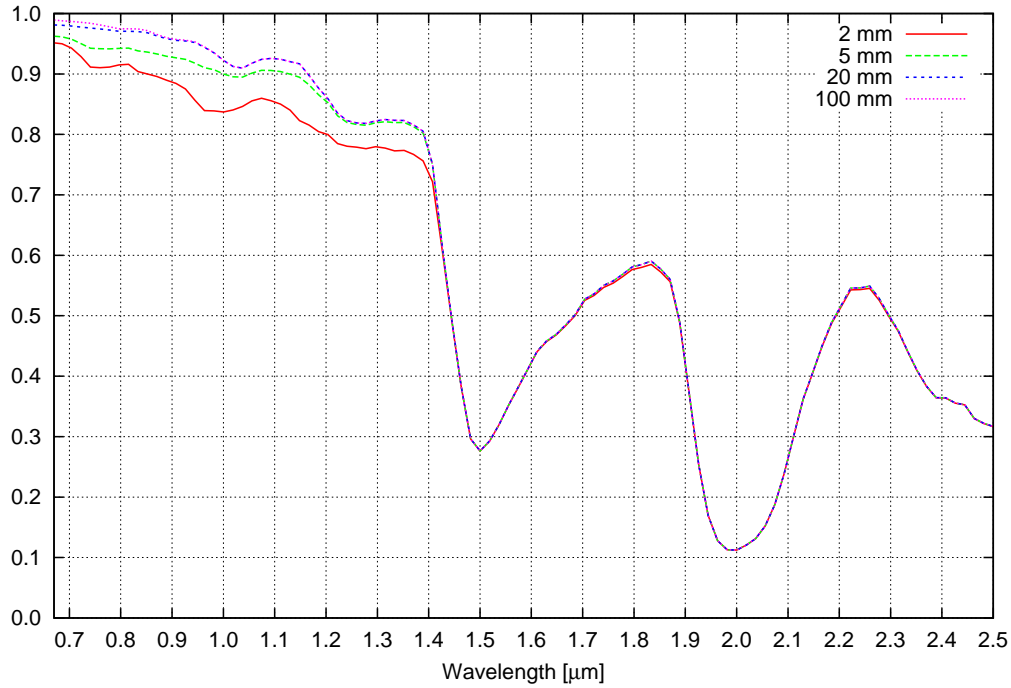


Figure 3.5 Spectral albedo for a layer of pure snow over a layer of optically thick ice as a function of wavelength and snow depth. The snow particle grain size is assumed to be $50 \mu\text{m}$.

set equal to:

$$\tau_{\text{snow}} = \frac{3 \rho_{\text{snow}} z Q_{t,\text{snow}}}{4 r_{\text{ice}} \rho_{\text{ice}}}, \quad (3.28)$$

where τ_{snow} is the optical thickness of the snow layer, $\rho_{\text{snow}} = 918 \cdot 0.109 = 100 \text{ kg m}^{-3}$ is the density of the snow, z is the snow geometrical depth in m, r_{ice} is the snow grain radius in m, and $\rho_{\text{ice}} = 918 \text{ kg m}^{-3}$ is the density of ice. As we can see from Figure 3.5, the spectral albedo in the visible range is sensitive to the depth of the snow layer. This enables an estimation of the amount of the snowfall measuring the reflectance through remote sensing instruments.

Finally, the *fifth* set of simulations shows an example of a BRF for an optically thick mixture of soil and ice as a function of the percentage in volume of the two pure components. The input parameters, including complex index of refraction, grain size, and grain size distribution for both soil and snow are reported in Table 3.2. The mixture was computed at a specified wavelength in the visible region of the spectrum, i.e. $0.63 \mu\text{m}$. The 641 coefficients of the Legendre expansion of the phase function as well as the single scattering albedo have been computed following the methodology and using the code provided by Mishchenko, Dlugach, et al. (1999). Figure 3.6 demonstrates the reflectance variability associated with intimate mixtures of ice and sediment/soil. As we can see, and following common

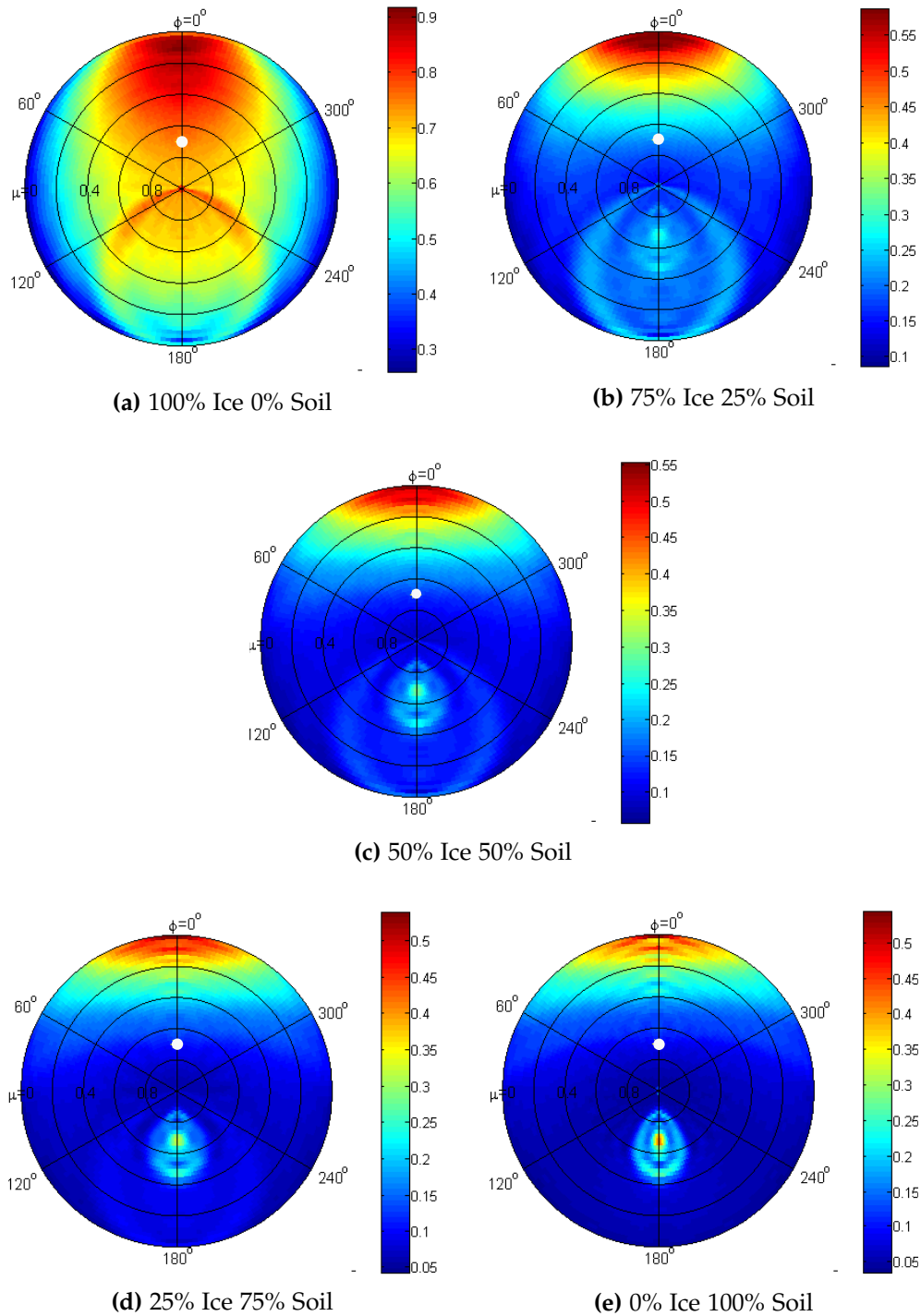


Figure 3.6 BRF simulations for intimate mixtures (in volume percentage) of ice and sediment/soil. The white dot represents the impinging solar beam. The overall magnitude (i.e. albedo) decreases as the percentage of soil increases. The BRF patterns are also a function of the mixture percentage. This set of simulations shows that BRF patterns can be potentially used to discriminate between various surface materials and conditions in glacier environments.

Table 3.2 Input optical parameters employed for MADOC BRF simulations of intimate and areal mixtures of ice and soil.

| | Ice | Soil |
|-----------------------------|--------------------|--------------------|
| Wavelength | 0.63 μm | 0.63 μm |
| Particle diameter | 30 μm | 30 μm |
| Variance | 0.2 | 0.1 |
| Distribution | Log Normal | Modified gamma |
| Index of Refraction (Real) | 1.31 | 1.55 |
| Index of Refraction (Imag) | 0 | 0.001 |
| Max radius | 35 | |
| Min radius | 25 | |
| Single-scattering albedo | 1 | 0.85413 |
| Max scattering coefficients | 641 | 641 |
| Type of simulation | Intimate Mixture | Intimate Mixture |

sense, the magnitude of reflectance decreases with increasing percentage of sediment/soil. Also, pure ice exhibits a highly variable pattern that is directionally dependent. This anisotropic reflectance changes with increasing sediment. In particular, the azimuthal reflectance variations become more spatially homogeneous. The forward-scattering component also decreases in extent and magnitude, while the backscatter component decreases in extent, and exhibits an increase in magnitude associated with increasing debris.

References

- L. B. Barichello, R. D. M. Garcia, and C. E. Siewert (2000). "Particular Solutions for the Discrete-Ordinates Method". In: *Journal of Quantitative Spectroscopy and Radiative Transfer* 64, pp. 219–226.
- M. P. Bishop, R. G. Barry, A. B. G. Bush, L. Copeland, J. L. Dwyer, A. G. Fountain, W. Haeberli, D. K. Hall, A. Käab, J. S. Kargel, B. F. Molnia, J. A. Olsenholler, F. Paul, B. H. Raup, J. F. Shroder, D. C. Trabandt, and R. Wessels (2004). "Global Land Ice Measurements from Space (GLIMS): Remote sensing and GIS investigations of the Earth's cryosphere". In: *Geocarto International* 19.2, pp. 57–85.
- C. Brezinski (2000). "Convergence acceleration during the 20th century". In: *Journal of Computational and Applied Mathematics* 122, pp. 1–21.
- A. B. G. Bush (2000). "A positive feedback mechanism for Himalayan glaciation". In: *Quaternary International* 65/66, pp. 3–13. DOI: 10.1016/S1040-6182(99)00033-6.
- B. G. Carlson and G. I. Bell (1958). "Solution of the transport equation by the Sn method". In: *Proceedings of the second international conference on the peaceful uses of atomic energy*. Vol. 16, p. 535.
- S. Chandrasekhar (1960). *Radiative Transfer*. Dover.
- A. B. Davis and Y. Knyazikhin (2005). "A Primer in 3D Radiative Transfer". In: *3D Radiative Transfer in Cloudy Atmospheres*. Vol. 2. Springer Berlin Heidelberg, pp. 153–242.
- R. Furfaro and B. D. Ganapol (2007). "Spectral Theory for Photon Transport in Dense Vegetation Media: Caseology for the Canopy Equation". In: *Transport Theory and Statistical Physics* 36, pp. 107–135. DOI: 10.1080/00411450701456824.
- B. D. Ganapol (2011). "Radiative Transfer with Internal Reflection via the Converged Discrete Ordinates Method". In: *Journal of Quantitative Spectroscopy and Radiative Transfer* 112, pp. 693–713.
- B. D. Ganapol and R. Furfaro (2008). "The Art of Analytical Benchmarking". In: *Computational Methods in Transport: Verification and Validation*. Vol. 62. Springer Berlin Heidelberg, pp. 105–134.
- A. S. Gardner and M. J. Sharp (2010). "A review of snow and ice albedo and the development of a new physically based broadband albedo parameterization". In: *Journal of Geophysical Research* 115, F01009. DOI: 10.1029/2009JF001444.
- B. Hapke (1981). "Bidirectional Reflectance Spectroscopy. 1. Theory". In: *Journal of Geophysical Research* 86.B4, pp. 3039–3054.
- L. G. Henyey and J. L. Greenstein (1941). "Diffuse radiation in the galaxy". In: *Astrophysical Journal* 93, pp. 70–83.

- J. S. Kargel, M. J. Abrams, M. P. Bishop, A. Bush, G. Hamilton, H. Jiskoot, A. Käab, H. H. Kieffer, E. M. Lee, F. Paul, F. Rau, B. Raup, J. F. Shroder, D. Soltesz, D. Stainforth, L. Stearns, and R. Wessels (2005). "Multispectral imaging contributions to global land ice measurements from space". In: *Remote Sensing of the Environment* 99, pp. 187–219.
- L. Kou, D. Labrie, and P. Chylek (1993). "Refractive indices of water and ice in the 0.65-2.5 μm spectral range". In: *Applied Optics* 32.19, pp. 3531–3540. DOI: 10.1364/AO.32.003531.
- E. E. Lewis and W. F. Miller (1984). *Computational Methods of Neutron Transport*. Wiley-Interscience.
- D. W. Mackowski and M. I. Mishchenko (2011). "A multiple sphere T-matrix Fortran code for use on parallel computer clusters". In: *Journal of Quantitative Spectroscopy and Radiative Transfer* 112.13, pp. 2182–2192. DOI: 10.1016/j.jqsrt.2011.02.019.
- M. Maisch (2000). "The longterm signal of climate change in the Swiss Alps: Glacier retreat since the end of the Little Ice Age and future ice decay scenarios". In: *Geografia Fisica e Dinamica Quaternaria* 23.2, pp. 139–151.
- C. Mätzler (2002). *MATLAB Functions for Mie Scattering and Absorption*. Research Report 2002-08. Institut für Angewandte Physik: Universität Bremen. URL: <http://diogenes.iwt.uni-bremen.de/vt/laser/codes/Mie-Matlab-Maetzler.zip>.
- M. I. Mishchenko, J. M. Dlugach, E. G. Yanovitskij, and N. T. Zakharova (1999). "Bidirectional reflectance of flat, optically thick particulate layers: An efficient radiative transfer solution and applications to snow and soil surfaces". In: *Journal of Quantitative Spectroscopy and Radiative Transfer* 63, pp. 409–432.
- M. I. Mishchenko, L. D. Travis, and A. A. Lacis (2002). *Scattering, Absorption, and Emission of Light by Small Particles*. Cambridge University Press.
- A. Mugnai and W. J. Wiscombe (1980). "Scattering of radiation by moderately nonspherical particles". In: *Journal of Atmospheric Science* 37, pp. 1291–1307.
- P. C. Mullen and S. G. Warren (1988). "Theory of the optical properties of lake ice". In: *Journal of Geophysical Research* 93.D7, pp. 8403–8414.
- P. Picca (2009). "Applications of the Boltzmann Equation to the Neutronics of Nuclear Reactors and Radiative Transport". Ph.D. thesis. Politecnico di Torino.
- A. Previti (2010). "Semi-Analytic Radiative Transfer Model for Remote Sensing of Planetary Surfaces". Master's thesis. Alma Mater Studiorum Università di Bologna.
- A. Previti, R. Furfaro, P. Picca, B. D. Ganapol, and D. Mostacci (2011). "Solving radiative transfer problems in highly heterogeneous media via domain de-

- composition and convergence acceleration techniques". In: *Applied Radiation and Isotopes* 69.8, pp. 1146–1150.
- B. Raup, A. Kääh, J. S. Kargel, M. P. Bishop, G. Hamilton, E. Lee, F. Paul, F. Rau, D. Soltesz, S. J. S. Khalsa, M. Beedle, and C. Helm (2007). "Remote sensing and GIS technology in the Global Land Ice Measurements from Space (GLIMS) Project". In: *Computers and Geoscience* 33.1, pp. 104–125. DOI: 10.1016/j.cageo.2006.05.015.
- C. E. Siewert (2000). "A concise and accurate solution to Chandrasekhar's basic problem in radiative transfer". In: *Journal of Quantitative Spectroscopy and Radiative Transfer* 64, pp. 109–130. DOI: 10.1016/S0022-4073(98)00144-7.
- K. Stammes, S.-C. Tsay, and I. Laszlo (2000). *DISORT, a General-Purpose Fortran Program for Discrete-Ordinate-Method Radiative Transfer in Scattering and Emitting Layered Media: Documentation of Methodology*. Tech. rep. NASA.
- K. Stammes, S.-C. Tsay, W. J. Wiscombe, and K. Jayaweera (1988). "Numerically stable algorithm for discrete-ordinate-method radiative transfer in multiple scattering and emitting layered media". In: *Applied Optics* 27, pp. 2502–2509.
- G. E. Thomas and K. Stammes (1999). *Radiative Transfer in the Atmosphere and Ocean*. Cambridge University Press.
- S. G. Warren and R. E. Brandt (2008). "Optical constants of ice from the ultraviolet to the microwave: A revised compilation". In: *Journal of Geophysical Research* 113, p. D14220. DOI: 10.1029/2007JD009744.
- W. J. Wiscombe (1980). "Improved Mie Scattering Algorithms". In: *Applied Optics* 19.9, pp. 1505–1509.
- W. J. Wiscombe and S. G. Warren (1980). "A model for the spectral albedo of snow. I. Pure snow". In: *Journal of Atmospheric Science* 37, pp. 2712–2733.

Conclusions

The aim of this work has been to explore various applications of the transport theory for industrial and environmental protection purposes, and specifically to neutron and photon transport. The numerical modeling required for nuclear reactor analysis and remote sensing applications has been discussed, presenting our research devoted to provide fast, accurate, and efficient tools to analyze such systems.

Chapter 1 has been dedicated to the application of neutron transport theory for nuclear reactor applications, and in particular to the acceleration of the computation. A direct calculation for whole core heterogeneous geometries represents a challenge for the extreme complexity and correlated great computational effort. Typically, homogenization techniques are employed to collapse spatial heterogeneities into homogenized equivalent cross sections, unfortunately introducing substantial error in the flux distribution and leading to inaccurate prediction of punctual reaction rates. The augmentation of the computation power in modern computers coupled with a renewed research in a more precise numerical tools is gradually making increasingly possible to study clusters of fuel assemblies and small cores in full transport theory and even in 3D geometries, without assuming spatial homogenization.

In particular, the Method of Short Characteristics (MSC) implemented in the code IDT-APOLLO has been recently extended to take into account heterogeneous Cartesian cells, to exactly represent the ordinary fuel pins of water-moderated reactors. However, proper acceleration techniques are of paramount importance in order to make the problem tractable and the solution feasible for industrial and research needs. Convergence acceleration techniques applied to source iterations based transport codes are essential when the regions in the spatial mesh are optically thick and the scattering to total extinction ratio is very close to unity. Applications to nuclear reactors and shields usually employs finer meshes, but the extreme heterogeneities coupled with the steep gradients of the neutron flux make practical simulations very slow. Acceleration methods are therefore useful to greatly reduce the overall computational burden.

We concentrated our efforts in the implementation of the Boundary Projection Acceleration (BPA) for the peculiar heterogeneous Cartesian cells of IDT-APOLLO. Being a linear acceleration scheme, it is guaranteed to converge to the unaccelerated (source iteration) equation. The BPA is a synthetic transport acceleration technique that involves a lower order angular discretization for the construction of the transport operator. The calculation of the response matrices of the acceleration problem has been carried out by integration and projection of the matrices used by free iterations. The acceleration scheme has been further enhanced considering the boundary source residual error, increasing the consistency of the acceleration model.

The results provided by the C5G7 benchmark in 2D and 3D configurations demonstrate the effectiveness of the BPA. More specifically the number of internal iterations needed to achieve convergence drops by a factor of 4 in 2D and by a factor of 6 in 3D. Comparison with the non-linear Coarse Mesh Finite Differences (CMFD) acceleration scheme manifests the spectral superiority of the BPA method. However, considering the total CPU time, BPA appears more competitive than CMFD only for higher S_N angular discretization. In fact, the CMFD approach involves a pre-homogenization phase, where the number of unknowns is by far reduced, as opposed to BPA, that only degrades the angular representation while preserving the full description of the spatial heterogeneities.

The effect of the CMFD acceleration applied to the external iteration has been studied as well. The combination of CMFD (external iterations) and BPA (internal iterations) has been proved to be more efficient than other methods based on Chebyshev acceleration and group rebalance. In particular the savings in terms of total inner iterations is 4-fold in 2D and 2-fold in 3D.

Regarding the spatial representation of the angular flux, in the cases examined in 2D and 3D the linear characteristics scheme has manifested to be sensibly more accurate than the constant one. On the other side, bilinear has not provided substantial gain in the precision of the eigenvalue estimation, while increasing the cost in terms of calculation time.

In Chapter 2 we focused our attention on the temperature effects in the elastic scattering for heavy isotopes accounting for the anisotropy of elastic scattering in the center of mass reference system. Nuclear data processing codes like NJOY usually neglect the temperature dependency of transfer kernel above the thermal region, assuming the asymptotic model, that considers only down-scattering. It has already been proven that there is a sensible probability of elastic up-scattering by resonant isotopes in the vicinity of the thermal region. In particular, the probability of up-scattering increases on the left side of the resonance. Therefore the effect is particularly important when a pair of absorption and scattering reso-

nances are very close. In such cases, during the slowing down a neutron may be sent back to an higher energy by the up-scattering effect just mentioned and it should be passed through the absorption peak multiple times. However, the bulk of neutrons usually slows down in the moderator, and since this effect is pronounced only for heavy isotopes, it may occur mostly on the periphery of the fuel pin. Elastic up-scattering is shown to affect the calculation of reactivity as well as the neutron balance and then the fuel burn-up.

We proposed a method for computing the Doppler-broadened transfer kernel for elastic scattering of heavy nuclei that accounts for resonance behavior, and we determined the angular moments by an accurate angular quadrature. Then this methodology can be applied to the generation of multigroup transfer matrices for deterministic transport computations, and there is also a potential for applications to Monte Carlo.

We employed an exponential cutoff to limit the interval of the integral defining the Doppler-broadened transfer kernel. This approach has been proved to be very efficient in reducing the overall computational burden while avoiding numerical instabilities. The accuracy of the algorithm has been proved from comparison with analytic solutions for constant cross section. Regarding the angular moments calculation, two types of representations have been tested: a global collocation technique based on the Gauss-Legendre nodes, and a simpler continuous piecewise linear interpolation. An increased difficulty for the angular moment numerical quadrature has been found for exiting neutron energies close to the impinging energy, that comes from the singularity of the kernel at $E' = E$. Subsequent refinements of the angular representation has enabled the precise evaluation of the angular moment integral, with good agreement with previously published results.

We first considered the case of an isotropic scattering law in the center of mass system. Analysis of the transfer kernel for ^{238}U increasing the temperature have demonstrated the presence of a pronounced up-scattering peak for back-scattering angles at 1000 K. The behavior of the angular moments has been studied as well. In particular, it has been found that the effect of up-scattering at high temperatures is present only for the first resolved resonances at few eV. At higher energies the validity of the asymptotic models has been confirmed.

We then studied the effect of anisotropy in the scattering law. From the analysis of the cross section data, it is shown that ^{238}U presents anisotropy of the scattering only for energies above 1 keV. As a consequence, there is no sensible up-scattering prompted by resonances.

Chapter 3 has been dedicated to photon transport theory, and in particular how it can be employed to quantify the amount of radiation reflected by glacier

surfaces in the study of Earth's cryosphere. Numerical modeling of radiative transfer equation has provided the scientific community with a numerical algorithm that permits the computation of physical quantities of interest in remote sensing, like BRF and spectral albedo, both efficiently and accurately.

However, such radiance calculations are only meaningful if knowledge of the medium optical properties is available, since they require the input of explicit models for single-scattering albedo and scattering phase function, that in turn depends upon the use of absorption and scattering coefficients (or efficiencies), the asymmetry parameter (or Legendre coefficients describing the series expansion of the phase function), particle concentrations, wavelength of interest, as well as size and shape of the single-type particles/mixture of many-type particles describing the medium. Mie theory is the most popular way to determine such properties, and it is based on the assumption that a single particle is spherical. Mie-based codes have been designed to compute the aforementioned parameters as a function of the complex index of refraction and particle size. The modeling of the optical properties of glacier environments, i.e. snow, ice, soil, and mixtures, has been discussed, including extensive analysis of the validity of the approximations employed.

The radiative transfer simulation examples have demonstrated that modeling can be effectively employed as an investigative tool to assess the information content in satellite images. Furthermore they show how typical glacier surface conditions and glacial lakes optically respond as a function of their morphological and mineralogical composition. Consequently, the coupling of radiative transfer modeling and multispectral digital image analysis can be used to assess important biophysical parameters of glacier environments, such that the ingesting of sensor data can produce spatio-temporal quantitative information regarding the observed medium including ice grain size, percentage of carbon soot in snow, concentration of glacier flour in lakes, pixel debris cover percentages. The latter reinforce the significance of radiative transfer modeling for studying and understanding the Earth's cryosphere.

Acknowledgments

A special thanks goes to the team of the Laboratory of Montecuccolino, and in particular to my supervisor prof. Domiziano Mostacci, for its support and guidance in the last few years of my university studies, and to prof. Marco Sumini, for the interesting discussions.

I am very grateful to a couple of key figures of professional career, Barry Ganapol and Richard Sanchez, who stimulated me the passion for transport theory and numerical methods.

A big “thank you” goes to all the researchers and colleagues of the CEA center in Saclay, in particular to Emiliano, Simone, and Igor. Thank you for your support, for the interesting discussions, for the good time spent together, for having welcomed me so warmly in your team.

I want to specifically acknowledge my family: my mother, my father, and my brother always encouraged me during all my university studies, and without their continuous advice, their support, and our interesting discussions I will not be here.

Curriculum Vitae

Education

- 06/2010 – 07/2010: Italian professional qualification examination, Engineer (sector A – industrial engineer), with final grade of 228/240.
- 09/2007 – 03/2010: Master Degree in Energy Engineering, 110/110 summa cum laude, University of Bologna (Italy)
Thesis title: “Semi-Analytic Radiative Transfer Model for Remote Sensing of Planetary Surfaces”, at The University of Arizona - Aerospace and Mechanical Engineering
Advisor: prof. Domiziano Mostacci
Co-advisors: prof. Roberto Furfaro, prof. Barry D. Ganapol
- Bachelor Degree in Energy Engineering, 110/110 summa cum laude, University of Bologna (Italy)
Thesis title: “Profiles of Concentration of Natural Radionuclides in Environmental Matrices of Remote Places”
Advisor: prof. Domiziano Mostacci
Co-advisor: prof. Laura Tositti

Courses

- 2007/08/19-31: Jülich Nuclear Chemistry Summer School (JUNCSS07), Aachen University of Applied Sciences, Jülich (Germany)
- 2011/03/07-18: Intensive Course on Accelerators and Reactor Operation (ICARO2011), Istituto Tecnologico e Nuclear, Lisbon (Portugal)
- 2011/05/25-27: 46th theoretical and practical course in neutron measurements, Calci e Pisa (Italy)
- 2011/06/14-17: 6th Summer School on Actinide Science and Applications, JRC-ITU, Karlsruhe (Germany)
- 2011/06/05-08: 3rd Operational Issues in Radioactive Waste Management and Nuclear Decommissioning, JRC-ISPRA, Ispra, Varese (Italy)
- 2011/09/05-16: 20th Summer School of Parallel Computing, CINECA, Bologna (Italy)
- 2011/10/10-14: 7th Advanced School of Parallel Computing, CINECA, Bologna (Italy)

- 2013/03/18-22: Analytical Benchmarks: Case Studies in Neutron Transport Theory, OECD/NEA, Issy-les-Moulineaux (France)

Research periods abroad

- 2009/09/11 - 2010/02/28: The University of Arizona, Department of Aerospace Engineering, United States of America
- 2013/03/18 - 2013/12/20: Commissariat à l'Énergie Atomique et aux Énergies Alternatives, Centre de Saclay, Service d'Études des Réacteurs et des Mathématiques Appliquées, Laboratoire de Transport Statistique et Déterministe, France

Teaching experience

- Teaching assistantship for the course "Metodi matematici per l'energetica M" held by prof. Domiziano Mostacci, University of Bologna (Italy)
- Teaching assistantship for the course "Radioprotezione M" held by prof. Marco Sumini, University of Bologna (Italy)

Publications

- **Alberto Previti**, Roberto Furfaro, Paolo Picca, Barry D. Ganapol, Domiziano Mostacci, Solving radiative transfer problems in highly heterogeneous media via domain decomposition and convergence acceleration techniques, Applied Radiation and Isotopes 69.8, (2011), 1146-1150. [paper]
- Laura Tositti, Domiziano Mostacci, Erika Brattich, Giorgia Cinelli, **Alberto Previti**, Silvia Sandrini, Daniela Baldacci, Silvia Parmeggiani, Serie temporali di gamma emettitori in matrici atmosferiche (PM10 e bulk deposition) in stazioni in quota dell'Emilia Romagna, ARPA FVG, Twenty-five years after the Chernobyl accident: studies, remarks and recent findings, Udine, June 21-23, 2011. [conference proceedings]
- Laura Tositti, Erika Brattich, Giorgia Cinelli, **Alberto Previti**, Domiziano Mostacci, Comparison of radioactivity data measured in PM10 aerosol samples at two elevated stations in northern Italy during the Fukushima event, Journal of Environmental Radioactivity 114, (2012), 105-112. [paper]
- B. Ganapol, P. Picca, **A. Previti**, D. Mostacci, The Solution of the Point Kinetics Equations via Converged Accelerated Taylor Series (CATS). PHYSOR 2012, Knoxville, Tennessee, USA, April 15-20, 2012. [conference proceedings]

- Barry Ganapol, **A. Previti**, D. Mostacci, Benchmarks for the Point Kinetics Equations. M&C 2013, Sun Valley, Idaho, USA, May 5-9, 2013. [conference proceedings]
- R. Furfaro, **A. Previti**, P. Picca, J. S. Kargel, M. P. Bishop, Radiative Transfer Modelling in the Cryosphere, in: Global Land Ice Measurements from Space, J.S. Kargel, G.J. Leonard, M.P. Bishop, A. Käab, and B. Raup (Editors), Praxis-Springer (Publishers), Heidelberg (2013), ISBN: 978-3-540-79817-0. [book chapter]
- **Alberto Previti**, Richard Sanchez, Domiziano Mostacci, Computation of the Doppler-broadened scattering kernel and its Legendre moments. SNA+MC 2013, Paris, France, October 27-31, 2013 [conference proceedings]